POLITECNICO
MILANO 1863

SCUOLA DI INGEGNERIA INDUSTRIALE
E DELL'INFORMAZIONE

De-orbiting mission from LEO: design of a passive deployment system for an origami drag sail

Tesi di Laurea Magistrale in
Space Engineering - Ingegneria Spaziale

Author: **Tommaso Sironi**

Student ID: 968761
Advisor: Prof. Antonio Mattia Grande
Co-advisors: Laura Pernigoni
Academic Year: 2021-22

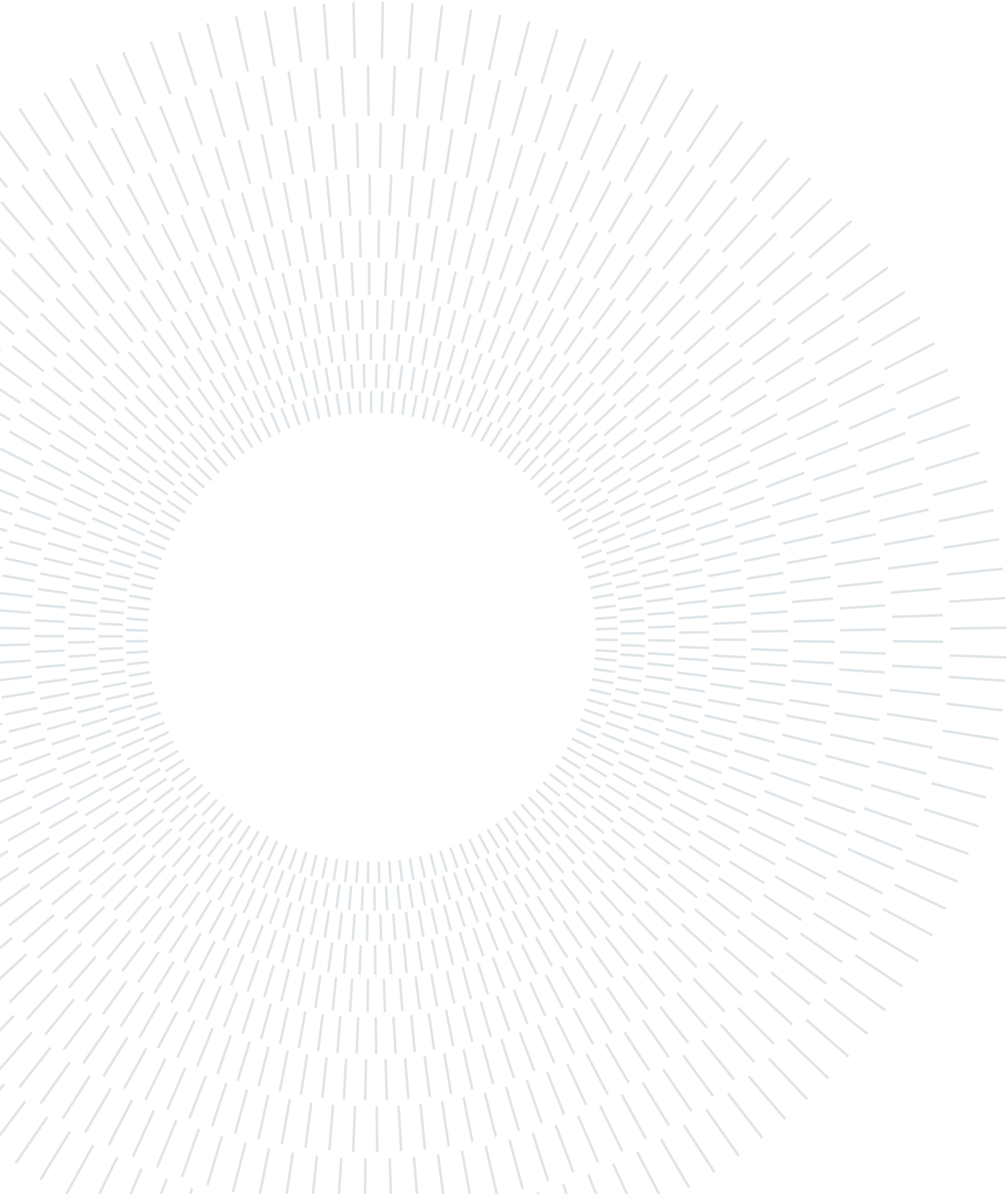

Abstract

Many of the subsystems equipping space vehicles are made up of structures requiring large dimensions to provide performance compatible with the mission requirements. A typical example is the drag sail, a membrane structure capable of reentry vehicles into the atmosphere at the end of their operational lifetime and responding to the growing interest in orbital space debris mitigation. The surface of the sail necessary to complete the de-orbiting within the times dictated by the new international regulations must be huge, therefore the design of an appropriate deployment system is of great interest. Among the various strategies proposed, those that guarantee the sail's autonomous deployment from the packed to the operational configuration stand out. Smart materials such as shape memory alloys can deform when heated above the phase transformation temperature. Therefore, the possibility of meeting the requirement of self-deployment by inserting Nitinol wires along the folds of the origami cells is investigated. Preliminary mission analysis is initially conducted to determine the sail size needed to de-orbit the satellite from LEO orbits: the two-body problem orbital model is implemented in MATLAB for this purpose and then validated using the Ansys STK Premium Space software. This step is followed by the thermal analysis of the system to verify the operating temperatures of the sail during the mission and the analytical modeling of the constitutive law of shape memory alloy. The sail is finally modeled in MATLAB as a multi-body system, and the deployment dynamics are analyzed by co-simulation between ADAMS and Simulink software. The results show that the shape memory alloys can exert sufficient force to bring the sail from the stowed to the operational configuration. Potential future applications are not only limited to the one-way deployment of structures of this type but also to control the shape morphing of the structure according to operational needs.

Keywords: drag sail, space debris, origami, passive deployment, shape memory alloys, multi-body dynamic simulation

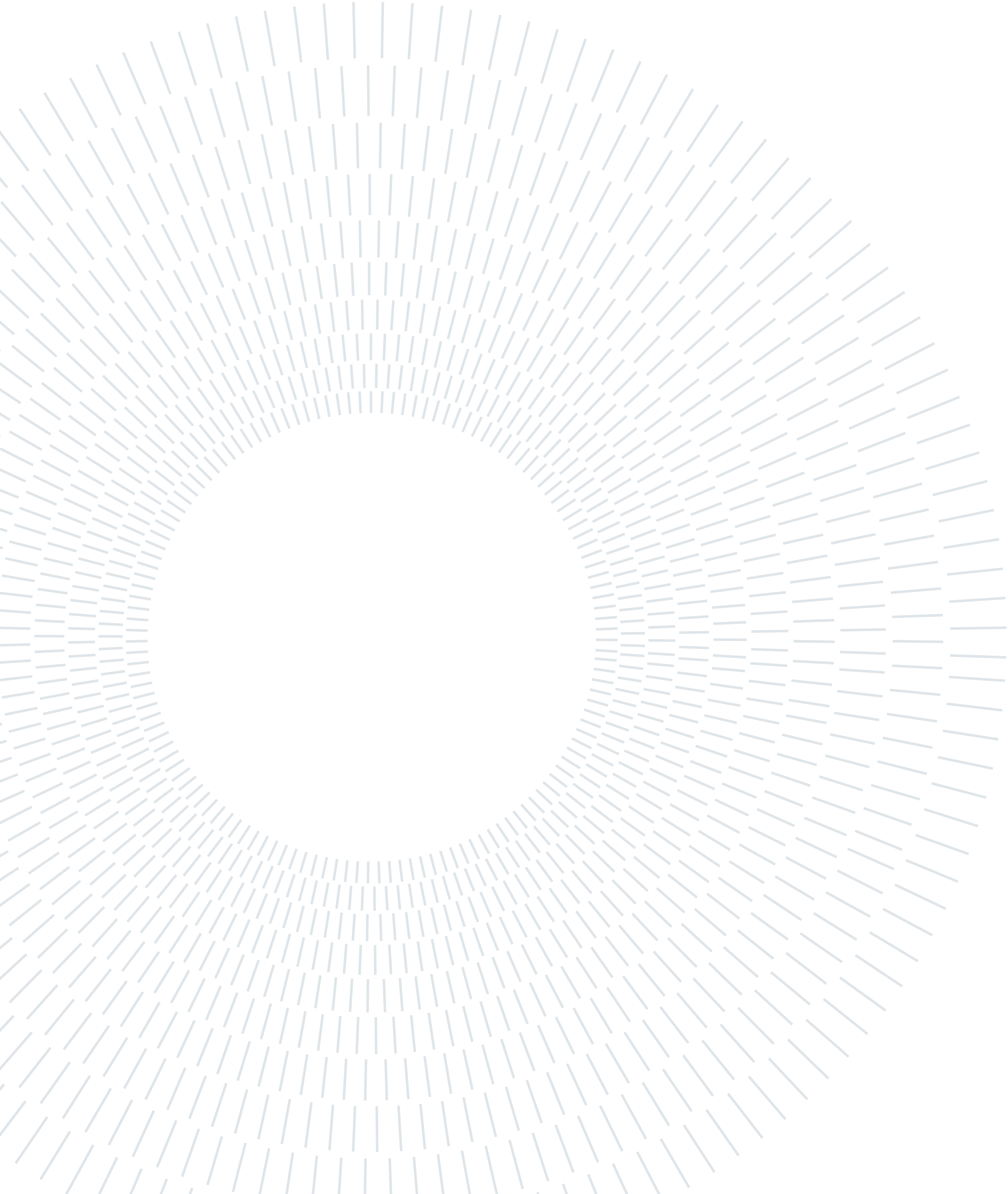

Abstract in lingua italiana

Molti dei sottosistemi che equipaggiano i veicoli spaziali si compongono di strutture che richiedono grandi dimensioni per poter fornire prestazioni compatibili con i requisiti della missione. Un tipico esempio sono le drag sails, strutture a membrana in grado di far rientrare i veicoli in atmosfera al termine del loro ciclo di vita operativo e che rispondono quindi al crescente interesse verso la problematica relativa all'accumulo dei detriti spaziali in orbita. La superficie della vela necessaria a completare il de-orbiting entro i tempi dettati dalle nuove regolamentazioni internazionali dev'essere molto estesa, perciò la progettazione di un opportuno sistema di dispiegamento è di grande interesse. Tra le varie strategie proposte, spiccano quelle che garantiscono lo sviluppo autonomo della vela dalla posizione impaccata a quella operativa. Materiali intelligenti come le leghe a memoria di forma sono in grado di deformarsi se riscaldate al di sopra della temperatura di trasformazione di fase, perciò viene indagata la possibilità di soddisfare il requisito di dispiegamento autonomo attraverso l'inserimento di fili di Nitinol tra le pieghe dell'origami. Un'analisi preliminare della missione è inizialmente condotta per determinare le dimensioni della vela necessarie a far de-orbitare il satellite da orbite LEO. Per fare ciò, viene implementato in MATLAB il modello orbitale *two-body problem* che è poi validato per mezzo del software STK Premium Space di Ansys. Seguono l'analisi termica del sistema per verificare le temperature operative della vela durante la missione e la modellazione analitica della legge costitutiva delle leghe a memoria di forma. La vela è stata infine modellata su MATLAB come sistema multi-corpo e la dinamica del dispiegamento viene analizzata per mezzo della co-simulazione tra i software ADAMS e Simulink.
I risultati mostrano come le leghe a memoria di forma siano in grado di esercitare sufficiente forza da portare la vela dalla configurazione stivata a quella operativa. Potenziali applicazioni future non si limitano soltanto al dispiegamento a una via di strutture di questo tipo, ma anche al controllo della modifica della forma della struttura in base alle necessità operative.

Parole chiave: drag sail, detriti spaziali, origami, dispiegamento passivo, leghe a memoria di forma, simulazione multicorpo

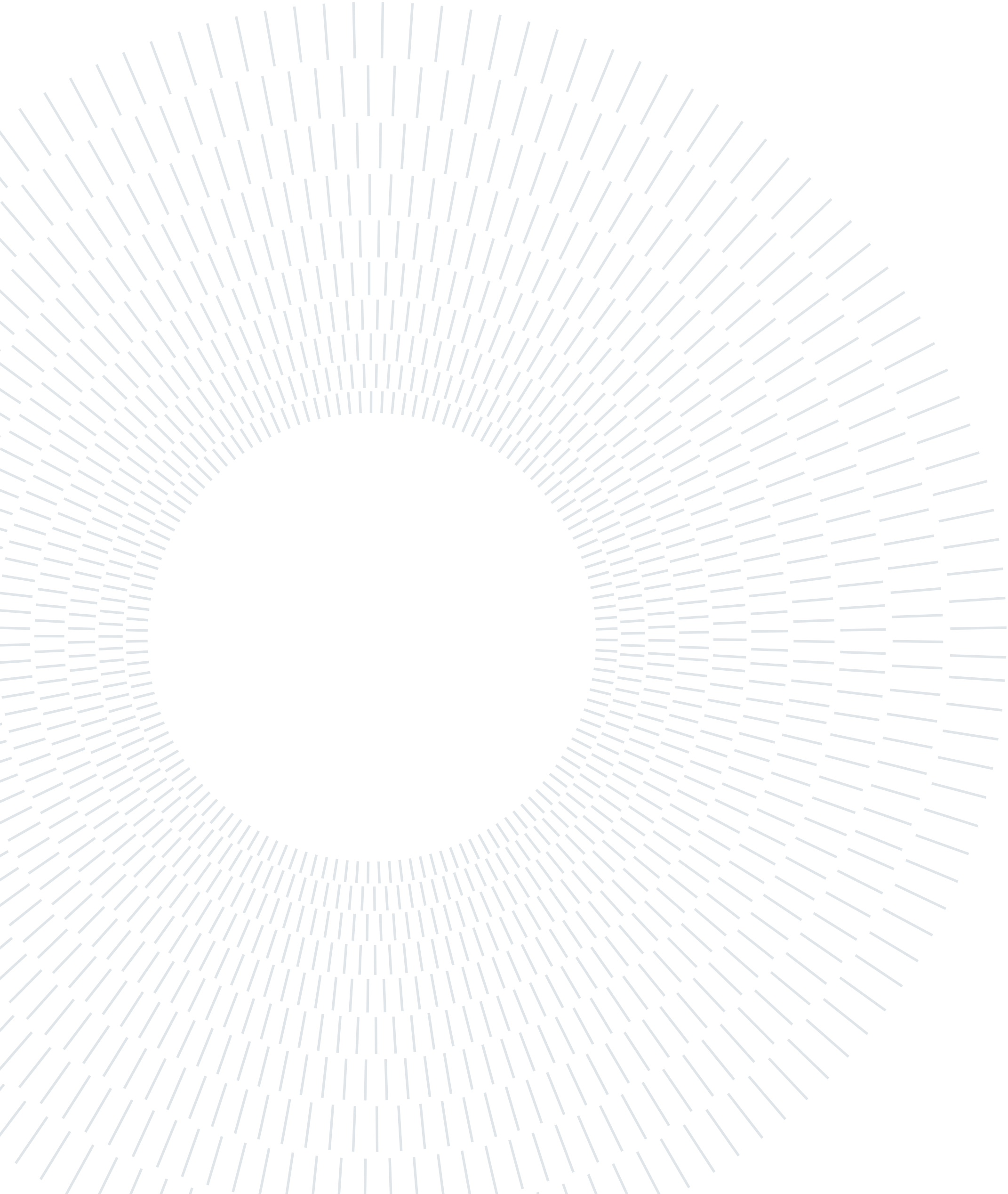

Contents

Abstract **i**

Abstract in lingua italiana **iii**

Contents **v**

Introduction **1**

Aim of the thesis **3**

1 Space debris mitigation **5**
- 1.1 Space debris 5
- 1.2 De-orbiting technologies: state of the art 7
- 1.3 Drag sails 12
  - 1.3.1 Sail film and origami folding patterns 12
  - 1.3.2 Actuation devices and rigidization systems 17

2 De-orbiting design **21**
- 2.1 Two-body problem 21
- 2.2 Orbital perturbations 22
  - 2.2.1 Solar radiation pressure 23
  - 2.2.2 Air drag 23
  - 2.2.3 Earth oblateness 24
- 2.3 De-orbit strategy 26
- 2.4 FCC requirement: 5-year de-orbit 29
- 2.5 Model validation 31
- 2.6 Optimized packed configuration 33

3 Thermal analysis **37**
- 3.1 Thermal cycle along the orbit 37

3.2 Satellite burning in the atmosphere 41
3.3 Thermal analysis during deployment phase 42

4 Miura-Ori multibody dynamics 47
4.1 Origami dynamic modeling 47
4.2 Miura-Ori model in ADAMS 49
4.2.1 Miura-Ori faces 49
4.2.2 Miura-Ori crease lines 51
4.3 ADAMS-MATLAB integration 53

5 Passive actuator design 57
5.1 Foundamentals of shape memory alloys 57
5.2 Drag sail passive actuator 60
5.2.1 Nitinol properties 60
5.2.2 SMA actuator configuration 62
5.2.3 Thermal model 63
5.3 Shape memory effect model 64
5.4 Actuator in ADAMS-MATLAB model 67

6 Deployment simulation 71
6.1 ADAMS-Simulink co-simulation 71
6.2 Actuator configuration influence on deployment 73
6.3 Deployment design 75
6.3.1 Deployment dependency on SMA length, radius and strain 75
6.3.2 Optimization algorithm 78
6.4 Simulation of the optimum geometry: results 83
6.5 Uncertainty propagation 87

7 Conclusions and future developments 89

Bibliography 91

A SMA actuator configuration choice 97

List of Figures 103

List of Tables 107

List of Symbols **109**

Acknowledgements **113**

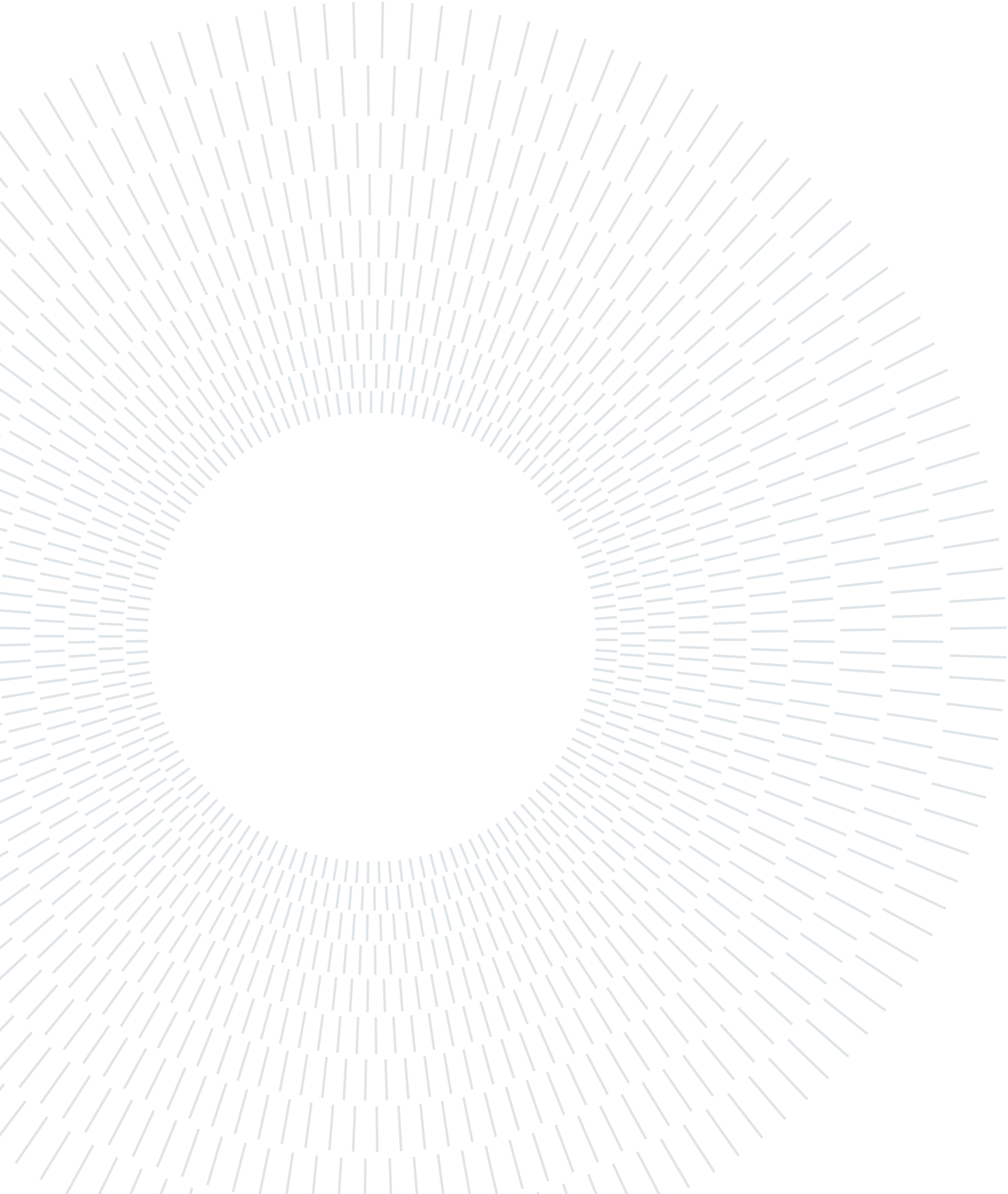

Introduction

The adoption of large structures has always been a concern in the design of satellites and spacecraft since the performances of elements such as solar panels, sails, or antennas depend on their size. However, space vehicles are required to restrict their volume within the limited space available in the launcher. Such a requirement can be tough to meet when large structures must be employed. In this framework, gossamer structures allow equipping spacecraft with large deployable components by reducing costs and weight compared with traditional mechanical deployment systems.

Gossamer structures are flexible, deployable membranes used in a planar or curved configuration with a high ratio of unfolded surface to folded volume [17]. The interest in this technology dates back to the early space projects. However, no satellites equipped with these structures were launched until 1996, when NASA tested IAE (Inflatable Antenna Experiment) in the space environment (Figure 1).

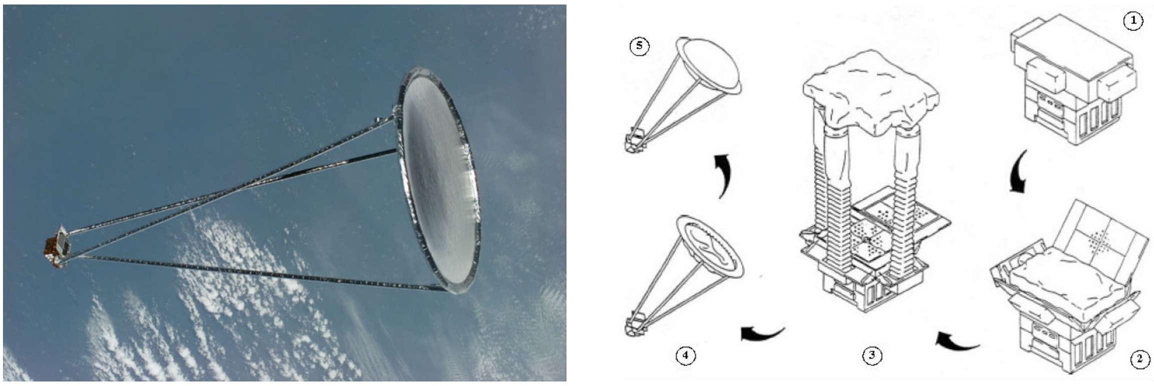

(a) IAE in orbit picture.

(b) IAE deployment sequence.

Figure 1: Inflatable Antenna Experiment [26]

The research about gossamer structures mainly concerns the minimization of packed volume and the deployment strategy. Considerable progress has been made on the first, leading to ever-larger structures. However, the greater the dimensions, the more difficult it is to design a suitable deployment mechanism.

In the last years, origami's application in space engineering is playing a pivotal role in research on reducing the space filled up by the membrane structures inside the satellite. Furthermore, the origami structure guarantees simple and effective deployment strategies being easily controlled during the actuation phase. The ancient art of paper folding is thus the most promising technology for the future design of gossamer structures.

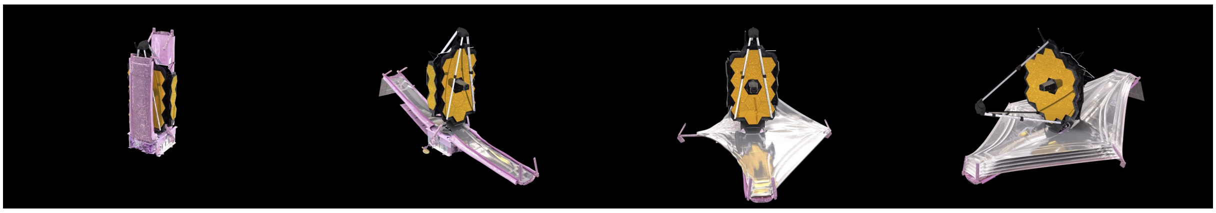

Figure 2: James Webb Space Telescope: sunshield deployment phase.

As regards the deployment, once the vehicle reaches space the gossamer structure starts unfolding, usually driven by electric motors or by the release of strain energy. The research is increasingly oriented toward the use of actuation systems not requiring the supply of energy from the satellite (passive deployment). In this context, shape memory materials (alloys or polymers) respond to the requirement of a passive actuation system. The shape memory effect consists of the recovery of a pre-strain by simply rising the temperature above the transformation temperature limit. The process can be controlled by the Joule effect or it can be passively actuated by exposure to Sun's radiation.

Among the countless possible applications, gossamer structures based on origami patterns can be exploited to design drag sails. This extremely light propulsive system takes advantage of solar pressure and air drag to decelerate the spacecraft until its reentry into the atmosphere by unfolding a huge sail from inside the satellite. The actuation system is a primary concern in the design of such a de-orbiting device and smart materials actuators are suited for the purpose of realizing a passive deployment.

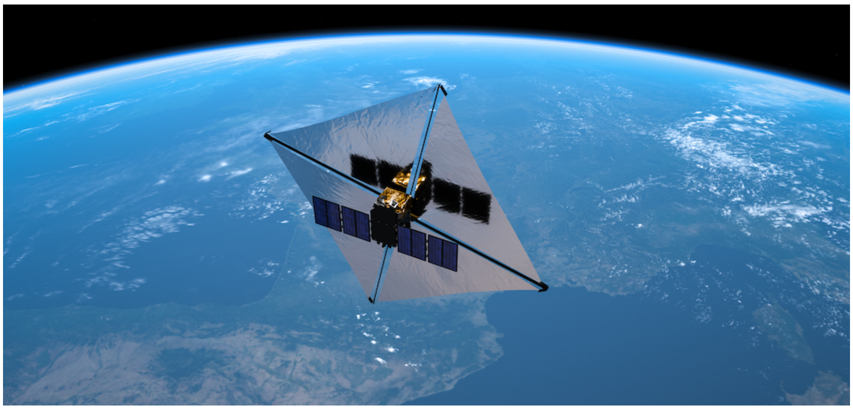

Figure 3: Drag sail de-orbit device.

Aim of the thesis

The thesis aims to design a passive actuation system for space field origami deployable structures and verify that this is compatible with the satellite coupling requirements. The design is based on a particular case study, that of a drag sail for the de-orbiting of CubeSats in LEO.

The design will focus on one of two critical aspects of gossamer structure research and development: the deployment. This phase must be totally passive, therefore capable of deploying the sail without being supplied with electricity or energy from the satellite. In order to do this, the structure is equipped with hinges in SMA material (Nitinol) which, irradiated by the Sun, heat up and recover their initial prestrain.

The study of the deployment is carried out by analyzing the multi-body dynamics of the sail, considering each face of the origami as a rigid body. Given the subsystem requirements, the design requires three distinct types of analysis prior to actual deployment simulation: sail geometry study, system thermal analysis, and Nitinol wire actuation force modeling.

The geometry is designed using software for the integration of the orbital motion of the satellite, able to determine the size of the sail necessary for de-orbiting, and another for optimizing the ratio between stowed volume and surface area deployed.

Once the information on the geometry has been obtained, the thermal analysis makes it possible to verify the system's temperature irradiated by the Sun during the deployment phase, focusing on the variation of the absorbed energy as the bend angle varies.

Finally, the shape memory alloy's constitutive model returns the Nitinol wire's performance aligned along the origami fold lines.

The simulation of multi-body dynamics considers all these aspects and aims to verify the effectiveness of the system conceived. The configuration of the wires should exert a uniform force on the whole structure and guarantee a controlled and gradual deployment despite being completely passive.

This deployment system also allows, if properly implemented, to have a non-passive but, on the contrary, reversible and controllable implementation system.

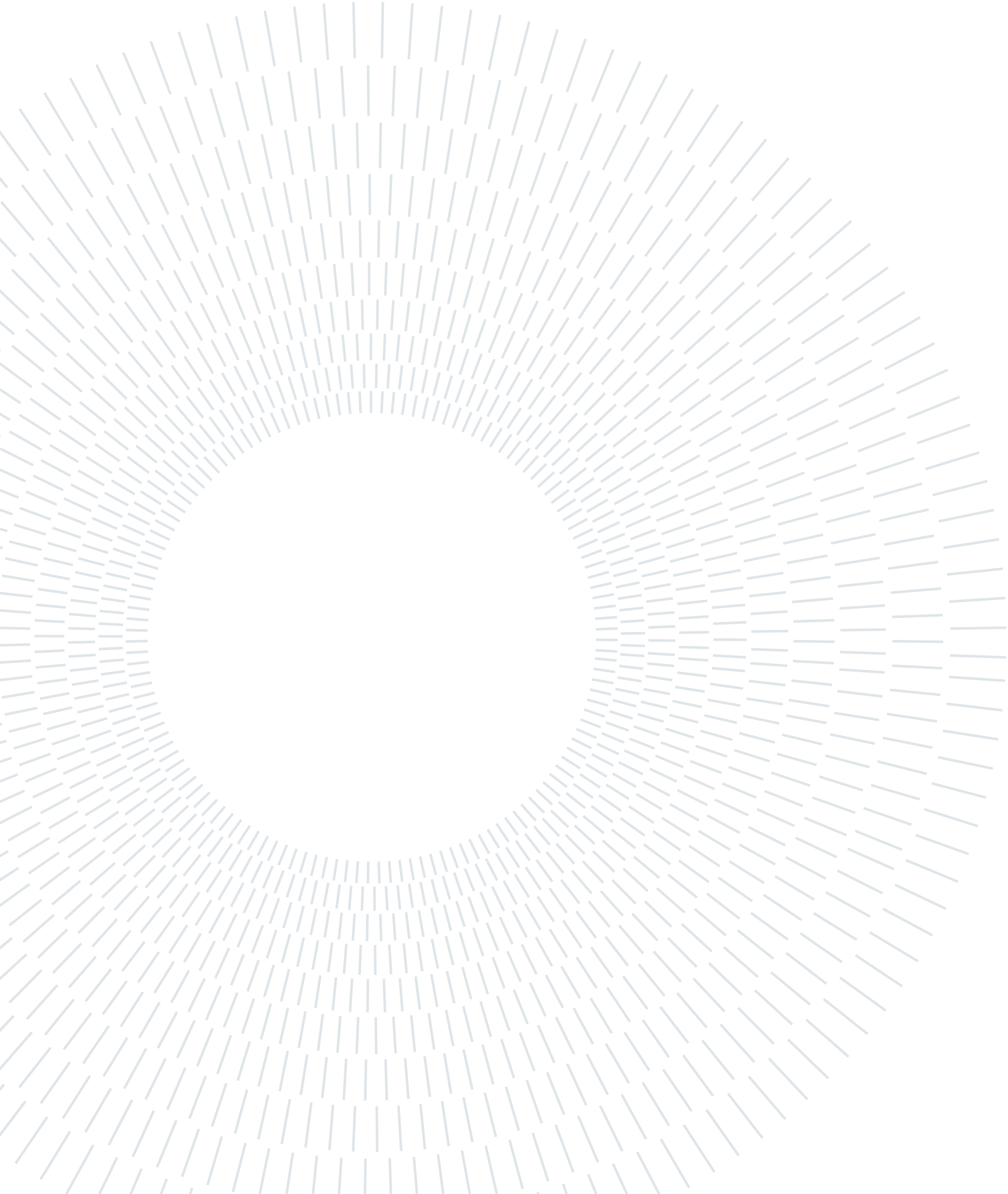

1 | Space debris mitigation

The first chapter presents an overview of space debris mitigation. A brief introduction to space debris and de-orbit competitive technologies anticipates a more detailed focus on drag sails and their applications. The aim is to contextualize the analysis of the deployment system of an origami sail described in the following chapters.

1.1. Space debris

Today more than ever people are space users. Everyday life strongly depends on the contribution given by satellites orbiting the Earth, from internet connection to geolocalization via Earth observation for environmental forecasts or military applications. The intensive exploitation of space technologies and the birth of ever-new solutions (like satellite constellations) make space around the Earth more and more crowded. In agreement with this, the picture below illustrates the evolution of space usage through the years, with a distinction between space objects (Figure 1.1). It is evident the steady rise in the number of payloads (PL) launched in a year, with a consequent and almost uncontrolled increase in the number of payload debris (PF, PD,PM) and rocket debris (RF).

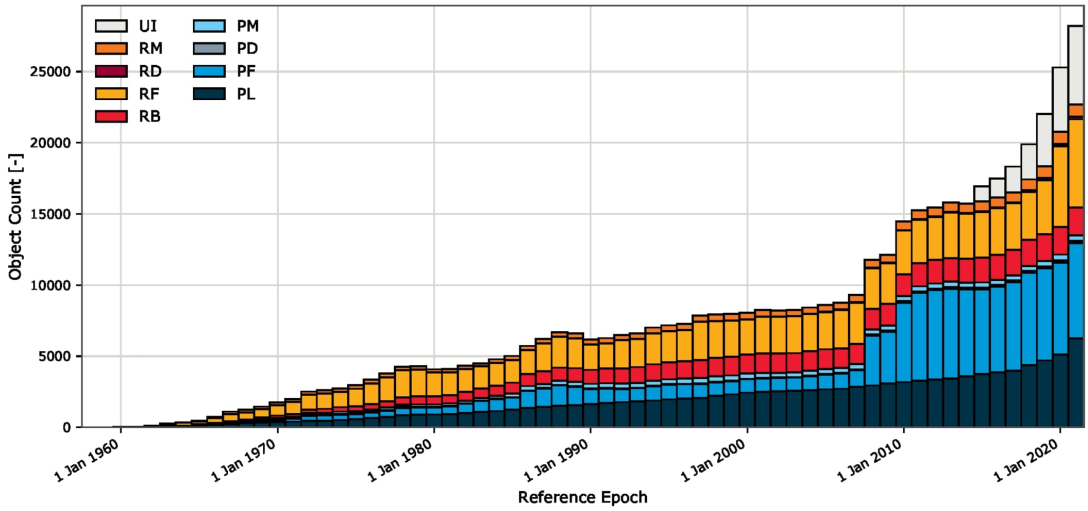

Figure 1.1: Space objects evolutions in all orbits. Report by ESA [28].

Among the orbits around the Earth, Low Earth Orbits (LEO) are the most affected by this overcrowding phenomenon since they are the most accessible and less expensive orbits to be reached. Moreover, the proximity to the Earth is favorable for many technological applications such as Earth observation or communication, with the recent advent of the constellation missions being an additional and relevant source of overpopulation. Satellite clusters are in fact sets of space objects working in synergy to provide global coverage of the service, thus requiring a large number of satellites that communicate with each other. The main example is Starlink, by SpaceX, an internet connection constellation with the target of providing global internet access. With the maiden launch dated February 22, 2018, SpaceX planned to complete the service with the deployment of about 12000 satellites (extendable to 42000), a consistent impact on the density of artificial objects in LEO.

In addition to operative satellites, LEO hosts myriads of defunct spacecraft and debris that contribute to the increase in the multitude of space objects around the Earth. This picture is worrying from the point of view of collisions since the so-called "space junk" can hit operative space vehicles and endanger the proper functioning of the subsystems or even the mission accomplishment. An example is reported in Figure 1.2b, which shows the image acquired by the board camera of Copernicus Sentinel-1A detecting a small damage on the solar array: an impact with a particle caused a small power reduction in the array and a slight change in the attitude of the satellite.

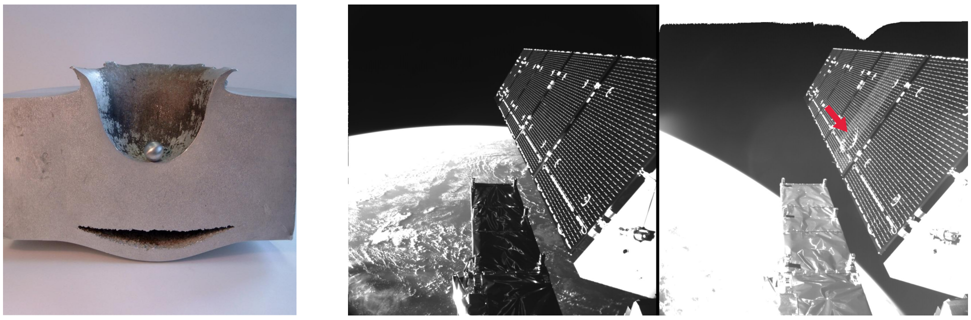

(a) Impact crater.

(b) Copernicus Sentinel-1A satellite.

Figure 1.2: Space debris impact damages on spacecrafts.

In order to account for the impact of debris, the analysis of the potential collisions is carried out both during design and while the satellite operates in orbit. This analysis is achieved with the aid of statistical monitoring systems for the computation of the debris risk [50]. An example of such software is ORDEM 3.2 developed by NASA's Orbital Debris Program Office, providing precise knowledge of the orbital environment [54].

The table below shows the impact probability of a satellite orbiting in LEO. An impact with sub-millimeter-size debris can cause small damages and produces craters in the envelope of the satellite, while in membrane structures like gossamers the damage results in real holes. A debris larger than 1mm can even destroy subsystems, while a 10cm object collision entails a catastrophic destruction of the spacecraft.

Particle dimension	>0.1mm	>1mm	>10mm
Micrometeorite	0.68 days	3.43 years	34000 years
Debris	0.49 days	0.53 years	4000 years

Table 1.1: Time elapsed between two successive collisions [18].

The orbital overpopulation is getting more and more a concern for space users: the more objects around Earth, the more the probability of registering bumps between satellites, resulting in the scattering of fragments in orbit which increase the collision probability even more [57]. This chain effect is named the Kessler Effect. To counteract this syndrome, Federal Communications Commission (FCC) established the "25-Year Rule", asserting that any no longer usable object orbiting around the Earth, called space debris, must de-orbit within 25 years of the end of its operative life. The "25-Year Rule" turned into the more recent "5-Year Rule" in September 2022 to keep up with the rapid space race [12]. The FCC rules have relevant consequences on the design of the satellites: if before the advent of the legislation there was no need to think of a way to take the satellite out of orbit, now debris removal missions or de-orbiting devices equipping satellites must be designed.

1.2. De-orbiting technologies: state of the art

The rate of decay of satellites orbiting in LEO depends on several factors. The main influence is given by the altitude above Earth's surface, since the higher the orbit, the lower the density of the atmosphere. Below about 400 km the air drag is significant enough to make the satellite reenter the atmosphere in less than 5 years as stated by FCC. Contrary to the previous case, a de-orbiting system is required for satellites above 400km altitude.

The first trend that aims at clearing the space around the Earth is the debris removal mission. It consists of a spacecraft having advanced guidance, navigation, and control systems capable of approaching and capturing the debris. After orbital capture, the debris is slowed down and returned to the atmosphere. A noteworthy mission of this kind is ClearSpace-1 by ESA [27] (Figure 1.3a), whose launch is scheduled for 2026. The spacecraft equipped with robotic arms will capture and de-orbit Vespa (Vega Secondary Payload Adapter) from a disposal orbit of about 801-664 km altitude.

The rendezvous with the debris is one of the most critical aspects of the mission, so deep research in this field is carried out with the aid of on-orbit tests. An example is the ELSA-d mission [5, 23] by Astroscale, launched on March 22, 2021. The mission consists of two satellites, a servicer and a client, with masses of about 175kg and 17kg respectively. The two modules demonstrated the capability of finding and docking potential debris by continuously releasing the client from the servicer. Other mission concepts make use of nets to collect one or multiple pieces of debris at a time, as shown in Figure 1.3b.

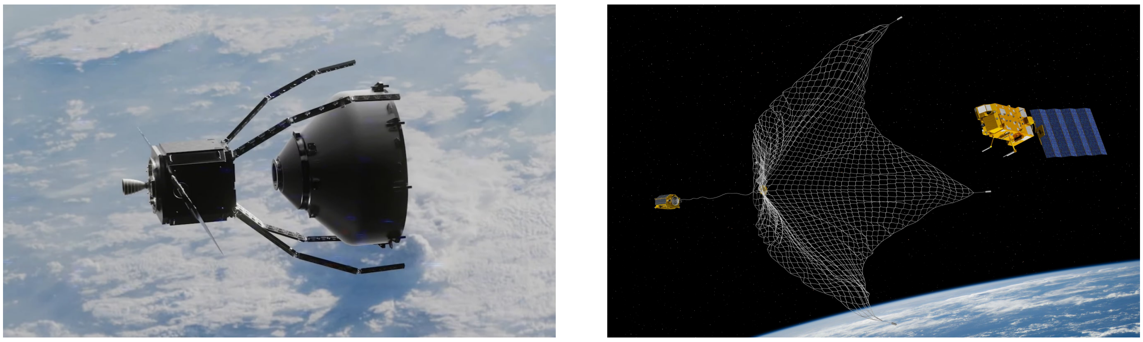

(a) Concept of ClearSpace-1 mission by ESA.

(b) Satellite capture with net.

Figure 1.3: Debris removal mission concepts.

The missions just described are suitable just for the return of space objects not equipped with their own de-orbiting subsystem. In fact, an autonomously de-orbiting satellite would not require specially designed recovery missions to be sent into space, with a significant saving on the cost of recovery. It is thus convenient to supply future satellites with subsystems capable of reducing the in-orbit lifetime by exploiting the thrust of a propulsion system in the opposite direction to the orbital velocity.

The thrust needed to slow down and de-orbit the spacecraft can be provided both actively and passively. In the first case, satellites are equipped with propellant thrusters or electric thrusters. This solution is the most effective because of the large thrust they can provide, allowing a simple accomplishment of the 5-year requirement dictated by FCC. On the other hand, the volume and the mass of the subsystem including tanks, feeding lines, and the motor is critical, above all on CubeSats.

Several companies are investing in active deorbit systems and they already produced technology demonstration missions. These systems are usually associated with spacecraft-based deorbiting systems, but they can even equip satellites granting autonomous reentry. An example of the application of this technology is provided by Momentus company with the Vigoride vehicle [53]. The spacecraft was launched on May 25, 2022, with the aim of deploying three satellites on their respective orbits. Once the mission was accomplished, the vehicle slowed down and de-orbited thanks to the water plasma propulsion system with which it was equipped (figure 1.4a). Another interesting technology is the one proposed by D-orbit with the D-Orbit Decommissioning Device (D3) [14]. This smart motor optimized for decommissioning maneuvers easily removes satellites from their orbits thanks to a powerful solid motor booster equipped with thrust vector control (figure 1.4b).

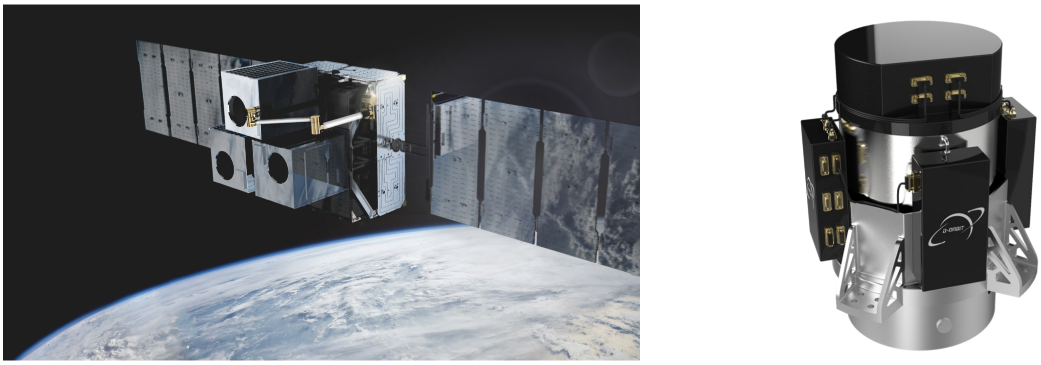

(a) Vigoride spacecraft servicer. [53]

(b) D3 propulsive system.

Figure 1.4: Active de-orbiting systems.

The counterpart of active propulsion de-orbiting modules are passive propulsion subsystems. They consist of large membrane structures (known as gossamer structures [17]) capable of exploiting the acceleration due to solar radiation pressure (SRP) and air drag to gradually reenter the atmosphere. The design requires just a main thin structure (usually a sail) supported by a rigidization system, which unfolds from a stowed arrangement to a large-surface deployed configuration. The classification of the passive systems is based on the altitude of the orbit and, as a consequence, on the source of acceleration. In the case of high-altitude orbits, the only acceleration acting on the membrane is the one due to solar activity: the photons colliding on the sail exchange momentum with the satellite, providing an acceleration (Chapter 2.2.1). This kind of passive system is called solar sail. The application is not only limited to the de-orbit accomplishment, but is extended to any application requiring slight and constant propulsion, like orbital maneuvers and interplanetary missions. A relevant mission equipped with solar sail is the one involved in the LightSail program [25, 59]. The mission designed by the Planetary Society was launched in 2015 with the aim of demonstrating solar sail deployment and control flight (Figure 1.5). A huge sail of 32m^2 surface was stored in a small CubeSat and successfully deployed at 800km altitude. The sail was able to increase the apogee of the orbit and escape the slight air drag acting on the satellite at high altitudes. This was possible thanks to a continuous attitude adjustment aimed at exploiting the SRP for acceleration purposes (more detailed information about sail attitude in chapter 2.3).

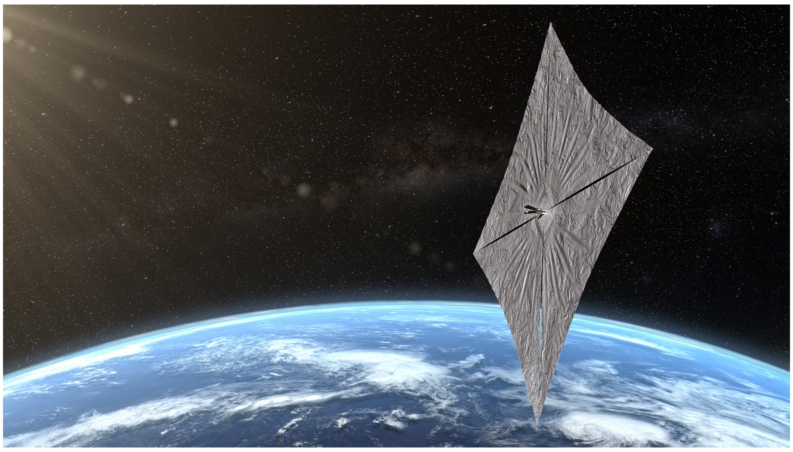

Figure 1.5: Lightsail spacecraft, graphical representation of the in-orbit deployed sail.

As regards lower altitudes, the most interesting passive de-orbit system for LEO satellites is the drag sail. The working principle is the same as the one of the solar sail, but the denser atmosphere of these orbits allows the sail to exploit even the stronger acceleration due to air friction. Drag sails operate from about 400km to 900km. Below the lower limit, the surface of the spacecraft exposed to air particles is generally enough to make the vehicle reenter without any de-orbit device. Above 900km instead the air becomes more and more rarefied and consequently the sail less effective.

A recent successful mission is the CanX-7 CubeSat demonstrator, developed by the Space Flight Laboratory and the University of Toronto Institute for Aerospace Studies [24] (figure 1.6a). The nanosatellite launched in 2016 was equipped with a 4m^2 drag sail deployed the following year at an altitude of 700km. The target was to limit the in-orbit lifetime (estimated to be about 180 years without the adoption of a de-orbit system) within the limit dictated by the FCC at the time (25 years). The mission was accomplished on June 13, 2022, just 5 years after the deployment of the sail [58], demonstrating that the old lifetime requirement could easily be met.

A more recent mission is the Drag Augmentation Derbiting System (ADEO) breaking sail, born from the collaboration between ESA's General Support Technology Programme and HPS GmbH company. The small satellite deployed a 3.6m^2 sail from a 1U unit volume in late December 2022 and will demonstrate the effectiveness of the drag sail de-orbiting system (figure 1.6b). The interest of ESA in this technology is very strong: according to ESA's Zero Debris Initiative, in fact, the removal of unresponsive satellites from their orbits is becoming a key aspect for the availability and the safety of the orbits for future missions, and drag sails will represent a viable solution for the achievement of the target.

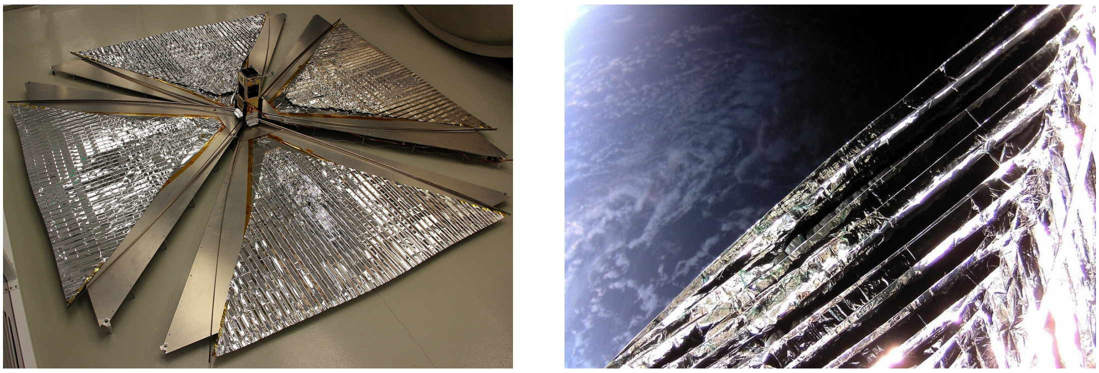

(a) CanX-7 mission by UTIAS/SFL.

(b) Drag Augmentation Derbiting System ADEO breaking sail. On-board camera image.

Figure 1.6: Space debris removal with drag sail.

The appeal of this de-orbit subsystem does not only affect western industries, and it does not refer only to small satellites. Another interesting application is indeed the one adopted by the chinese Shanghai Academy of Spaceflight Technology (SAST) to de-orbit a component of the Long March 2D rocket from LEO. The mission was launched on June 24, 2022, and successfully placed in orbit 3 military reconnaissance satellites. The following day, a 300kg component of the upper stage of the rocket deployed a 25m^2 sail with the aim to de-orbit the booster in about 2 years from an initial orbit of 491km altitude. Evidence of the mission is provided in the following image, captured by the Long March 2D board camera (Figure 1.7). The accomplishment of the mission would be of great interest for the future recovery of launchers and heavy components.

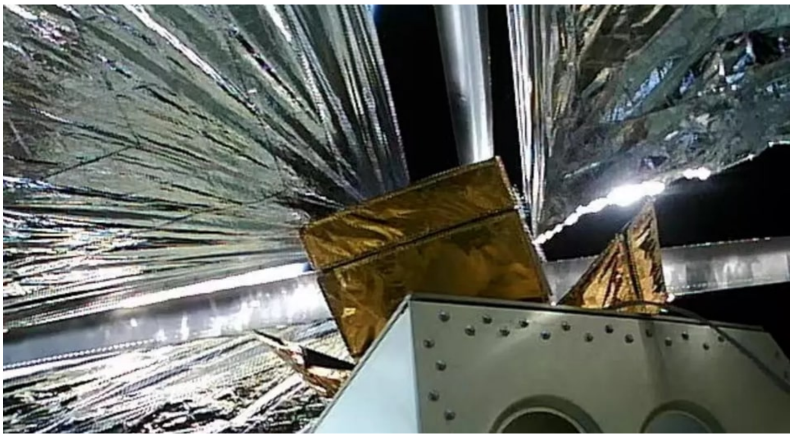

Figure 1.7: Long March 2D deorbit with drag sail. On-board camera image.

In chapter 1.3 the discussion about the drag sails will be deepened, focusing on the three fundamental issues in the design of sails and deployable structures in general: the folding pattern and the volume optimization, the rigidization system, and the actuation system.

1.3. Drag sails

The technology readiness level (TRL) of the drag sails is higher than the one of active decommissioning systems and many companies already commercialized and tested the technology in the space environment. Research has come a long way in the last decade and the technology is constantly advancing. Among the drag sail developing research fields, the optimization of the folded volume, the rigidization systems, and the actuation design are the most critical and interesting for the future of this technology.

1.3.1. Sail film and origami folding patterns

The slight accelerations provided by the friction with air particles force the drag sail to enlarge as much as possible the surface exposed to the atmosphere. Such a large structure is required to have great mechanical flexibility combined with lightness so that it can be easily folded into the small volumes of satellites during launch. In accordance with this, polymers are the most suitable materials for gossamer structure applications because of their low elastic modulus and density. These properties allow the sail to reach thicknesses of a few micrometers, benefiting in terms of compactness while packed. An example is provided by the CanX-7 drag sail described in chapter 1.2, whose structural polymeric film was just 12.7μm thick. However, the mechanical characteristics of drag sail materials must be compatible with the harsh space environment made up of wide temperature ranges, high radiation doses, and reactive elements like atomic oxygen. In this framework, Kapton [21], Mylar [42] and Upilex [61] are polymers specifically designed for harsh applications and are widely used as a structural layer in drag sails. Despite the excellent mechanical, chemical, and thermal properties, the lightness and thickness of these membranes must account for metallic coatings for erosion protection during the long de-orbit lifetime. The long exposure to atomic oxygen in LEO can in fact significantly damage the thin film of polymeric material, up to the complete failure of the mission. A metallic layer of a few tens of micrometers can prevent this harmful phenomenon and grant the integrity of the sail. As regards the CanX-7 sail, the 12.7μm polymeric film was coated with 300Å of aluminum on both sides, incrementing the overall thickness of just one-tenth of a micrometer. An even thinner limit has been reached by ESA'ADEO, enclosing the global thickness of polymeric and metallic layers in about 7.5μm.

The importance of including a protective film in the sail design is highlighted in table 1.2. In the first column, the three previously cited structural polymers are collected with different coating configurations, while in the second column, their respective amount of erosion over the entire de-orbit of a satellite is presented. It is evident how the absence of an aluminum coating can even lead to a gradual disgregation of the entire sail.

Sail-coating combination	Erosion depth [μm]
Mylar	79
Al-Mylar-Al	0
Kapton	74
Al-Kapton	29
Al-Kapton	29
Al-Kapton-Al	0
Upilex	24
Al-Upilex	9
Al-Upilex-Al	0

Table 1.2: Atomic oxygen erosion estimates. Credits: [49].

The thickness of the sail is not the only element ensuring a compact packed volume of the sail, since a proper folding pattern is essential for the maximization of the ratio between deployed surface and stored volume. Moreover, the choice of the pattern can even dictate the shape of the deployed membrane structure and the deployment strategy, making the choice of folding tessellation a crucial design phase.

Among the most common folding techniques, the Z-fold tesselation (figure 1.8a) has been widely tested in the space environment. It consists in the simple alternation of mountain and valley fold lines parallel to each other, which allow the deployment of the structure in a single direction. The perfectly regular pattern plays in favor of the design simplicity and allows to resort to straightforward deployment techniques. The most relevant space vehicle involving the application of this folding technique is the International Space Station. The ISS's solar panels were sent into orbit in a packed configuration and, once in orbit, they unfurled and increased the surface exposure to Sun's radiation. As can be seen in figure 1.8b, the tessellation of the membrane forces the panel to assume an elongated shape, while the other dimension is kept unchanged. This constraint can turn out to be restrictive in case of applications other than the one just presented. For example, if the deployable structure is a drag sail equipping a CubeSat the extended configuration makes the requirement on the rigidization and actuation design complex to be met.

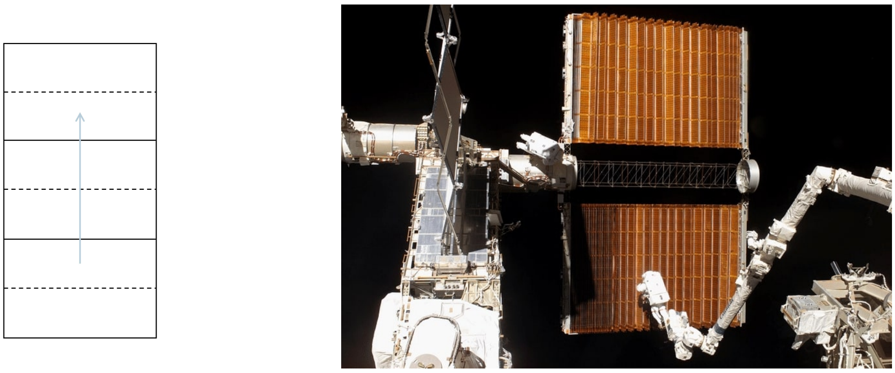

(a) Z-folding pattern.

(b) ISS's solar panel deployment.

Figure 1.8: Z-folding technique. The arrow in 1.8b indicates the deployment direction, while the solid and dashed lines indicate respectively the mountain and valley folds.

In this context, the knowledge of origami and the introduction of mathematic models for the analysis of the tesselations drove the idea of applying the antique art of folding papers to space structures in order to create ad hoc solutions for various applications. Origami are truly beneficial in the design of a deployable structure: aside from the great packing efficiency, a proper scheme of the origami can also stiffen the membrane and reduce the degrees of freedom to the advantage of the actuation system. Nowadays, a wide set of tesselations have been studied and tested for different applications such as medicine and robotics, but the most relevant in the design of drag sails are the ones ensuring a flat shape once deployed.

Miura-Ori is the most famous and simple pattern and possesses the ability to change between two flat configurations, the packed one and the folded one. Unlike Z-fold, the deployment affects both the length and the width of the membrane, ensuring a more uniform packed shape. Nevertheless, the structure can be simply unfolded by pulling it in one direction, without the need to drive the membrane along both deployment directions. Another interesting aspect is the simplicity of the manufacturing process since it consists in the recursive folding of a simple pattern, prone to be automated. The figure representing the alternation of mountain and valley folds (figure 1.9a) highlights the regularity and simplicity of these origami cells.

The history of Miura-Ori application in space industry is limited to a bunch of missions. The first spacecraft equipped with an Origami structure of this kind was the Japanese Space Flyer Unit launched in LEO orbit on March 18, 1995 (figure 1.9b). The energy of the vehicle was supplied by a prototype of an origami folded solar array called 2D Solar

Array (2DSA), whose tesselation was based on a Miura-Ori pattern. The deployment of the structure ended well, but the most interesting outcome was that, at the end of the mission, the solar panel was able to be repacked without problems, demonstrating involuntarily the reversibility of the deployment of origami structures.

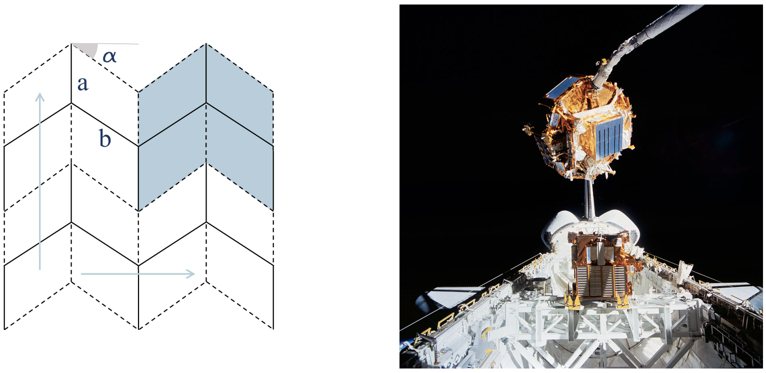

(a) Miura-Ori pattern. (b) Space Flyer Unit mission.

Figure 1.9: Miura-Ori folding technique. The arrows in 1.9a indicate the deployment direction, while the solid and dashed lines indicate respectively the mountain and valley folds. The highlighted cells make up a single unit of Miura-Ori tessellation.

Another commonly used pattern in engineering applications is the Flasher tessellation. Unlike Miura-Ori, the folded membrane of this origami is wrapped around a hollow cylinder or prism. Upon opening, the origami unfurls by rotating and expanding in a planar configuration around the central hollow. This packed geometry can be easily stowed in satellites and ensures a flat extended surface suited for the application in space vehicle components like solar panels, antennas, or solar/drag sails. As can be noted in figure 1.10a, the pattern of the flasher origami is not as regular as the Miura-Ori: the elementary blocks differ in shape according to their position, adding difficulties in the design phase. A further source of complexity is related to the thickness accommodation issue. When the Flasher is packed, the most external parts of the structure wrap around the inner ones. The more the structure grows in size, the more the thickness of the central cylinder/prism to be enclosed by the outer facets, resulting in the stretch of the external part of the membrane. In order to account for thickness without producing structural deformations, the straight radial creases are curved as in figure 1.10b. In this case, the irregularity of the pattern of the facet is even more evident.
In the last few years, the interest in the application of Flasher tesselation in space engineering gave rise to proposed space missions and concepts equipped with large gossamer origami structures. In 2014 NASA's Jet Propulsion Laboratory collaborates with Brigham

Young University, Provo, Utah, on the design of a flasher origami solar array with the purpose to demonstrate the feasibility of the implementation of origami folds in space engineering. The membrane was deployed with the aid of an external truss structure fixed at the external profile of the solar panel [55].

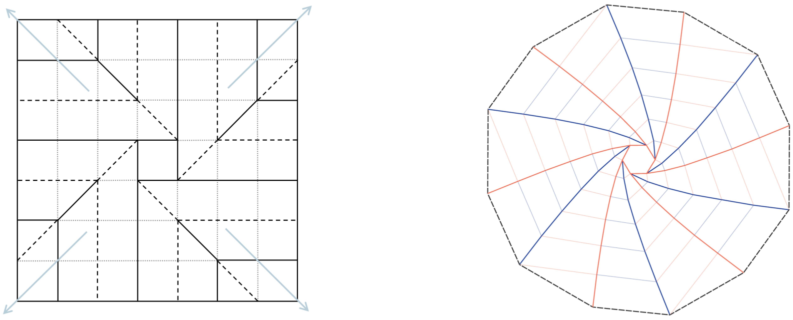

(a) Flasher simplified pattern.

(b) Flasher pattern.

Figure 1.10: Comparison between the flasher simplified pattern (1.10a) and the one accounting for thickness accommodation (1.10b).

The most interesting proposed mission is NASA's Starshade, a huge occulter flying in formation with a space telescope observing exoplanets. The aim of the Starshade is to hide the light emitted from the stars in the field of view of the telescope to ease the direct imaging of its planets. The large structure is composed of an external set of petals and a central disk folded with the flasher technique (figure 1.11b).

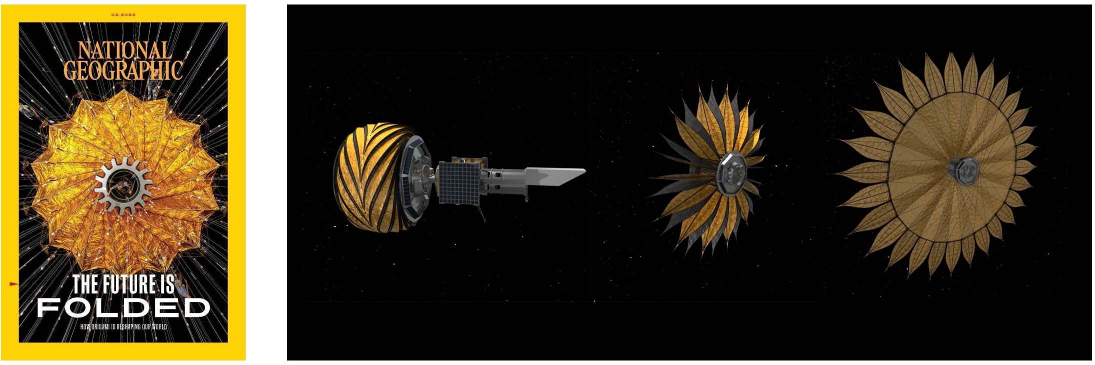

(a) February 2023, National Geographic magazine.

(b) Starshade deployment sequence.

Figure 1.11: Example of Flasher origami application in space engineering. Starshade is currently under development. Credits: National Geographic [31, 32], NASA.

Miura-Ori and Flasher are the most suited origami for space application, but the possibilities of folding gossamer structures extend to many other patterns. Among the existing ones, the most interesting for engineering applications are the ones collected in table 1.3. All of them are prone to deploy in a flat configuration, suitable for drag sail de-orbiting devices, but the packing efficiency varies between the tesselations. In chapter **??** an optimization software developed by Martino Fossati, thesis student of the university of Politecnico di Milano, will lead the choice of the best pattern for the specific application.

Pattern	Facet Shape	Folded shape	Deployed shape
Miura-Ori	Parallelogram	Flat	Flat
Kresling	Triangle	Flat	Cylinder/Flat
Yoshimura	Triangle	Flat	Cylinder/Flat
Waterbomb	Triangle	Cylinder/Flat	Cylinder/Flat
Flasher	Quadrilateral/Triangle	Prism/Cylinder	Flat

Table 1.3: Origami tesselations for space engineering application.

1.3.2. Actuation devices and rigidization systems

Once the characteristics of the sail film are fixed, it is necessary to account for the deployment phase of the structure with the aid of an actuation device. The stringent requirement on the packed volume dictating the design of the membrane applies also to the actuation system, which must be as much compact as possible and compatible with the low mass of the drag sail to not compromise the lightness of the overall de-orbiting device.

The first broad class of actuation systems consists of external structures entrusted with both deployment and rigidity tasks. Figure 1.12 shows an example of such kinds of structures, in which the deployment is carried out by a perimeter truss.

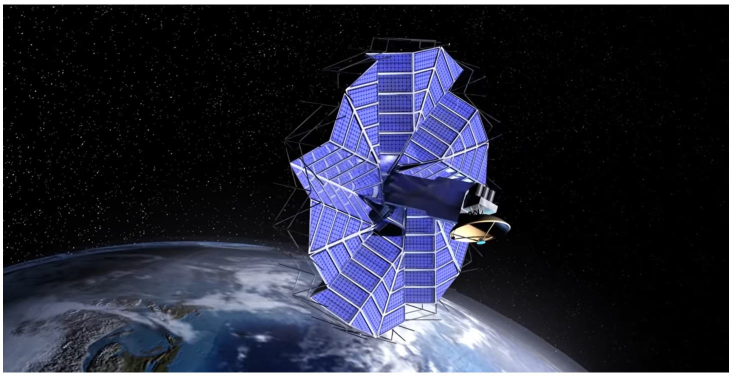

Figure 1.12: Mission concept: perimeter truss deployment system.

The actuation principle is based on the deployment of booms pulling the packed sail outside and keeping it tensioned. Because of the requirement on the size, several solutions have been developed to limit the space filled inside the satellite.
The scissor mechanism (figure 1.12) can be designed in a variety of shapes and configurations and it is able to reach a compact dimension in the stowed arrangement. Moreover, the unfurl phase consists of the release of strain energy at the joints of the beams, making the deployment autonomous once started. However, the disadvantage of this kind of system lies in the storage volume of the truss, too large to be suitable for small satellites. The research on more compact structures led to the implementation of collapsable tubes made of metallic or composite materials. Among the popular solutions, the Storable Tubular Expandable Member (STEM™) [6] is promising for the design of the deployment system of drag sails and solar sails. STEM is a bi-stable tube that can be rolled and deployed from a canister and, once it is extended, it remains rigid due to the convex deployed shape (figure1.13). The extension of the boom is driven by an electric motor, but it can even deploy autonomously via the release of elastic energy, saving the satellite from having to supply electricity. Figure 1.13a shows different configurations of the STEM system: based on the load they have to bear, the tube can be reinforced by unfurling two layers one inside the other. As regards the application in space missions, STEM has flown in the space environment since the 60s, equipping missions like Apollo and Voyager. The most recent one is the James Webb Space Telescope, in which the system is entrusted to pull and unfold the sunshield membranes.

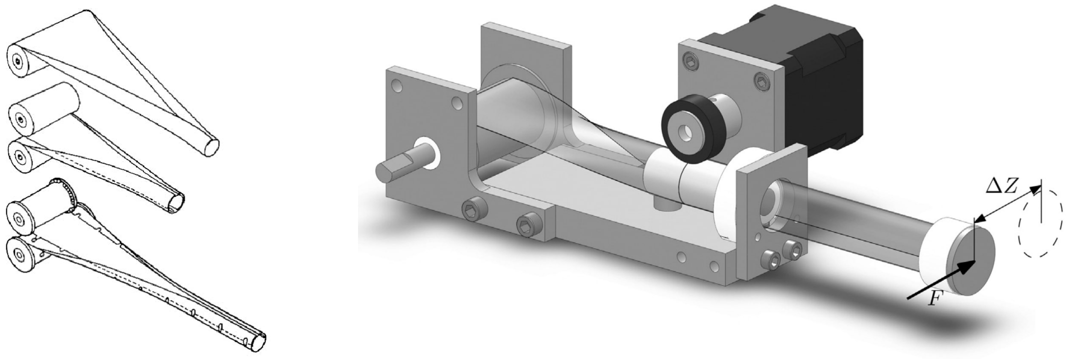

(a) STEM configurations

(b) STEM actuation system.

Figure 1.13: Storable Tubular Expandable Member (STEM) technology.

Another similar configuration is the one of the Collapsible Tube Mast (CTM) [6]. The working principle is exactly the same as for STEM, but it is made of two transversally curved strips of composite material glued together forming a tube. The advantage of this configuration with respect to the previous one is the higher torsional stiffness.

The motor-driven systems and the release of elastic energy are not the only solutions adopted for the deployment of large, thin structures. A valid alternative is represented by the inflatable deployment and rigidization systems. They are based on flexible booms or masts folded inside the spacecraft during launch. Once in orbit, the deployment is actuated by inflating an inert gas (usually N_2) inside the structure which unfurls and assumes the opened configuration. The internal pressure generated by the gas not only promotes the deployment but provides the required stiffening effect. Among the critical aspects, the folding technique is one of the most crucial during design. In 1996 the Inflatable Antenna Experiment adopted a Z-folding technique to bend the flexible booms of the sail structure, but the deployment sequence was unpredictable and the packing efficiency was law. A more interesting solution is the one equipping the InflateSail mission in 2014 1.14a [22]. The three-ply laminate boom made with Aluminium and Biaxially-oriented PolyEthylene Terephthalate (BoPET) was folded around a central mandrel in a flat configuration and deployed along its axis with the aid of the inflated gas. The folding technique relies on origami tesselation, which is better indicated because of the good ventilation of residual gas, the excellent packing efficiency, and the possibility to locally fold into the stowed configuration.
Unfortunately, the application of this deployment system to drag sails suffers from the disadvantage of having to equip the satellite with an inert gas tank, increasing the space occupied by the subsystem. Moreover, the thin deployed structure enclosing the gas is prone to failure if a gas leakage arises.

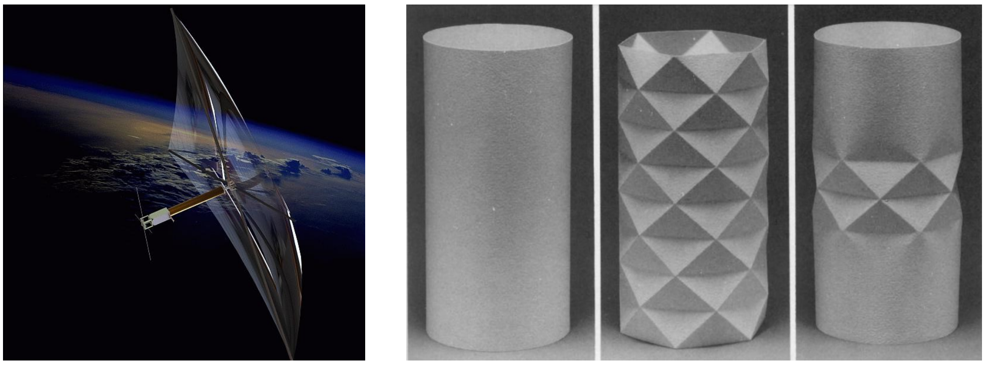
(a) InflateSail Mission (b) Origami folding for deployable booms.

Figure 1.14: Inflatable deployment and rigidization systems.

An innovative way to preserve the lightness and compactness of the drag sails is the adoption of deployment systems based on the shape memory effect provided by alloys (SMA) and polymers (SMP). These materials have the ability to recover a pre-strain providing an external stimulus like temperature change (the focus will be placed on this kind of transformation). Even if the deformation effect is similar, the recovery mechanism differs between SMP and SMA. As regards polymers, they can exhibit both a permanent shape and a temporary shape induced by external stress. If a temporary shape is set, the activation transformation occurs at high temperatures (T_{trans}) since the polymer softens and allows the material to resume the original shape. This effect can show recoverable strains up to 800%. Figure 1.15 shows the picture of the experimental analysis of a SMP deployment system for solar arrays. The folded polymeric structure is capable of recovering the pre-strain by simply rising the temperature above the glass transition temperature of the material. The result is a fast and controlled complete deployment.

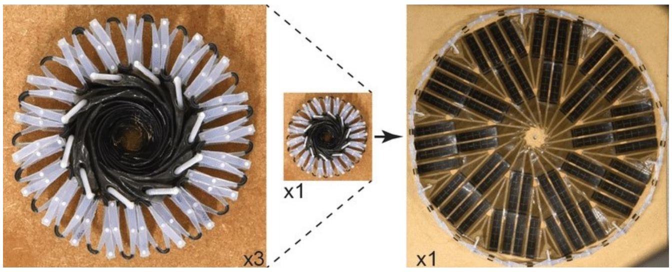

Figure 1.15: Perimeter truss SMP deployment system. Image credits: [11].

Despite the effectiveness of SMP, the low force provided by the polymer during the recovery and the flexibility at high temperatures are relevant drawbacks of this solution. Moreover, the long period of inactivity of the drag sail inside the satellite may decrease the shape memory effect and thus the probability of successful de-orbiting. In this framework, SMAs can make up for the shortcomings of SMPs. The shape recovery principle is based on the transition of the alloy from the martensitic to the austenitic phase upon temperature increase, which can be driven both by Joule heating and by an external source of radiation. One of the strengths of SMAs is the possibility to shape them like wires or strips to allow an easy embedment in the membrane structure, as shown in figure 1.16.

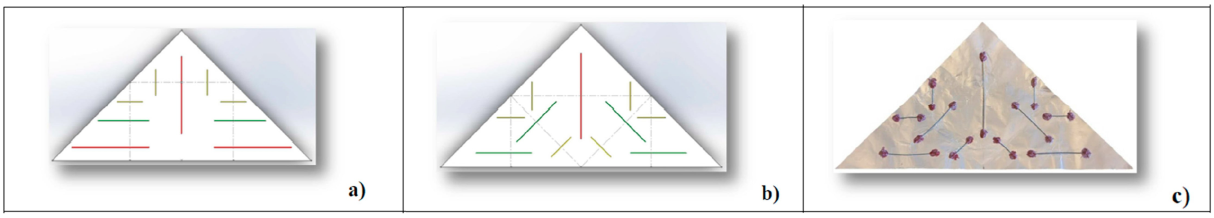

Figure 1.16: SMA embedment in gossamer structure. Image credits: [8].

The adoption of shape memory elements replacing standard electromechanical actuators can simplify the drag sail systems and allow for the reversible deployment of the sail.

2 | De-orbiting design

The purpose of the chapter is to introduce the design of the de-orbiting phase of the satellite mission. The CubeSat orbiting in LEO must reenter the atmosphere within five years, as ruled by the FCC. For this purpose, the two-body problem is implemented in MATLAB® to predict the time required for the satellite to de-orbit with the aid of a drag sail. The accuracy of the model is enhanced by considering the orbital perturbations along the decay orbit. The design ends with the validation of the results entrusted to Ansys Systems Tool Kit (STK) software [2, 3].

2.1. Two-body problem

The two-body problem describes the relative motion of two bodies gravitationally interacting with each other [13]. This model neglects any third-body influence and it is suited for the description of the orbital motion of a spacecraft around the Earth. The formulation of the two-body problem is stated as follows:

$$\ddot{\mathbf{r}} = -\frac{G\left(m_1 + m_2\right)}{r^2}\hat{\mathbf{u}}_r. \tag{2.1}$$

The equation provides the relative acceleration vector $\ddot{\mathbf{r}}$ between the two bodied: m_1 and m_2 are the masses of the two gravitationally interacting bodies and r is the distance between the two centers of mass. The acceleration is directed as the distance versor, $\hat{\mathbf{u}}_r$. On the assumption of m_1 being the mass of the Earth and m_2 the one of the satellite, the second can be neglected and the summation at the numerator simply becomes

$$(m_1 + m_2) = m_1 = m. \tag{2.2}$$

Since the aim is to determine the motion of the satellite with respect to the Earth, it is necessary to define a suitable reference frame for the definition of the satellite's position. The Earth Centered Inertial Frame consists of three mutually orthogonal axes ($\hat{\mathbf{i}}$, $\hat{\mathbf{j}}$, $\hat{\mathbf{k}}$) centered on the Earth, with $\hat{\mathbf{i}}$ and $\hat{\mathbf{j}}$ lying on the equatorial plane. The $\hat{\mathbf{i}}$ axes in the direction of the Vernal equinox, while $\hat{\mathbf{k}}$ points toward the north pole (Figure 2.1).

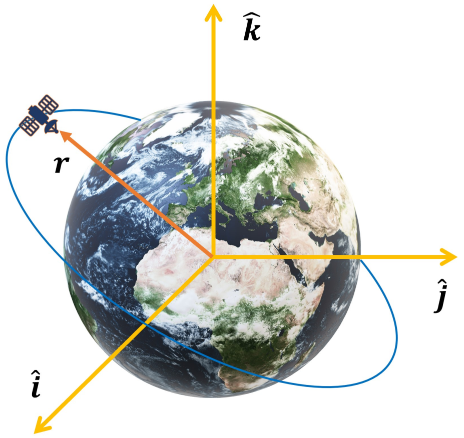

Figure 2.1: Earth Centered Inertial Frame.

With these assumptions, the Equation Of Motion of the restricted two-body problem (EOM) can be written as follows:

$$\ddot{\mathbf{r}} = -\frac{\mu}{r^3}\mathbf{r}. \tag{2.3}$$

with the gravitational parameter computed as

$$\mu = Gm. \tag{2.4}$$

Equation 2.3 is integrated with the aid of an ordinary differential equation (ODE) solver built-in in MATLAB®.

2.2. Orbital perturbations

Equation 2.3 describes the ideal motion of the orbiting satellite and it is valid just if the gravitational interaction between Earth and spacecraft is the only force acting on the satellite. However, in the space environment the orbital motion is altered by a multitude of perturbing forces causing this simple model to fail in predicting the on-orbit positions. The previous equation is thus revised by adding the contribution of the perturbing accelerations as follows:

$$\ddot{\mathbf{r}} = -\frac{\mu}{r^3}\mathbf{r} + \sum \mathbf{a}_{\mathrm{p}}. \tag{2.5}$$

The main perturbing accelerations acting on a satellite in LEO are due to solar pressure, air drag and Earth's oblateness.

2.2.1. Solar radiation pressure

Whenever an object is exposed to Sun's radiation, photons exert a slight pressure due to the exchange of momentum between the light and the body. Although this effect is completely negligible in everyday experience, the contribution on the satellites in the space environment is sizable enough to alter the orbital motion.
According to quantum physics, photons are massless particles traveling at the speed of light ($c = 2.998 \cdot 10^8$ m/s) [13, 33]. The momentum transferred at the impact is computed as the energy of the photon divided by the speed of light:

$$p = \frac{E}{c} = \frac{h\nu}{c} \tag{2.6}$$

where h is the Planck constant ($h = 6.626 \cdot 10^{-34}$ J·s) and ν is the frequency of the electromagnetic wave. The knowledge of the exchanged momentum leads to the determination of the pressure exerted on the satellite: given the surface of the satellite hit by the photons (A) and the power per unit surface of the radiation coming from the Sun ($F_\odot$=1358W/m^2), the pressure P_{SRP} assumes the following expression:

$$P_{SRP} = \frac{1}{A}\left(\frac{\Delta p}{\Delta t}\right) = \frac{F_\odot}{c} \tag{2.7}$$

The SRP is not always constant, but it depends on both the relative distance from the Sun and the optical and geometrical characteristics of the satellite. As a consequence, the complete description of the perturbation turns out to be:

$$\mathbf{a}_{SRP} = -P_{SRP@1AU}\frac{AU^2}{\left\|\mathbf{r}_{s/c-\odot}\right\|^2}\frac{A}{m}\left(2\eta < \hat{\mathbf{n}} \cdot \hat{\mathbf{r}}_{\mathrm{s/c}-\odot} > \hat{\mathbf{n}} + (1-\eta)\hat{\mathbf{r}}_{\mathrm{s/c}-\odot}\right) \tag{2.8}$$

Equation 2.8 represents the acceleration experienced by the satellite due to SRP. On one hand, the more is the distance from the Sun ($\mathbf{r}_{\mathrm{s/c}-\odot}$) the less is the perturbing effect, on the other hand, the acceleration is directly proportional to the area of the impinged surface. The SRP depends also on the optical properties of the spacecraft, in particular on the reflectivity coefficient of its surface (η). $\eta = 1$ implies complete reflection, which is the condition showing the most effective action of the SRP.

2.2.2. Air drag

Satellites orbiting in LEO are close enough to the Earth to experience an interaction with the highest layers of the atmosphere. Even if the density of the air is almost insignificant (from an order of magnitude of 10^{-7}kg/m^3 at an altitude of 100km to 10^{-15}kg/m^3 at 1000km), the impact of air particles generates aerodynamic forces altering the orbital path of the spacecraft. A glaring example is the International Space Station, whose orbital decay due to air drag must be continuously corrected with frequent reboosts provided by the propulsion system. Not only orbital decay, since also heating affects satellites moving at orbital speed. As the altitude lowers the drag effect grows, down to the point where the satellite burns up at a quote of about 120km due to aerodynamic heating (chapter 3.2). Equation 2.9 presents the air drag acceleration on a satellite orbiting in LEO [13]:

$$a_{drag} = \frac{1}{2}\frac{C_D\ A_{cross}}{m_{s/c}}\rho\left(h, T\right)\|\mathbf{v}_{rel}\|^2\,\frac{\mathbf{v}_{rel}}{\|\mathbf{v}_{rel}\|}. \tag{2.9}$$

$m_{s/c}$ is the mass of the spacecraft while $\mathbf{v}_{rel}$ is the relative velocity between the spacecraft and the particles, which are assumed to rotate at the same angular speed as the Earth. The drag coefficient C_D depends on the shape of the satellite and it is usually considered equal to 2.2 (dimensionless). Satellite attitude is relevant as well: the orientation of the normal to the surface A with respect to $\mathbf{v}_{rel}$ defines the cross surface area A_{cross}.
The most complex parameter to be modeled is the density of the atmosphere. As shown in equation 2.9, ρ does not depend just on the altitude, but also on the temperature. Because of almost unpredictable environmental effects, such as solar activity, there is not a model perfectly representing the trend of atmospheric density yet. A lot of models have been implemented over years [4, 63], but the most simple is the exponential one, which describes analytically the relationship between height and density (Equation 2.10).

$$\rho(h, T) = \rho_0 e^{-\frac{h-h_0}{H}}. \tag{2.10}$$

Unfortunately, it is not perfectly consistent with the experimental results and it is not dependent on the temperature of the atmosphere. Therefore, the model used for the design is the COSPAR International Reference Atmosphere from NSSDC, providing empirical models of the atmospheric density [56].

2.2.3. Earth oblateness

The Earth is not a perfect sphere and its mass is not equally distributed. These uneven properties are the cause of orbital drifts that cannot be represented by the spherical symmetric approach for the gravitational field. The undisturbed keplerian orbits must therefore be modified by employing corrections, which are modeled as spherical harmonics [13, 44] and can be distinguished in three main contributions (Figure 2.2): zonal, tesseral and sectoral. Since the influence of the last two mentioned is quite negligible, the zonal harmonics is the only contribution taken into consideration in the following pages.

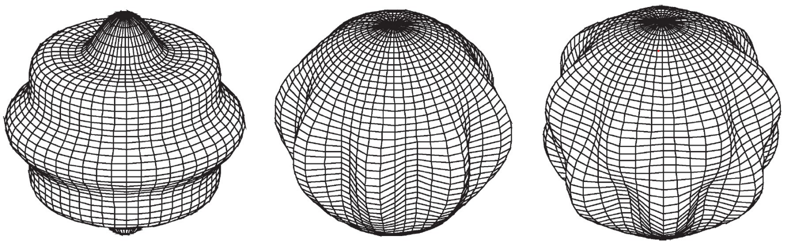

Figure 2.2: Harmonic potentials. From left to right: zonal, tesseral and sectoral.

The rotational symmetric perturbation is thus given by the series:

$$\Phi(r,\phi) = \frac{\mu}{r}\sum_{k=2}^{\infty} J_k \left(\frac{R}{r}\right)^k P_k \cos\phi \tag{2.11}$$

where R is the equatorial radius and P_k are the Legendre polynomials [13]. J_k are the zonal harmonics of the planet, whose values are collected in the table below.

$\mathbf{J_2}$	$\mathbf{J_3}$	$\mathbf{J_4}$	$\mathbf{J_5}$	$\mathbf{J_6}$
1082.6	$-2.3394 \cdot 10^{-3} J_2$	$-1.4960 \cdot 10^{-3} J_2$	$-0.2099 \cdot 10^{-3} J_2$	$0.4994 \cdot 10^{-3} J_2$

Table 2.1: Earth zonal harmonics. All the values are multiplied for 10^6.

The reported series of harmonics is clearly dominated by J_2. The same is true for the highest harmonics, being even more than three orders of magnitudes smaller than J_2. Therefore, the infinite series in equation 2.12 can be truncated at the first order without introducing a relevant error. From the computation of the gradient of Φ the perturbing acceleration sensed by the satellite due to J_2 assumes the following expression:

$$\mathbf{a}_{J_2} = \frac{3J_2\mu R^2}{2}\left[\frac{x}{r^4}\left(5\frac{z^2}{r^2}-1\right)\hat{\mathbf{i}} + \frac{y}{r}\left(5\frac{z^2}{r^2}-1\right)\hat{\mathbf{j}} + \frac{z}{r}\left(5\frac{z^2}{r^2}-3\right)\hat{\mathbf{k}}\right]. \tag{2.12}$$

As the inclination of the orbit grows, the effect of accelerations due to Earth oblateness on the satellite is increasingly strong. This perturbing acceleration cannot be exploited by the air drag for de-orbiting, but it is crucial for a more reliable integration of the orbital motion of the spacecraft.

2.3. De-orbit strategy

The aforementioned environmental perturbations affecting the motion of a satellite are not always to be considered disadvantageous for the accomplishment of a mission. In fact, drag sails are able to exploit the effect of SRP and air drag to de-orbit an end-of-life satellite. This target is reached by orienting the sail such as the overall acceleration given in Equation 2.8 and 2.9 are in the direction opposite to the satellite's velocity vector ($\mathbf{v}_{s/c}$), so as to slow it down. Considering that the density of the atmosphere is completely null above 1000km, the de-orbit model is divided into two cases.

Above 1000km, the drag sail can rely just on the acceleration provided by the SRP. When the satellite orbiting the Earth moves away from the Sun, the component of the velocity vector $\mathbf{v}_{s/c}$ along the straight line joining the Sun and the Earth ($\mathbf{v}_{s/c-Sun}$) is in the same direction as $\mathbf{a}_{SRP}$ (Figure 2.3, left). If the attitude of the sail is such that it is perpendicular to $\mathbf{a}_{SRP}$ the satellite is accelerated, so the sail must be oriented in parallel. As the satellite moves towards the Sun, the component of the velocity vector $\mathbf{v}_{s/c}$ along the straight line joining the Sun and the Earth ($\mathbf{v}_{s/c-Sun}$) is in the opposite direction as $\mathbf{a}_{SRP}$ (Figure 2.3, right). This condition is favorable for de-orbiting, so the normal to the surface of the sail points in the direction of the Sun. The effect is a gradual drop in the perigee altitude of the orbit. The orientation of the sail makes no difference if the satellite is in shadow. In this case, the radiation coming from the Earth is impeded by the interposition of the Earth between the satellite and the Sun, and $\mathbf{a}_{SRP}$ is equal to zero.

This strategy of exploiting solar pressure is used by spacecraft equipped with solar sail propulsion systems, which can travel even far from Earth thanks to the pressure exerted by the photons. A noteworthy example is the LightSail mission, which demonstrated the solar sail technology in 2015 [25, 59].

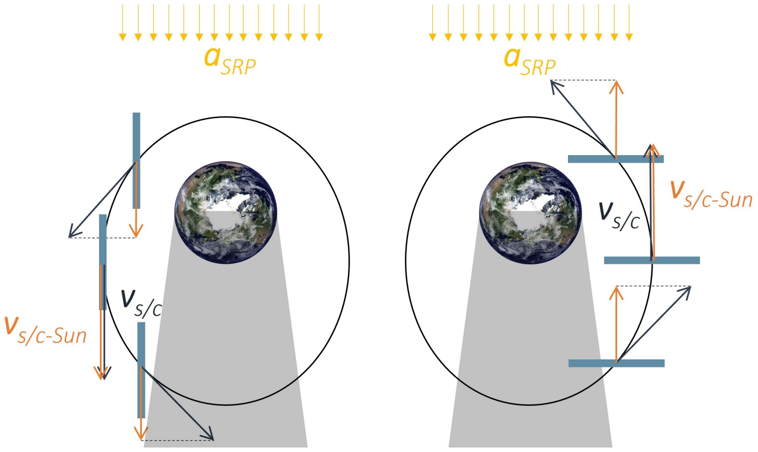

Figure 2.3: Sail orientation along the orbit.

Once the satellite drops below 1000km, the contribution of the air resistance becomes increasingly sizable as the height decreases. The attitude of the spacecraft is no longer based just on the SRP, but on the synergistic contribution of $\mathbf{a}_{SRP}$ and $\mathbf{a}_{drag}$. On one hand, the SRP depends on the distance from the source of radiation. As can be seen in Figure 2.4, the intensity of the acceleration due to SRP can thus be considered constant, since the variation of the distance between the satellite and the Sun along the orbit is negligible with respect to the distance itself. Vice versa, $\mathbf{a}_{drag}$ varies with the height because of the increasing density of the atmosphere as the altitude decreases. As a consequence, it is some orders of magnitudes smaller than $\mathbf{a}_{SRP}$ for high altitudes, while it is predominant when under about 500-600km height (Figure 2.4).

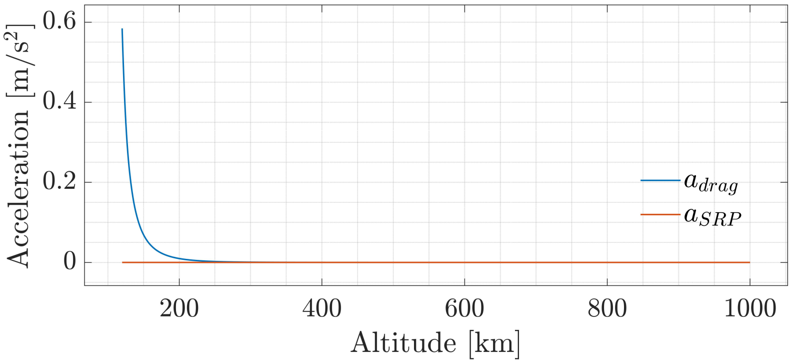

(a) $\mathbf{a}_{drag}$ and $\mathbf{a}_{SRP}$ versus orbital height.

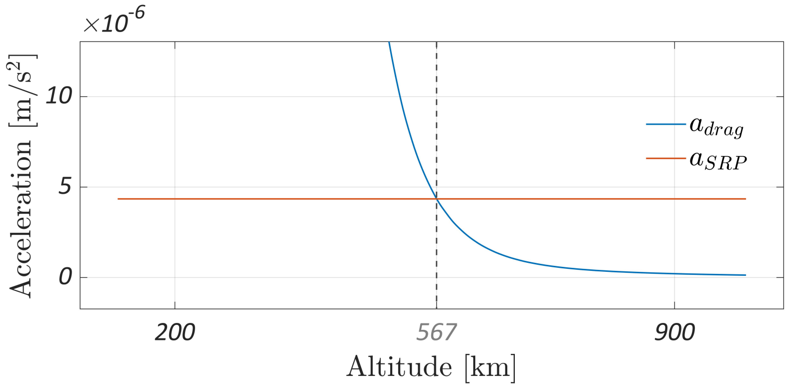

(b) $\mathbf{a}_{drag}$ and $\mathbf{a}_{SRP}$ versus orbital height. Detail of Figure 2.4a

Figure 2.4: In the image above it is evident how $\mathbf{a}_{drag}$ rapidly increases as the altitude decreases. The image below is a detail of Figure 2.4a. The zoom on the y axis underlines the altitude at which the acceleration due to air drag becomes bigger than the one due to SRP. The graphs are obtained from MATLAB® by integrating the perturbed two-body problem (Equation 2.5) with $A_{sail} = 2m^2$ and $m_{s/c} = 4kg$.

The accelerations shown in Figure 2.4 must be exploited by properly adjusting the attitude of the drag sail. The shortest possible de-orbit time is obtained if the projection of the vector sum of $\mathbf{a}_{drag}$ and $\mathbf{a}_{SRP}$ along $\mathbf{v}_{s/c}$ is maximized at each timestep (with the direction being opposite with respect to the velocity vector). If the contribution given by the air were the only one, the norm to the sail $\mathbf{n}$ would be simply oriented in the opposite direction to $\mathbf{a}_{drag}$, otherwise it would be rotated of an angle γ with respect to $\mathbf{a}_{drag}$ direction (Figure 2.5a). The greater the contribution of $\mathbf{a}_{SRP}$, the higher the shift angle γ. Figure 2.5b shows the trend of γ as the altitude decreases. For high altitudes, the main contribution to acceleration is given by SRP, so the sail continuously changes its attitude to take advantage of the solar photons. Under 400km the air drag is so predominant that the sail remains almost perpendicular to $\mathbf{a}_{drag}$. This strategy grants the shortest de-orbit time possible, but it would need continuous control of the attitude of the satellite.

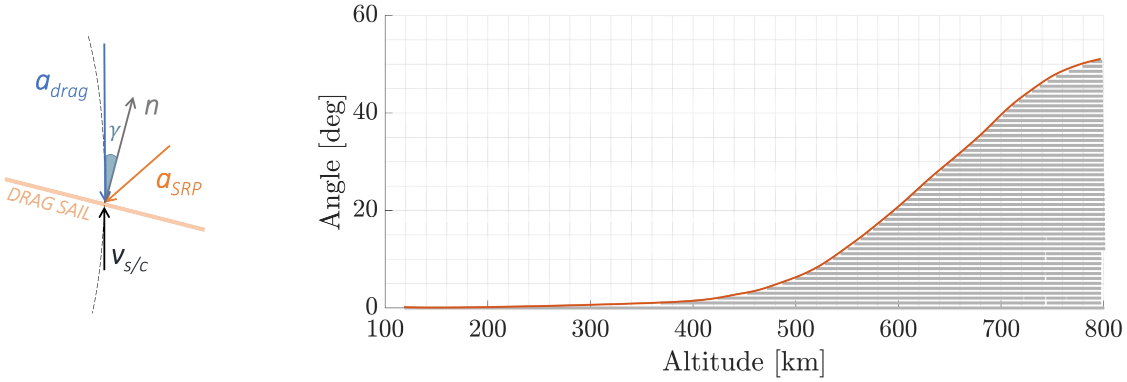

(a) (b)

Figure 2.5: Sail orientation along the orbit.

The model can be simplified by considering an attitude strategy similar to the one adopted above 1000km until the SRP effect is largely predominant. When the air drag starts contributing to the orbital decay instead, the sail is oriented perpendicularly to the pressure exerted by the air particles to maximize a_{drag}. This second strategy is less challenging in terms of attitude control and when the altitude drops under about 400-500km the air resistance is enough to make the satellite aero-stable [38].

Once the equation of motion, the environmental perturbations, and the sail model are set, the orbital motion can be integrated in MATLAB®, obtaining the size of the sail needed to de-orbit the satellite in less than 5 years.

2.4. FCC requirement: 5-year de-orbit

The choice of the mission design presented in the following lines is dictated by the recent evolution in the space activity. Since the rapid increase in the number of small satellites launched in low orbits enhanced the density of artificial objects, the need to deal with space debris in LEO is a great concern. In this framework, a CubeSat de-orbit mission from LEO is examined: the goal is to derive the minimum dimension of the sail required for a de-orbit lifetime of at most 5 years.

The 3U configuration (three units, 10x10x30 cm) is the one selected for the mission, with a mass of about 4kg. The sail is required to be stored in no more than the volume of a 1U (10x10x10 cm) and it must de-orbit the satellite in less than 5 years. Figure 2.6 shows a graphical representation of the de-orbit of a satellite from a starting circular orbit of 700km height. The orbit gradually drops over time and the reentry height is fixed at 120km (See Chapter 3.2). It can be seen from the color bar how the satellite drops slowly at high altitudes, while the de-orbit is very fast when the air density increases.

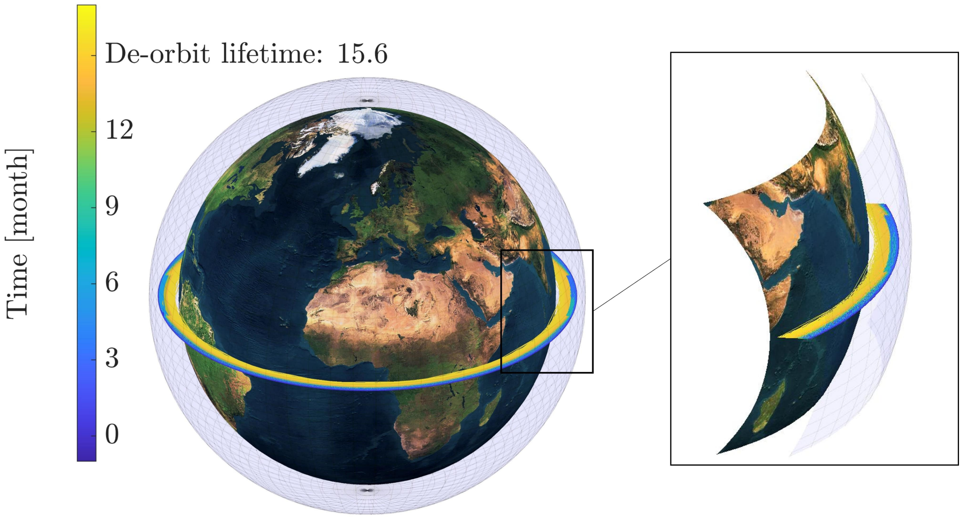

Figure 2.6: De-orbit representation from 700km altitude. The mass of the satellite is 4kg and the surface of the drag sail is 2m^2. Inclination of the orbit: 0°.

The main parameters affecting the de-orbit lifetime are the mass of the satellite and the surface of the sail. As regards the first, the higher the mass the more difficult is to deorbit the satellite. This is evident in figure 2.7 by UTIAS/SFL, which illustrates the trend of the de-orbit lifetime with respect to the altitude as the mass varies: the green line representing the heaviest satellite is the highest and the steepest of the three, indicating a greater influence of the mass on the de-orbiting. Therefore, the 5-year requirement dictated by FCC is more and more restrictive as the mass and the altitude increase.

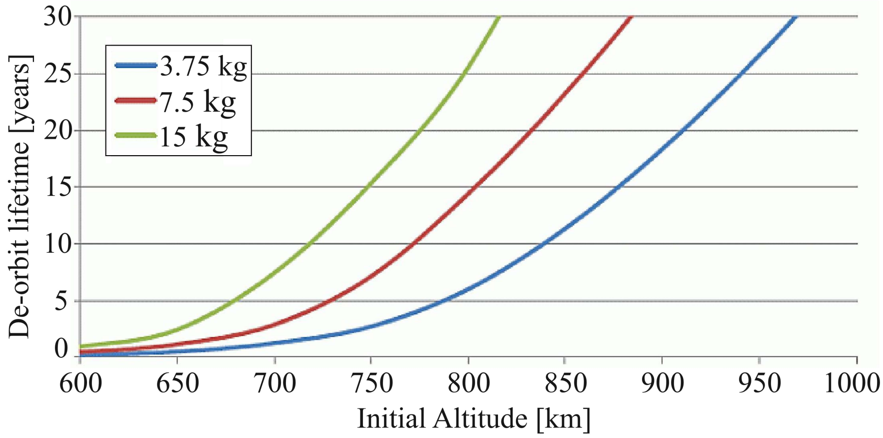

Figure 2.7: De-orbit lifetime based on a $4m^2$ drag sail (image credit: UTIAS/SFL [24]). The data are obtained from the Ansys software STK Premium Space (Chapter 2.5).

For what concerns the surface of the sail, the drag area is the key parameter for the design of the de-orbit phase. The influence of the sail size on the lifetime is computed with the aid of the de-orbit model implemented in MATLAB®. As can be seen in figure **??**, the larger the surface of the sail, the shorter the de-orbit period and the later the 5-year limit is reached. Therefore, each starting orbit is associated with a certain sail area capable of accomplishing the de-orbit within the FCC limit. As can be seen in figure **??**, while at low altitudes the severe air drag allows even small sails to properly lower the altitude of the orbit, on the other hand, the lifetime is increasingly sensitive to the variation of the sail surface as the height grows.

l

In the table below, the dimension of the sail associated with a 5-year de-orbit from different altitudes are reported. The case study considered in the following chapters for the design of the actuator refers to a CubeSat de-orbiting mission starting from an initial altitude of 750km (the one highlighted in table 2.2).

	Orbital height [km]	Sail dimension [m^2]
5-year de-orbit	600	0.13
	700	0.55
	750	**1.04**
	800	1.66
	900	3.01

Table 2.2: Size of the sail needed to deorbit the satellite within 5 years.

2.5. Model validation

The output results of the MATLAB® de-orbit software are validated with the aid of Ansys STK Premium Space software [2, 3]. STK is an advanced analytical tool providing a time-dynamic modeling environment to model complex systems inside a realistic and three-dimensional simulation. Among the possibilities that the software offers, the Premium Space package adds advanced modeling of the space environment and high-fidelity orbit propagation capabilities allowing the integration of the orbital motion of satellites. In this framework, the software can estimate the time a derelict satellite spends in orbit before it burns up in the atmosphere, with the de-orbit height assumed to be 64km (figure 2.8).

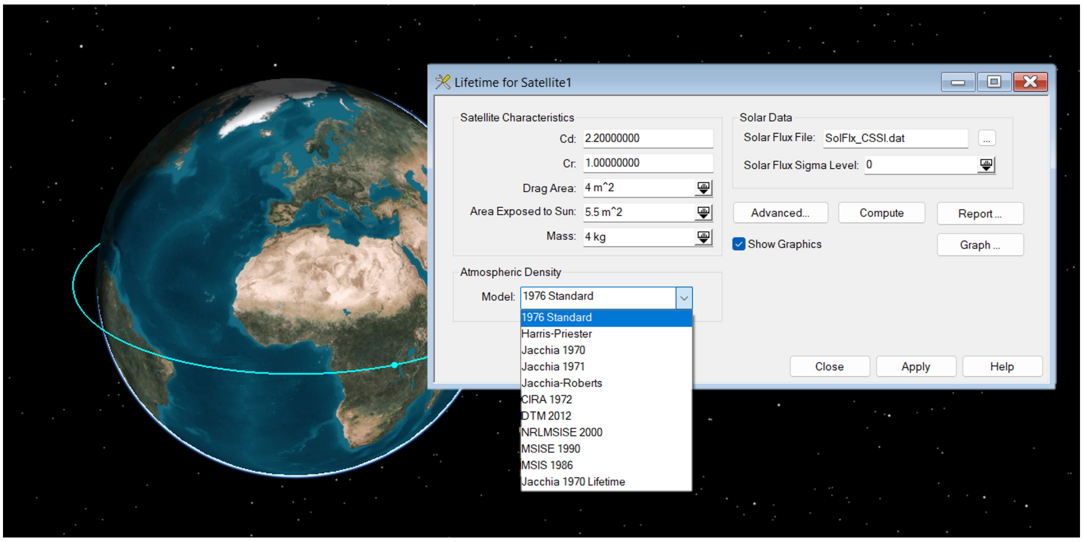
Lifetime for Satellite1

Satellite Characteristics
Cd: 2.20000000
Cr: 1.00000000
Drag Area: 4 m^2
Area Exposed to Sun: 5.5 m^2
Mass: 4 kg

Solar Data
Solar Flux File: SolFlx_CSSI.dat
Solar Flux Sigma Level: 0

☑ Show Graphics

Atmospheric Density
Model: 1976 Standard

Advanced...
Compute
Report ...
Graph ...
1976 Standard
Harris-Priester
Jacchia 1970
Jacchia 1971
Jacchia-Roberts
CIRA 1972
DTM 2012
NRLMSISE 2000
MSISE 1990
MSIS 1986
Jacchia 1970 Lifetime
Close
Apply
Help

Figure 2.8: STK lifetime tool

As stated above, the result is just an estimate of the de-orbit lifetime: although the tool is based on sophisticated orbital theory and accurate environment models, the accuracy is not better than 10% of the actual lifetime. The reasons for this inaccuracy must be

sought in the reliability of the atmospheric model and in the variability in solar activity. Despite that, the software offers the possibility to switch between a set of atmospheric models available in the literature so as to evaluate the differences in accuracy (figure 2.8 shows the available atmospheric models).
Table 2.3 collects the minimum dimensions of the sail needed to de-orbit the satellite within 5 years computed with the aid of both MATLAB® software and STK lifetime tool. The starting orbits are considered circular and the atmospheric model used in STK is the Jacchia 1970 Lifetime.

	Orbital height [km]	Sail dimension [m^2]	
		MATLAB	STK Premium Space
5-year de-orbit	600	0.13	0.12
	700	0.55	0.51
	750	**1.04**	**1.01**
	800	1.66	1.89
	900	3.01	5.58

Table 2.3: MATLAB®-STK Premium Space results comparison for different altitudes.

The outcomes of the two softwares almost coincide in the determination of the surface of the sail, resulting in a $1m^2$ size needed to de-orbit the CubeSat from the case study orbit. It is interesting to notice the growth in the difference between the two results as the starting orbital altitude increases. The reason may lie in the accuracy of the atmospheric model, being less and less reliable as the density decreases. In table 2.4 instead the comparison in the sail size as function of the orbital inclination is provided.

	Orbit inclination [deg]	Sail dimension [m^2]	
		MATLAB	STK Premium Space
5-year de-orbit from 750km	0	1.04	1.01
	10	1.04	1.02
	30	1.05	1.09
	50	1.06	1.17
	70	1.07	1.25

Table 2.4: MATLAB®-STK Premium Space results comparison for different inclinations.

As the inclination grows, the sail size must slightly increase to accomplish the de-orbit within the FCC limit. Similarly to the previous table, the results almost coincide, meaning that the Earth oblateness model in the MATLAB® software is accurate enough for the estimation of the drag sail dimension.

The validation of the de-orbit model finally provides a reliable value of the sail size to be used in the following design steps. Because of the high sensitivity of the de-orbit lifetime to the dimension of the sail (figure 2.9), from now on the size of the drag sail required to de-orbit a 4kg CubeSat from 750km circular orbit is considered as 1.5m^2.

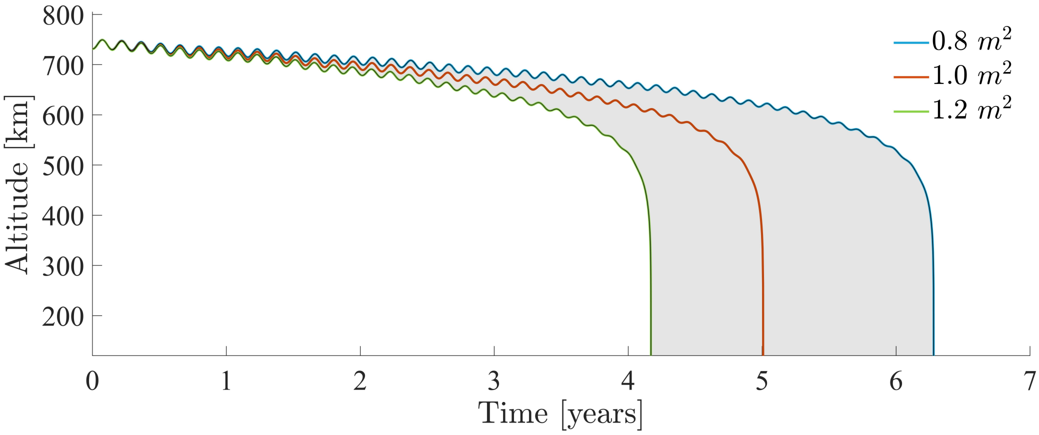

Figure 2.9: De-orbit lifetime sensitivity to sail size.

2.6. Optimized packed configuration

Once the area of the deployed sail is obtained from the propagation of the orbital motion of the satellite during de-orbit, it must be verified that it can fit within the space available in the satellite, which, in the case study, is that of a single unit (1U, 10x10x10 cm). As mentioned in Chapter 1.3.1, it is necessary to choose a crease pattern ensuring the smallest possible folded volume to fit inside that tiny space. Among the origami tessellations, the most suited for drag sail application are Miura-Ori, Kresling, Yoshimura, and Waterbomb (see table 1.3), since they can simply deploy in flat membranes starting from truly compact configurations. The choice of the best pattern is made with the aid of an optimization software implemented in MATLAB® by Martino Fossati (see bibliography at [29] for exhaustive information about the software), based on detailed geometrical properties of each of the four origami tessellation. The origami structure optimizer aims at maximize the ratio between deployed area and stored volume (A_{sail}/V_{packed}, the cost function) with the aid of the Genetic algorithm, capable to handle both non-linear constraints and integer variables. Figure 2.10 shows the user interface of the optimizer. Among the features provided by the optimizer, it requires input conditions defining the boundaries on the stored and deployed dimensions of the origami. Therefore, by setting the initial volume constraints as the size of the 1U CubeSat (10x10x10 cm), it is possible to determine the biggest possible origami storable inside a single unit.

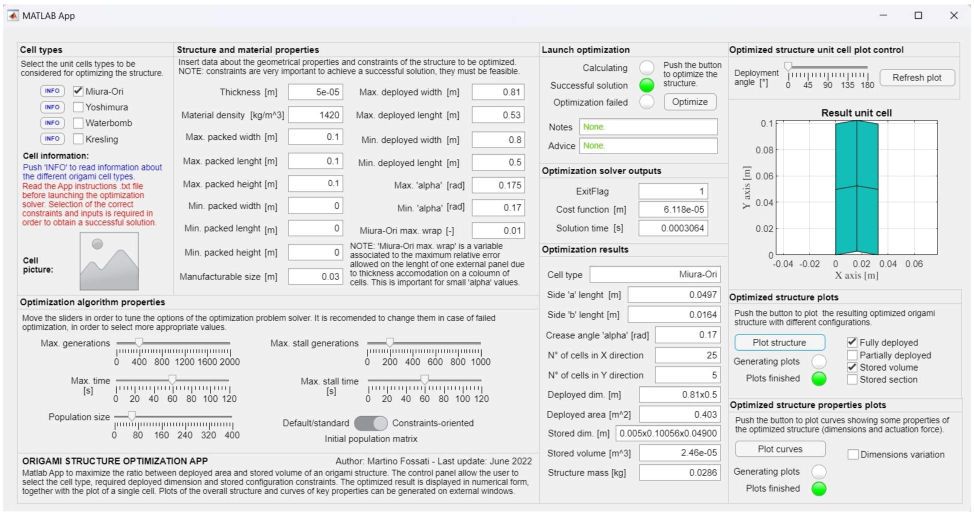

Cell types

Select the unit cells types to be considered for optimizing the structure.

- ☑ Miura-Ori
- ☐ Yoshimura
- ☐ Waterbomb
- ☐ Kresling

Cell information:

Push 'INFO' to read information about the different origami cell types.

Read the App instructions .txt file before launching the optimization solver. Selection of the correct constraints and inputs is required in order to obtain a successful solution.

Structure and material properties

Insert data about the geometrical properties and constraints of the structure to be optimized.
NOTE: constraints are very important to achieve a successful solution, they must be feasible.

Thickness [m]	5e-05	Max. deployed width [m]	0.81
Material density [kg/m^3]	1420	Max. deployed lenght [m]	0.53
Max. packed width [m]	0.1	Min. deployed width [m]	0.8
Max. packed lenght [m]	0.1	Min. deployed lenght [m]	0.5
Max. packed height [m]	0.1	Max. 'alpha' [rad]	0.175
Min. packed width [m]	0	Min. 'alpha' [rad]	0.17
Min. packed lenght [m]	0	Miura-Ori max. wrap [-]	0.01
Min. packed height [m]	0		
Manufacturable size [m]	0.03		

NOTE: 'Miura-Ori max. wrap' is a variable associated to the maximum relative error allowed on the lenght of one external panel due to thickness accomodation on a coloumn of cells. This is important for small 'alpha' values.

Optimization algorithm properties

Move the sliders in order to tune the options of the optimization problem solver. It is recomended to change them in case of failed optimization, in order to select more appropriate values.

Max. generations
Max. stall generations
Max. time [s]
Max. stall time [s]
Population size
Default/standard ● Constraints-oriented
Initial population matrix

ORIGAMI STRUCTURE OPTIMIZATION APP Author: Martino Fossati - Last update: June 2022

Matlab App to maximize the ratio between deployed area and stored volume of an origami structure. The control panel allow the user to select the cell type, required deployed dimension and stored configuration constraints. The optimized result is displayed in numerical form, together with the plot of a single cell. Plots of the overall structure and curves of key properties can be generated on external windows.

Launch optimization

Calculating ○
Successful solution ●
Optimization failed ○

Push the button to optimize the structure.

Notes: None.
Advice: None.

Optimization solver outputs

ExitFlag: 1
Cost function [m]: 6.118e-05
Solution time [s]: 0.0003064

Optimization results

Cell type: Miura-Ori
Side 'a' lenght [m]: 0.0497
Side 'b' lenght [m]: 0.0164
Crease angle 'alpha' [rad]: 0.17
N° of cells in X direction: 25
N° of cells in Y direction: 5
Deployed dim. [m]: 0.81x0.5
Deployed area [m^2]: 0.403
Stored dim. [m]: 0.005x0.10056x0.04900
Stored volume [m^3]: 2.46e-05
Structure mass [kg]: 0.0286

Optimized structure unit cell plot control

Optimized structure plots

Push the button to plot the resulting optimized origami structure with different configurations.

Generating plots ○
Plots finished ●

- ☑ Fully deployed
- ☐ Partially deployed
- ☑ Stored volume
- ☐ Stored section

Optimized structure properties plots

Push the button to plot curves showing some properties of the optimized structure (dimensions and actuation force).

- ☐ Dimensions variation

Generating plots ○
Plots finished ●

Figure 2.10: Origami optimization software, user interface [29].

The result is that the maximum dimension of the origami fitting the volume of the satellite is about 16m^2, well beyond the size of the drag sail needed to de-orbit the satellite. Such a size is provided just by Miura-Ori, Kresling, and Yoshimura tesselation (with minor differences between the three), while the low A_{sail}/V_{packed} ratio of the Waterbomb configuration hardly produces large deployed surfaces. Since the dimension of the sail seems to be not a bottleneck of the design, the choice of the best pattern is made on the completely unfolded geometry and the deployment simplicity.

As regards the first aspect, it is important to notice that the origamis expand more along one of the two directions, as shown in figure 2.11

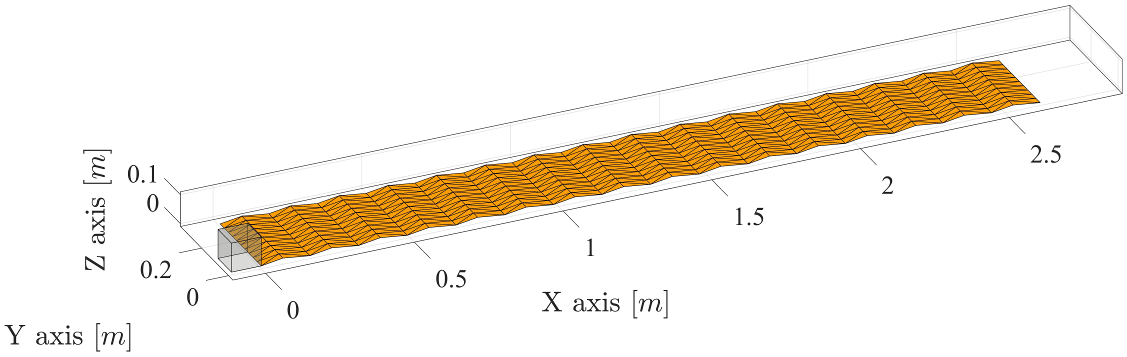

Figure 2.11: Predominance of the deployment along X axis (Kresling tessellation).

The large and uneven extension of the sail is problematic for actuation and rigidization purposes, so the more regular the geometry of the deployed origami, the more suitable it is for the application. Among the tessellations, Miura-Ori is the one ensuring the largest deployment along the Y direction (see figure 2.12) and, consequently, the most even geometry of the drag sail. However, the Y-side length is dictated by the size of the angle α (see figure 1.9a) which in turn influences the thickness accommodation effect [29]. In particular, the more α diminishes, the more the Y-side length increases but, on the other hand, the more α approaches zero, the more the external facets wrapping around the internal stacked layers shorten while packed. The thickness accommodation effect is avoided by imposing 5° as the minimum size of the α angle, with a minimum loss in the length of the Y-side of the drag sail.

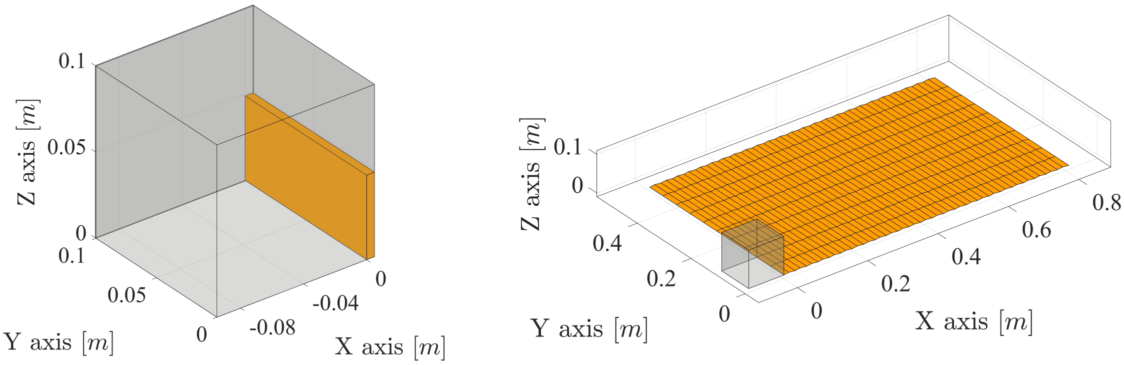

(a) (b)

Figure 2.12: Miura-Ori packed and deployed configurations.

Miura-Ori origami is fortunately also the one with the simplest unfolding kinematics: the vertices of the faces translate parallel to the plane of the drag sail during deployment, without involving out-of-plane movements and rotations like the other three tessellations. This aspect is crucial for the design of the actuation system since simple kinematics ensures better control in the deployment phase and a simpler architecture of the actuator.

The geometry of the case study drag sail will be thus based on the Miura-Ori tesselation and it is extracted from the origami optimization software described in the previous lines. This nominal outcome will be given in input to the design of the actuator, since it is necessary to know both the size of the sail to be opened and the geometrical features of each cell of the origami. As regards the first parameter, the bigger the dimension the more the inertia and the stronger the actuator must be. On the other hand, the geometry of the tessellation gives information about the way the actuator couples with the sail.

In order to extract a first, rough nominal origami drag sail from the origami optimization software, the constraint parameters are first established. First of all, the size of the packed sail must be confined within a volume of 10x10x10cm, while the total unfolded surface must be 1.5m^2 wide. However, the de-orbit device can be split into multiple separated modules deploying separately in all directions around the spacecraft. This solution is preferable because the difficulty in deploying a large sail is certainly greater than that of a smaller one. Moreover, splitting into multiple modules improves the reliability of the subsystem in the event of damage. Therefore, the constraint on the unfolded dimension refers to the single modules of about 0.4m^2 each (for a total number of four units). What is missing from the complete definition of the constraints are the thickness and the density of the material of which the sail is made. The density considered is that of Kapton, which is 1420kg/m^3, while the thickness is 10μm, in agreement with literature references and datasheets about coated Kapton for sail application. Finally, since the tessellation that has been selected is Miura-Ori, the constraint on the lower value of the size of the angle α is set as 5°.

The results of the optimization are shown in table 2.5. It is worth noting that the sail size required by the deorbiting design is well within the 1U volume, occupying only about 1% of the available space. The four modules can thus fit inside the spacecraft and the free space can be occupied by rigidization or deployment systems or even other subsystems.

Optimized drag sail module	
Side a length [m]	0.0279
Side b length [m]	0.0155
Crease angle α [deg]	8
Deployed surface [m^2]	0.38
Total deployed surface [m^2]	1.52
Total stored volume [m^3]	$5.2 \cdot 10^{-5}$
Percentage of occupied volume (1U)	5.2%
Number of cells in X direction	20
Number of cells in Y direction	11

Table 2.5: Optimized origami drag sail. The geometry refers to the one of a single module.

3 | Thermal analysis

The actuation system for the deployment of the drag sail is based on the shape memory effect occurring as a consequence of the temperature-induced transformation of SMA. The thermal analysis of the de-orbiting system is thus crucial to verify whether the actuation of shape memory material can be achieved without resorting to Joule effect heating. Moreover, the temperatures reached over the orbit and the aerodynamic heating at reentry are fundamental parameters driving to the choice of sail material.

In the following chapter, the thermal analysis is divided into two phases. At first, the analysis is focused on the deployed system, analyzing the thermal cycles along the orbits and the temperatures reached upon reentry. The study of the deployment phase is then presented in the final section.

3.1. Thermal cycle along the orbit

The satellite's exposure to solar radiation is not uniform along the orbit. Assuming a perpendicular orientation of the sail to the orbital velocity vector, the incident angle of the photons on the surface of the membrane changes continuously. In addition to this, the relative position of the Earth with respect to the Sun and the satellite can generate shadow regions in which the temperature of the satellite is bound to decrease. All these phenomena lead to continuous variations in the temperature of the sail and can be inferred analytically by adding to the de-orbit lifetime MATLAB® code the integration of the heat transfer model, giving as a result the temperature at each timestep.

The heat transfer model focuses attention on the flow of thermal energy that takes place whenever a temperature difference between two bodies occurs. According to the first law of thermodynamics, the total energy in a closed system remains constant, although it may be converted from one form to another. The formulation is thus the following:

$$\frac{\partial U}{\partial \tau} = \sum \dot{Q} + \sum \dot{L} \tag{3.1}$$

where U is the internal energy of the system and $\dot{Q}$ and $\dot{L}$ are respectively the heat and the work exchanged with the surrounding. By considering the density ρ of the system constant, no work exchange with the surroundings, and no internal heat sources, equation 3.1 can be integrated over the volume and written as:

$$\rho V c_V \frac{\partial T}{\partial \tau} = \sum \dot{Q} \tag{3.2}$$

since the thermal energy per unit mass can be expressed as a function of the specific heat at constant volume c_V:

$$du = c_V dT. \tag{3.3}$$

T is the temperature of the system whose trend over time is to be computed, in this case, the drag sail. Assuming that the volume, the density, and the specific heat of the sail are known, it is necessary to determine the sources of heat exchange to which it is subject. Among the ones affecting satellites in the space environment, the main source is the radiation generated by the Sun, computed as:

$$\dot{Q}_{Sun} = \alpha \dot{E}''_{Sun} A_{cross}. \tag{3.4}$$

in which α is the absorption coefficient of the sail while $\dot{E}''_{Sun}$ is the heat rate per unit surface exerted by the Sun at the distance of one astronomical unit (1AU=1.49598×10^8km), equal to 1358W/m^2.

Another source of radiation is the one coming from the Earth, divided in the reflected solar radiation and the radiation directed emitted by the planet. The two contributions are computed as follows:

$$\dot{Q}_{alb} = \alpha a_{Earth} \dot{E}''_{Sun} A_{cross} \tag{3.5}$$

$$\dot{Q}_{Earth} = \alpha \dot{E}''_{Earth} A_{cross} \tag{3.6}$$

As can be seen in equation 3.5, the amount of radiation reflected depends on the albedo of the Earth, denoted by a_{Earth} and ranging from zero to one. High values of a correspond to high reflectivity power, vice versa when the value is close to zero the reflection is almost null. In this specific case, the albedo of the Earth is between 0.37 and 0.39. As regards equation 3.6 instead, the heat rate per unit surface $\dot{E}''_{Earth}$ is less powerful than $\dot{E}''_{Sun}$ and strongly depends on the orbital height. These aspects are evident in table 3.1, which highlights the trend of the radiation and shows the predominance of the contribution of the solar one.

Altitude $[km]$	Direct solar radiation $[W/m^2]$	Earth albedo $[W/m^2]$	Earth radiation $[W/m^2]$
500	1358	600	150
1000	1358	500	117
2000	1358	300	89
4000	1358	180	62
8000	1358	75	38

Table 3.1: Heat rate per unit surface as a function of the altitude.

As opposed to the incoming radiation, the spacecraft exchanges energy with deep space by emitting in all directions. It can be shown that this emission depends on the temperature of the body as stated in the Stefan–Boltzmann law, according to which the total energy radiated per unit surface area across all wavelengths per unit of time is directly proportional to the fourth power of the body's temperature T:

$$\dot{E}_T''^B = \sigma T^4 \tag{3.7}$$

with $\sigma = 5.67 \cdot 10^{-8}\mathrm{W/m^2K^4}$. Equation 3.7 refers just to the black bodies (whence the apex ^{B}), an ideal emitter ($\varepsilon = 1$) and perfect absorber ($\alpha = 1$) whose intensity of emission is the same in all the directions and does not depend on the surface conditions. In case of heat exchange between the drag sail and deep space, the sail can be treated as a small body enclosed in a much larger one, from which the following formulation derives:

$$\dot{Q}_{ds} = -A_{tot}\varepsilon\sigma\left(T_{sail}^4 - T_{ds}^4\right). \tag{3.8}$$

However, the emission from deep space to the sail is almost completely negligible, since the baseline temperature of outer space is 2.7K. Therefore, considering the total emitting surface equal to $2A_{sail}$, the heat transferred to deep space is computed as:

$$\dot{Q}_{ds} = -2A_{sail}\varepsilon\sigma T_{sail}^4. \tag{3.9}$$

Equations 3.4, 3.5, 3.6, 3.9 represent the overall contribution to the heat exchanged by the spacecraft with the surroundings. In order to compute the temperature of the sail it is necessary to set up an approach for the modelization of the heat transfer. Since the sail is flat during flight and is homogeneous in geometric and physical properties, the temperature can be considered uniform and the sail is condensed in a single node.

This model is called the single-node lumped parameter approach and allows writing the following energy balance on the single-node sail:

$$\rho V c_V \frac{\partial T}{\partial \tau} = \dot{Q}_{Sun} + \dot{Q}_{alb} + \dot{Q}_{Earth} + \dot{Q}_{ds}. \tag{3.10}$$

The integration of this differential equation leads to the results reported in the figure below. It can be noted the relationship between the attitude of the sail and its temperature: as the angle between the normal to the surface of the sail and the direction of the Sun decreases (blue dashed line in figure 3.1) the cross-section area A_{cross} grows as well and the temperature rises accordingly. On the other hand, the minimum temperature is reached when the sail is parallel to the solar radiation. An additional source driving the temperature variation is the presence of the shadow region due to the relative position of spacecraft, Earth and Sun. When the sail enters the shadow cone of the Earth, the infrared radiation coming from the planet is the only source of heating and the temperature drops gradually. As soon as the sail is once again hit by the Sun's rays, the temperature starts rising rapidly.

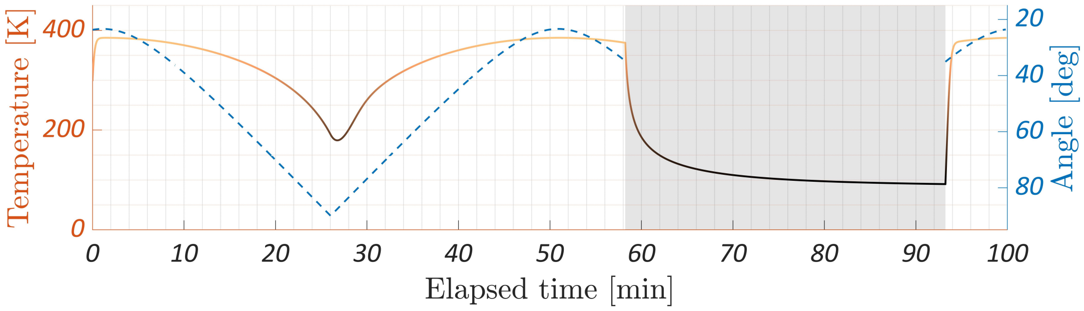

Figure 3.1: Sail temperature trend over one orbit. The orange line indicates the temperature of the sail: the more the color tends to yellow the higher the temperature. The gray area highlights instead the shadow region along the orbit. $\alpha = 0.4$, $\varepsilon = 0.15$.

The optical properties of the sail strongly influence the maximum and minimum temperatures reached. As the absorption coefficient α grows, the amount of radiation absorbed coming from the Earth and Sun raises and the sail achieves higher temperatures. On the contrary, as the emissivity ε grows the radiation emitted toward deep space increases and the average temperature along the orbital path decreases. The material adopted in this case study is Kapton, which is widely used in the design of drag sails in general. Its glass transition temperature is approximately 400°C, so surface optical properties can be set suitably to allow for increased absorption as needed without jeopardizing the structural integrity of the sail. As regards aluminum-coated Kapton, the ratio between the absorptivity and the emissivity of the external surface is typically 3.5 [20].

3.2. Satellite burning in the atmosphere

The radiative energy transfers with Earth, Sun, and deep space are not the only contributions to sail temperature variations. In addition to them, the high-speed interaction with the upper rarefied layers of the atmosphere produces the aerodynamic heating of the spacecraft. The analytical model of this effect is described in equation 3.11 [39, 40]:

$$\dot{Q}_{drag} = \frac{1}{2}\bar{\alpha}\rho_{atm}\|\mathbf{v}_{rel}\|^3. \tag{3.11}$$

The extent of $\dot{Q}_{drag}$ depends on the density of the atmosphere ρ_{atm} and the relative velocity between air particles and spacecraft $\|\mathbf{v}_{rel}\|^3$. Even if the orbital speed is extremely high, the order of magnitude of the density in orbit ranges between 10^{-12} and 10^{-16}, making this contribution almost negligible over 200km altitude. Below this limit, ρ_{atm} rises sharply and consequently also the heat exchanged, leading to a sudden increase of the temperature. This trend is well represented in figure 3.2, where the colored line indicates the temperature of the sail during reentry, while the blue line the atmospheric density. The two quantities rise together as the altitude lowers, up to the limit to which the satellite burns up. Assuming the sail is made of aluminized Kapton (glass transition temperature about 400°C, 673K), the temperature limit is reached at an altitude of about 110km (the one indicated in red in the figure). This justifies the stop condition on the accomplishment of the de-orbit, set in the MATLAB® code as 120km.

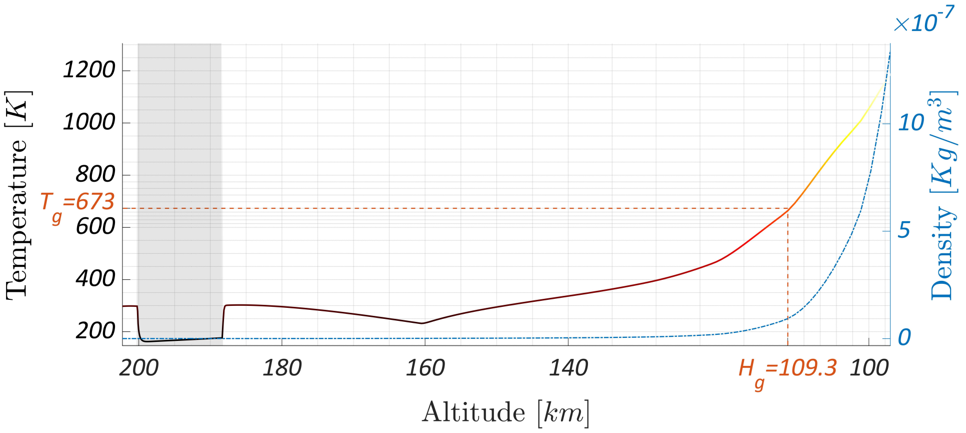

Figure 3.2: Sail temperature during reentry. T_g is the glass transition temperature of Kapton and H_g the corresponding height at which this temperature is reached.

The coefficient $\bar{\alpha}$ is "a measure of the extent to which the mean energy of the molecules that hit the surface and are reflected or reemitted is accommodated toward an energy corresponding to the temperature of the wall" ([34]) and it is called thermal accommodation coefficient. Its value depends on the assumptions made in the impact modeling: in the case of perfect specular reflection of the gas molecules the value is $\bar{\alpha} = 0$, while for diffuse reflection $\bar{\alpha} = 1$. For engineering applications, the diffuse assumption has proven to be more realistic and the value for the impact of air on metal is generally considered equal to 0.9.

3.3. Thermal analysis during deployment phase

The thermal analysis conducted in the previous paragraphs refers to the completely unfolded sail. The temperature trend during the deployment is different from the above results instead, since the surface of the sail is completely or partially packed, causing an alteration in the heat transferred by radiation (figure 3.3). On one hand, the heat exchanged becomes a function not only of the attitude but also of the deployment angle. As a consequence, the cross-section area diminishes (see equations 3.4, 3.5, 3.6) and some of the faces could be obscured by the others. This effect can simply be considered in the design phase by changing the impact angle of the radiation onto the surface of the sail. On the other hand, in the folded configuration the radiation emitted by the sail is not completely directed toward deep space since a partial self-radiation mutually involves the faces of the origami.

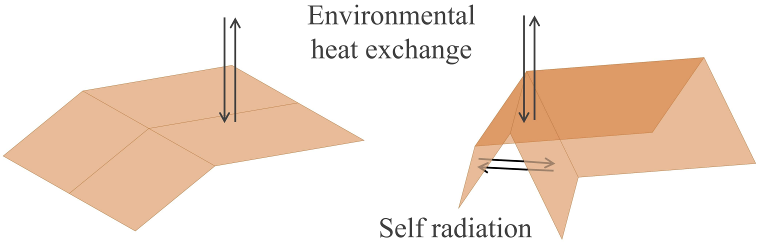

Figure 3.3: Radiation heat transfer for deployed and partially folded Miura-Ori origami.

The determination of the self-radiation is thus essential for thermal analysis during the deployment. In this case, equation 3.9 changes and becomes

$$\dot{Q}_{ds} = -2A_{sail}\varepsilon\sigma T_{sail}^4(1 - F_{self}). \tag{3.12}$$

where F_{self} is the view factor between the faces of the sail tesselation, indicating the portion of the radiation that leaves the sail and reaches the sail again. In the same way, in a partially deployed configuration, the solar radiation reflected from the surface hits the sail again resulting in the following expressions, where ρ_{sail} is the reflection coefficient of the drag sail (for simplicity, multiple reflections are not modeled):

$$\dot{Q}_{refl} = \rho_{sail} \dot{E}''_{Sun} A_{cross} \tag{3.13}$$

$$\dot{Q}_{abs} = \alpha_{sail} \dot{Q}_{refl} F_{self}. \tag{3.14}$$

The view factor depends on a variety of parameters, such as the deployment angle and the shape of the faces of the origami, but also on the relative position of multiple faces. Therefore, the computation of F_{self} is not simple and it can be carried out in two ways. The first strategy is based on the discretization of the surface into small differential surfaces. The view factor between two of them is computed as follows:

$$dF_{1\to 2} = \frac{\cos\theta_1 \cos\theta_2}{\pi s^2} dA_2. \tag{3.15}$$

in which s is the segment indicating the distance between the differential areas dA_1 and dA_1, while θ_1 and θ_2 are the angles between the normal to dA_1 and dA_1 and s. The global view factor from the first to the second surface is given by the double integration of equation 3.15 over the areas of the surfaces.

The second approach is simpler than the analytical one just described and it is adopted in the current chapter for the computation of the Miura-Ori view factor. The procedure relies on the Monte Carlo method, a computational algorithm used to model the probability of a certain outcome with the random generation of samples [52, 62].

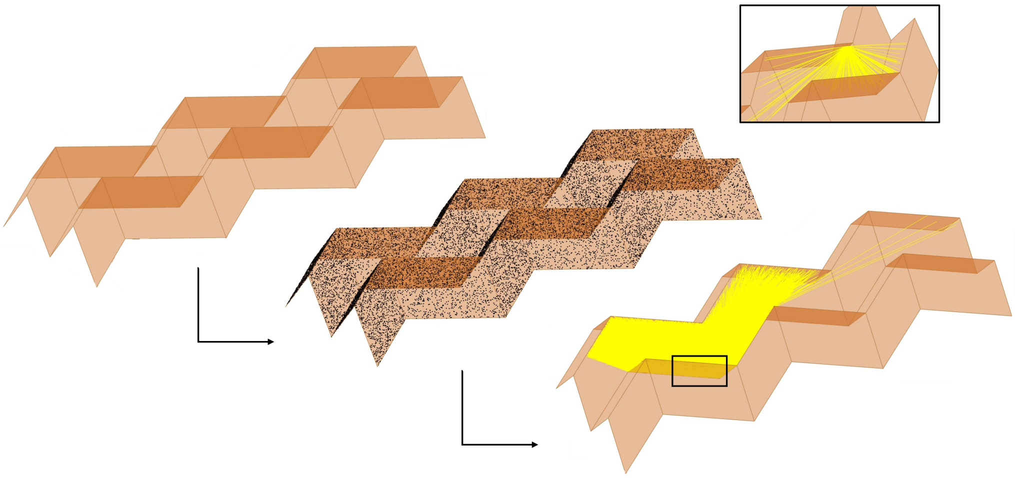

Figure 3.4: Monte Carlo method for the computation of the Miura-Ori self view factor. The zoom box shows the rays generated from a single point.

The approach consists of the random generation of rays from the surface of the radiating face and the verification of how many of them hit the surface of the sail (in percentage). Figure 3.4 helps in the understanding of the way the Monte Carlo method is applied. A three-dimensional geometric model of a portion of the sail is implemented in MATLAB® starting from the geometric characteristics of the Miura-Ori pattern [29]. The facets are isolated and a certain number of points are randomly generated on each of them (the black dots in figure 3.4). These will be the starting points from which the rays representing the radiation will be conducted. The rays are randomly generated too and the direction in which they exit the surface is bounded into a hemisphere centered on the starting point and lying on the face. Finally, the modeling of the radiation is completed by extending the shooting of the rays to every point lying on the sail. Once all the rays are generated, the second step is to determine whether they hit the sail itself or they spread out into the surrounding space. In order to do so, the model evaluates the number of times the rays arrive at the other faces of the origami, discarding the times when the shooted surface is hidden by another face. The outcome of the analysis is a value representing the total number of rays hitting the surface of the sail, n_{self}. The ratio between n_{self} and the total number of shooted rays n_{tot} gives the required self view factor:

$$F_{self} = \frac{n_{self}}{n_{tot}}. \tag{3.16}$$

It is important to notice that the value just obtained refers to one face alone. The results are indeed dependent on the face from which the rays are shooted: in the faces close to the perimeter of the sail the self view factor is less than the innermost one since the rays are less likely to impact the surface of the sail (figure 3.5).

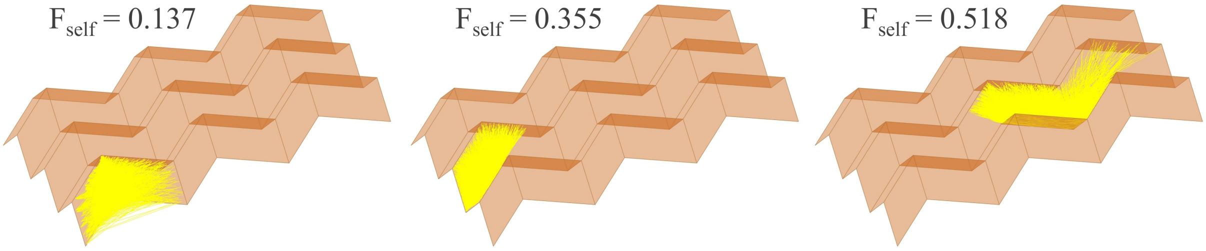

Figure 3.5: Self view factors of different Miura-Ori origami faces.

However, the small dimension of the faces compared with the overall size of the drag sail and the high number of cells making up the membrane justifies the choice of adopting the

single-node approach for the thermal model of the deploying sail. The global F_{self} will be computed as an average value of the self view factors of each face of the Miura-Ori origami, which will be close to the view factor of the innermost faces.
Figure 3.6 shows the trend of the self view factor as the deployment angle changes. As expected, the value of F_{self} for a completely packed origami is equal to one, while it gradually decreases as the sail unfolds up to a value of zero for the completely deployed sail.

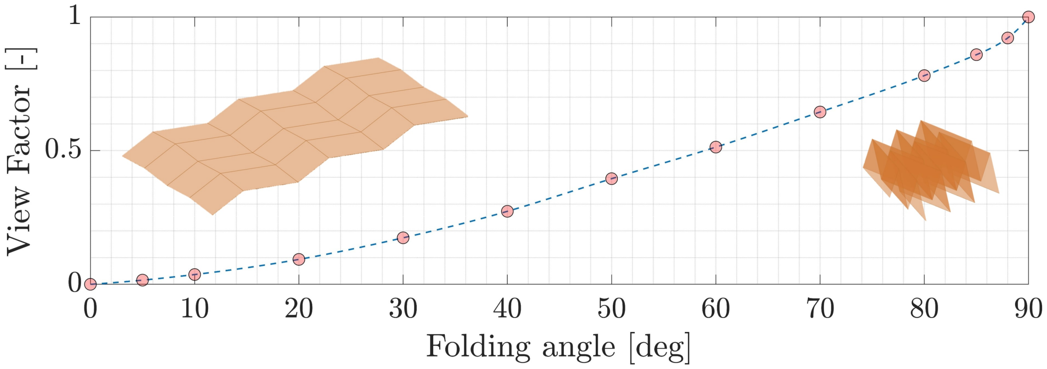

Figure 3.6: Self view factor as a function of the deployment angle θ.

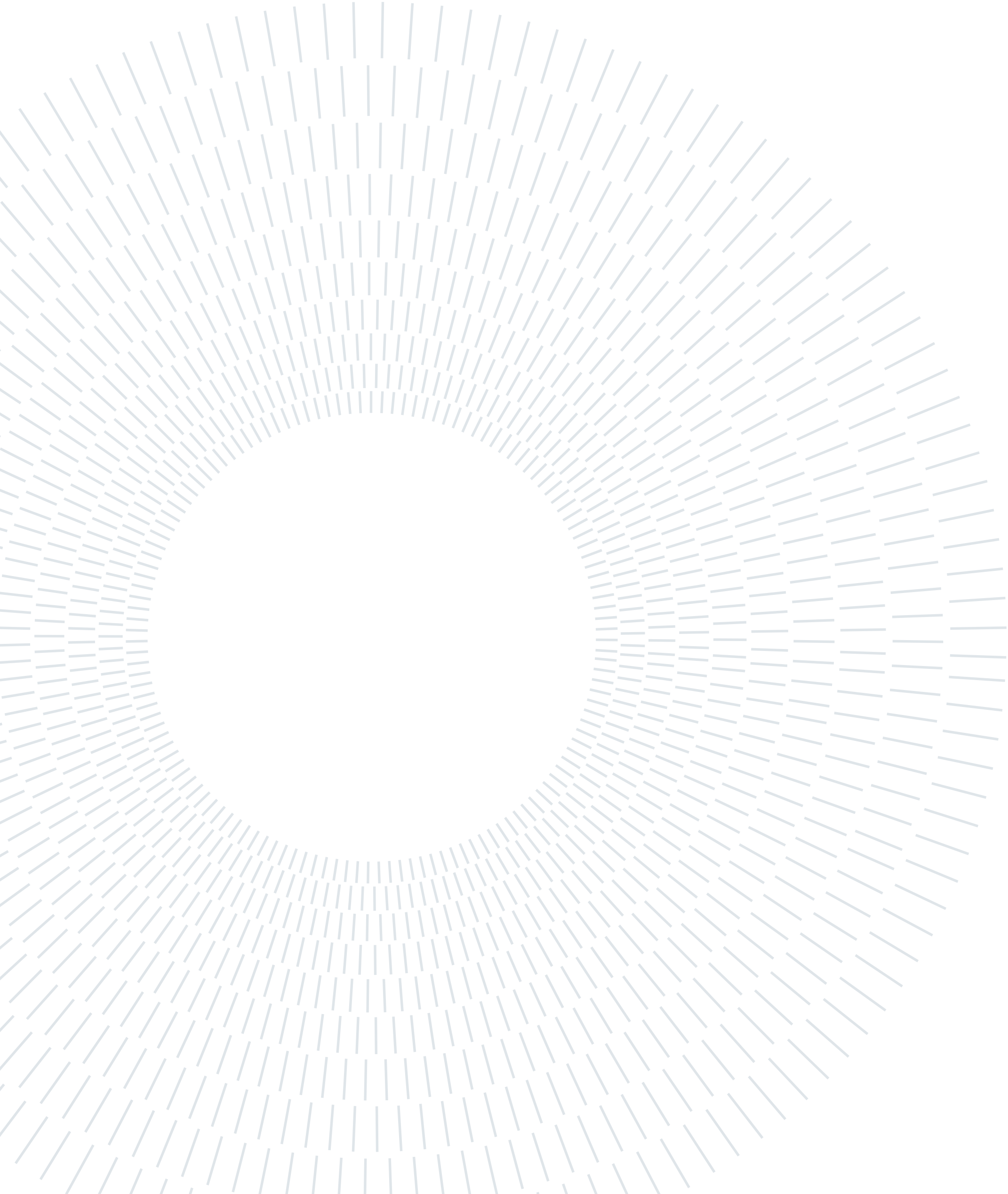

4 | Miura-Ori multibody dynamics

The design of the actuation device must go through the simulation of the dynamics of the overall sail-actuator system. In this way, if the dynamic model is accurate, it is possible to determine the effectiveness of the actuation system and refine its design. In the current lines, the dynamic model of the sail is provided with the aid of the combination between MATLAB® and Adams (by Hexagon) software. The modelization is based on the multibody dynamic of the origami faces, whose interconnection is established by the model of the fold lines. Afterward, the following chapters will take care of integrating the actuator into the dynamic model of the sail, so as to finally be able to simulate the complete model.

4.1. Origami dynamic modeling

The recent growth of interest in origami structures for space applications has promoted the study of the deployment characteristics of such systems. Depending on the information to be obtained from the analysis, there are different origami modeling strategies that can be implemented which aim at determining motion, force, velocity, acceleration, stress, strains, time, and other features involved in the deployment.

When the motion of the origami while unfolding is the main concern of the analysis, the kinematic models are implemented to determine how the structure folds and unfolds. In this origami model, the faces of the structure are usually assumed to be rigid while the creases are modeled as revolutes joints. Because of the simplicity of the model, the computational effort is less than in other methodologies and the solver is very quick. However, the model is not predisposed to the analysis of the forces and torques that generate the motion, so it is not suited to design the sail-actuator system.

In this framework, the dynamic model is the appropriate one to involve the forces actuating the deployment of the membrane structure. The modelization strategy is similar to the kinetic one since the faces of the origami are considered rigid, but the deployment simulation is now initiated through the forces provided by the actuator, while the joints between the faces account for the rigidity of the fold line. The system is described by

Lagrange's equations of motion plus a set of kinematic constraints [65]:

$$\mathbf{M}\ddot{\mathbf{q}} + \mathbf{f}_D + \mathbf{\Phi}_q^T \lambda - \mathbf{Q} = 0 \tag{4.1}$$

$$\mathbf{\Phi}(\mathbf{q}, t) = 0. \tag{4.2}$$

In the formulation above, $\mathbf{q}$ is the vector of generalized nodal coordinates of the bodies that make up the system, $\mathbf{M}$ is the mass matrix, $\mathbf{f}_D$ is the damping force vector and $\mathbf{Q}$ is the vector of generalized forces. $\mathbf{\Phi}$ is the complete set of kinematic constraints and λ is the Lagrange multiplier vector corresponding to the constraints $\mathbf{\Phi}$. Finally, $\mathbf{\Phi}_q$ is the derivative of the constraint conditions with respect to the generalized coordinates, known as Jacobian:

$$\mathbf{\Phi}_q = \frac{\partial \mathbf{\Phi}}{\partial \mathbf{q}}. \tag{4.3}$$

The strength of the dynamic analysis is the ability to model complex systems ensuring low computational efforts, so a variety of dynamic models of origami structures are proposed in the literature. Fulton and Schaub [30] proposed the dynamic simulation of the deployment of a Miura-Ori cell for space application. Bowen [43] developed the analysis of an Origami-inspired Starshade with the aid of a multi-body dynamic strategy. Zhang and Liu [64] developed a dynamic software for the simulation of a Miura-Ori origami and validated the results with Adams software. Bhuiyan [7] conducted a parametric dynamic analysis on the deployment of flasher origami. Among the software designed for the dynamic analysis of complex systems, ADAMS (Automatic Dynamic Analysis of Mechanical Systems) [36] is the best and most widely used multibody dynamics simulation software, and it will be presented in detail in the following section.

Despite the effectiveness of these methods, the multi-body dynamics approach has to deal with a simplification that is relevant in the modelization of gossamer structures and thin membranes in general, i.e. the assumption of rigid faces. Because of the great flexibility of this kind of system, the Finite Element Analysis (FEA) is perfectly suited when information regarding stress and strains internal to the faces is required. These softwares, like the well-known Abaqus, provide detailed design of the dynamics of the deployment but the computational cost is way higher than the one of the most common multi-body dynamics simulators. In this specific case, the high number of bodies (the origami faces) and hinges between them limit the ability of FEA to perform parametric analysis and iterations toward different solutions. As a consequence, this approach is more indicated as a validation tool of the multi-body dynamic analysis.

Given the reasoning above, the modelization of the drag sail at the following lines is based on the multi-body dynamics simulation with the aid of ADAMS.

4.2. Miura-Ori model in ADAMS

According to the definition of multi-body systems, the origami drag sail must be subdivided into single rigid faces, each of them interconnected by a joint modeling the behavior of the creases while deploying. The geometry of the cells is taken from the origami optimization software implemented by Martino Fossati, the results of which are reported in chapter 2.6. The pattern of the Miura-Ori is highly regular and the faces are all equal to each other (adjacent parallelograms), which simplifies the modelization. The unit cells are formed by four faces, each of them sharing its four sides with four further faces. The total number is thus 880 since the two sides of the drag sail have 20 and 11 cells respectively. Figure 4.1 shows a graphic model of a portion of the 20x11 cells sail that is designed for the satellite de-orbit.

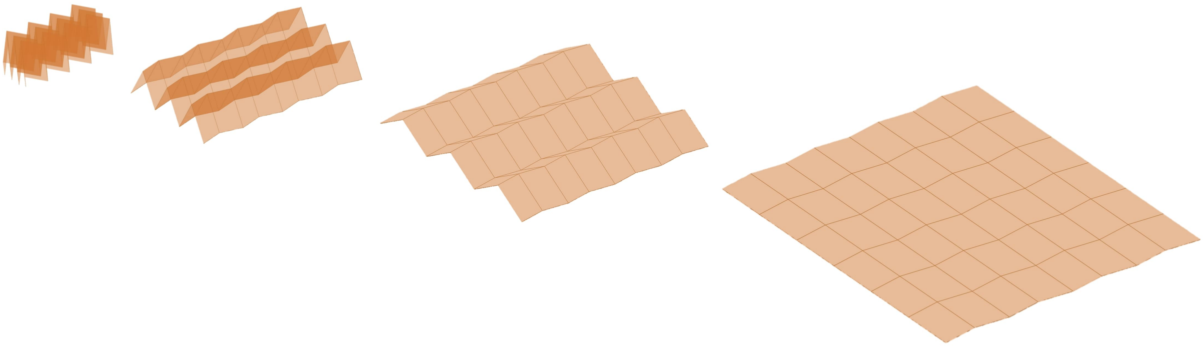

Figure 4.1: Miura-Ori drag sail optimal geometry.

4.2.1. Miura-Ori faces

The multi-body model of the origami faces requires information about the physical properties of the material (density, size, thickness, Young's modulus, and Poisson's ratio) and the coordinates of the vertices of each face at the initial state.

As regard the first requirement, the drag sail is made of Kapton® coated on both sides with a thin aluminized film. Because of the small thickness of the aluminum coating compared to that of the polymeric structural membrane, the density and the mechanical properties selected are those of Kapton®. In particular, the density is 1420kg/m^3, while the Young's modulus and the Poisson's ratio are respectively 2.5GPa and 0.33 [21].

Once the physical properties are set, the coordinates of the vertices are obtained from the following Miura-Ori geometrical relations (figure 4.2), where the first subscript refers to the face of the unit cell (the one indicated with the circled number) while the second to the number of the vertex. Figure 4.2 below helps in the comprehension of the formulations.

$$
\begin{aligned}
f_{1,1} &= [0,\ l,\ 0] & f_{2,1} &= \left[\frac{w}{2},\ u+l, 0\right] \\
f_{1,2} &= \left[\frac{w}{2},\ l+u,\ 0\right] & f_{2,2} &= [w,\ l,\ 0] \\
f_{1,3} &= \left[\frac{w}{2},\ l+u-a\cos\delta,\ h\right] & f_{2,3} &= [w,\ l-a\cos\delta,\ h] \\
f_{1,4} &= [0,\ l-a\cos\delta,\ h] & f_{2,4} &= \left[\frac{w}{2},\ l+u-a\cos\delta,\ h\right] \\
\\
f_{3,1} &= \left[\frac{w}{2},\ l+u-a\cos\delta,\ h\right] & f_{4,1} &= [0,\ l-a\cos\delta,\ h] \\
f_{3,2} &= [w,\ l-a\cos\delta,\ h] & f_{4,2} &= \left[\frac{w}{2},\ l+u-a\cos\delta,\ h\right] \\
f_{3,3} &= [w,\ 0,\ 0] & f_{4,3} &= [w/2u+l-2a\cos\delta 0] \\
f_{3,4} &= \left[\frac{w}{2},\ l+u-2a\cos\delta,\ 0\right] & f_{4,4} &= [0,\ 0,\ 0]
\end{aligned}
\tag{4.4}
$$

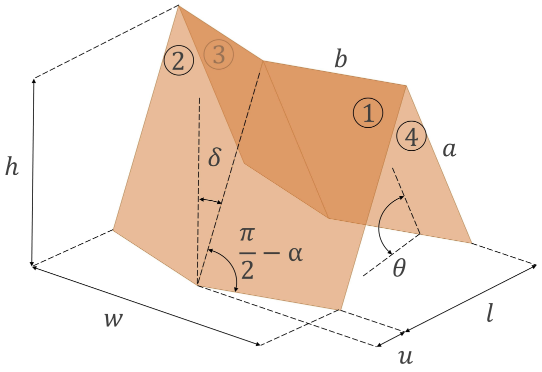

Figure 4.2: Single cell geometry.

The coordinates reported above are the ones of just the first cell, but the others can be obtained by simply shifting the x and y coordinates according to the reference cell position $(N_x,\ N_y)$, as shown in equation 4.5.

$$
\begin{aligned}
x_{shift} &= w\,(N_x - 1) \\
y_{shift} &= 2a\cos\delta\,(N_y - 1)
\end{aligned}
\tag{4.5}
$$

The initial configuration of the origami sail in the dynamics simulation is not completely packed (θ_0=90°) because of both computational and physical reasons. At first, when θ_0 is exactly equal to 90° the model is at an inversion point and the computation fails to determine the dynamics of the system. Secondly, it is expected that once the sail is freed from the satellite volume a certain amount of elastic potential energy allows a partial reopening of the sail. Therefore, being these two effects in agreement on establishing the initial aperture angle, θ_0 will be set a bit smaller than 90°, as shown in the picture.

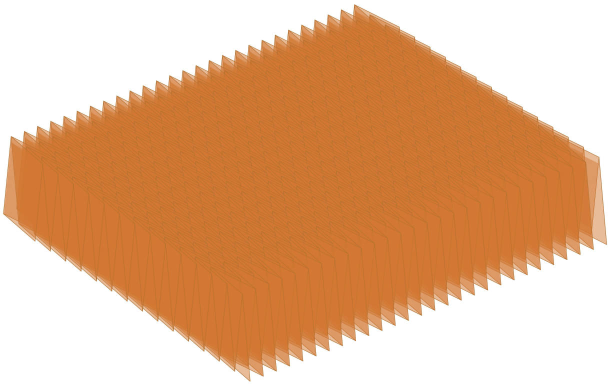

Figure 4.3: Multi-body dynamics simulation: drag sail initial configuration (θ=89°).

4.2.2. Miura-Ori crease lines

Once the faces are properly modeled in ADAMS, the same is done for the creases of the origami tessellation. Each face shares an edge with another establishing a rotational constraint along the crease. In ADAMS, this is translated into revolute joints granting the rotation about the folding line while blocking the other two rotational and three translational components. Even if this kind of constraint faithfully represents the relative movement of the faces, simulation issues can arise because of the high number of redundant constraints. A redundant constraint is a constraint that can be removed without changing the result of the simulation. The importance of detecting and removing them is the avoidance of consuming extra computational effort by obtaining a reduced model. Moreover, a high number of redundant constraints can cause computational issues blocking the simulation of the sail's dynamics. To solve this problem, two solutions are investigated. The first consists of a degrees-of-freedom analysis leading to the reduction of the constraint, comprising both spherical type and cylindrical in addition to revolute. A second strategy involves the bushing forces modeling, joint-like elements with three translational and three rotational degrees of freedom, each of them associated with a stiffness value. By setting the stiffness of the not-allowed degrees of freedom to very high values and the one of the rotation along the crease line as zero, the result is an equivalent revolute joint not causing simulation issues.

The definition of the interface between the faces is not sufficient to define the dynamic model of the sail. In fact, the sole introduction of these joints is not different from what is done in the kinematic analysis, whereas the dynamic simulation requires a modelization of the behavior of the crease as the origami deploys. After the polyimide (Kapton®) is compressed to be folded, the release of the folding load leads to a partial recovery of the elastic strain, while the extremely localized plastic deformation generated in the crease region leaves a residual fold pattern. As a consequence, the more the actuator moves the faces relative to each other, the more the crease tries to oppose the deployment, exerting a torque along the line. Although the source of this real stiffness is still unknown, in the literature there exist models trying to explain the behavior of the crease. According to Dharmadasa, Mallikarachchi, and López Jiménez [16], the moment generated by the crease is proportional to the difference between the deployment angle θ and the initial fold angle ϕ. In particular, the relation between these two quantities is reported in equation 4.6:

$$M = kW\,(\theta - \phi) \tag{4.6}$$

where M is the moment opposing the the deployment, W is the length of the crease, and k is hinge stiffness, measured in N$\cdot$deg^{-1}, whose value is about 0.0001 for Kapton® films of 25μm thickness. The damping effect associated with the crease behavior is evaluated too, expressing the damping coefficient as follows:

$$c = 2\zeta\sqrt{KI} \tag{4.7}$$

where K is the stiffness of the crease and I is the mass moment of inertia of the origami face about the folding line. The damping ratio ζ is considered equal to 0.05 [10], while a better understanding of this value can be investigated in future works.

Accordingly, the crease behavior is modeled in ADAMS as an equivalent torsional spring-damper element acting along the folding line, and the complete model becomes the one represented in the sketch below.

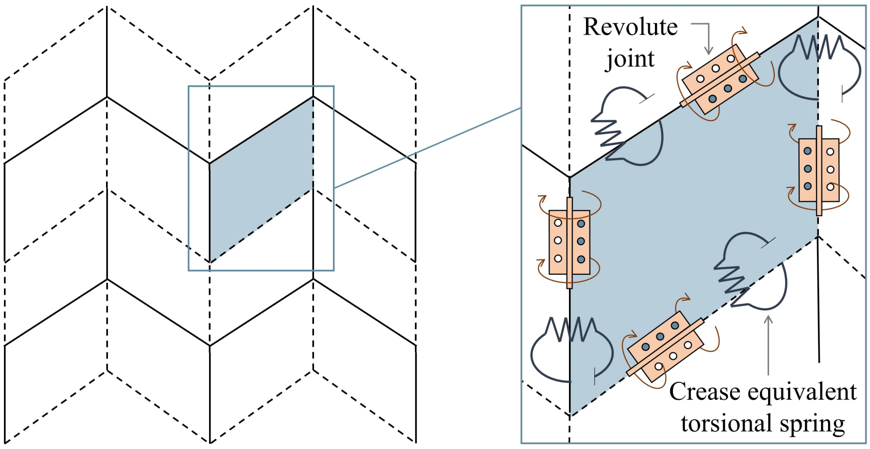

Figure 4.4: Miura-Ori multi-body dynamics simulation: crease model.

The consequences of the crease-equivalent torsional spring model are not only reflected on the moment generated at the junction of multi-body elements, as the stiffening effect of the crease couples with the deformation of the faces of the origami (figure 4.5). If the stiffness of the membrane is much greater than the one of the crease, the faces remain straight and the deployment involves just the aperture of the initial angle ϕ. On the contrary, in the case of high crease stiffness, the angle remains constant during deployment while the faces deform as a result of the application of the load. Lastly, when the two effects are comparable, both the deformation of the structure and the aperture of the angle are affected.

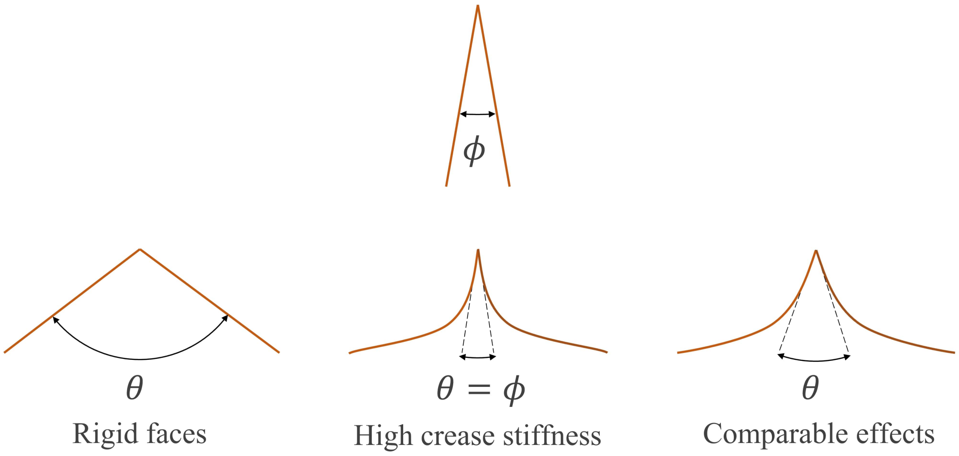

Figure 4.5: Effects of the crease-face stiffness relationship during deployment.

The multi-body dynamics simulation carried out in ADAMS assumes the faces of the origami as rigid bodies, therefore the first case on the left in figure 4.5 is the one exploited in the model. Future developments could validate the results with FEA softwares accounting for the flexibility of the structure.

4.3. ADAMS-MATLAB integration

The description of the origami drag sail model is thus complete. The following step is the implementation of the system into ADAMS, the multi-body dynamics simulation software selected for the purpose. ADAMS comes with a detailed graphical interface (as shown in figure 4.6) which gives the possibility to directly design the three-dimensional system within its main window. Although the CAD tools set is quite complete, ADAMS offers the possibility to import pre-designed models from other CAD software (like SolidWorks). This solution is often preferable since those programs are specifically designed for the implementation of even complex systems and the procedure may be simpler.

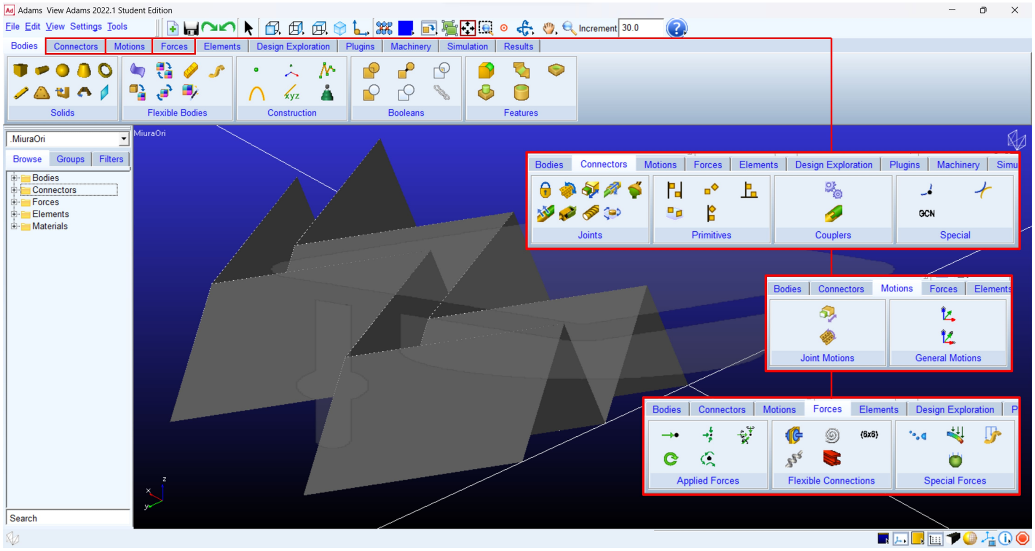
Adams View Adams 2022.1 Student Edition
File Edit View Settings Tools
Increment 30.0
Bodies
Connectors
Motions
Forces
Elements
Design Exploration
Plugins
Machinery
Simulation
Results
Solids
Flexible Bodies
Construction
Booleans
Features
MiuraOri
Browse
Groups
Filters
Bodies
Connectors
Forces
Elements
Materials
Search
Joints
Primitives
Couplers
Special
Joint Motions
General Motions
Applied Forces
Flexible Connections
Special Forces

Figure 4.6: ADAMS graphical interface.

The Miura-Ori structure is composed of simple thin membranes in the shape of parallelograms, so the CAD design of the units is not demanding. A certain level of complexity is yet provided by the high number of faces and the need to simply parametrize the design of the origami, which varies according to the mission specifications. Accordingly, the modelization on ADAMS or CAD software may be thus laborious and hardly scalable.
The proposed solution is the implementation of a software built in MATLAB capable of generating ADAMS-readable files containing information about the drag sail model. The advantages of this approach are the simple scalability of the design and the possibility to directly receive in input the results of the origami optimization algorithm described in Chapter 2.6 to return the dynamic model to be read by ADAMS (figure 4.7)

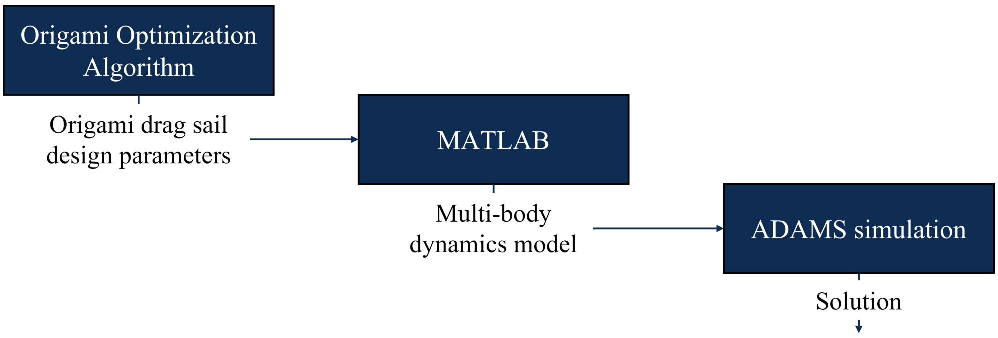
Origami Optimization Algorithm
Origami drag sail design parameters
MATLAB
Multi-body dynamics model
ADAMS simulation
Solution

Figure 4.7: Drag sail dynamics analysis: block scheme.

The procedure starts with the generation of an OBJ file from MATLAB collecting the coordinates of the vertices of the Miura faces. This file is the base of the ADAMS model and allows importing the geometrical features and the disposition of the faces, whose vertex coordinates are computed from equations 4.4 and 4.5.

Once the geometry is set, the dynamic model is deepened with the introduction of the sail material's physical characteristics, the origami's thickness, the joints between the faces, the crease model, and the constraints between the sail and the spacecraft. These features are collected in individual *.cmd* files that contain a set of ADAMS commands defining a model, performing a specific function, or collecting a set of procedures. The logic behind the architecture of the files is documented in detail in the Adams View Command User's Guide [37]. The number of *.cmd* files generated for modeling the sail is five: *material.cmd*, *extrusion.cmd*, *joints.cmd*, *crease_model.cmd*, and *ground.cmd*. The first collects the physical properties of Kapton®, that is to say Young's modulus, Poisson's ratio, and density. The two-dimensional profile imported from the OBJ file is then extruded in *extrusion.cmd* of an amount equal to the thickness of the sail. The mass and the inertia are automatically computed in ADAMS from volume and density data assuming that the origami is homogeneous. The revolute joints between the faces are generated in *joints.cmd*, while the crease-equivalent torsional spring is modeled in *crease_model.cmd*. The torsional stiffness of the torsional spring is set constant and equal to the value of kW (from equation 4.6). Finally, the number of degrees of freedom is reduced by fixing the first face of the first cell of the origami geometry at ground (*ground.cmd*). In this way, the translation of the sail is blocked and the actuator deploys the origami without inducing any rigid motion. The OBJ and the five *.cmd* files are combined together in a single *.cmd* file which will be the input of the ADAMS simulation.

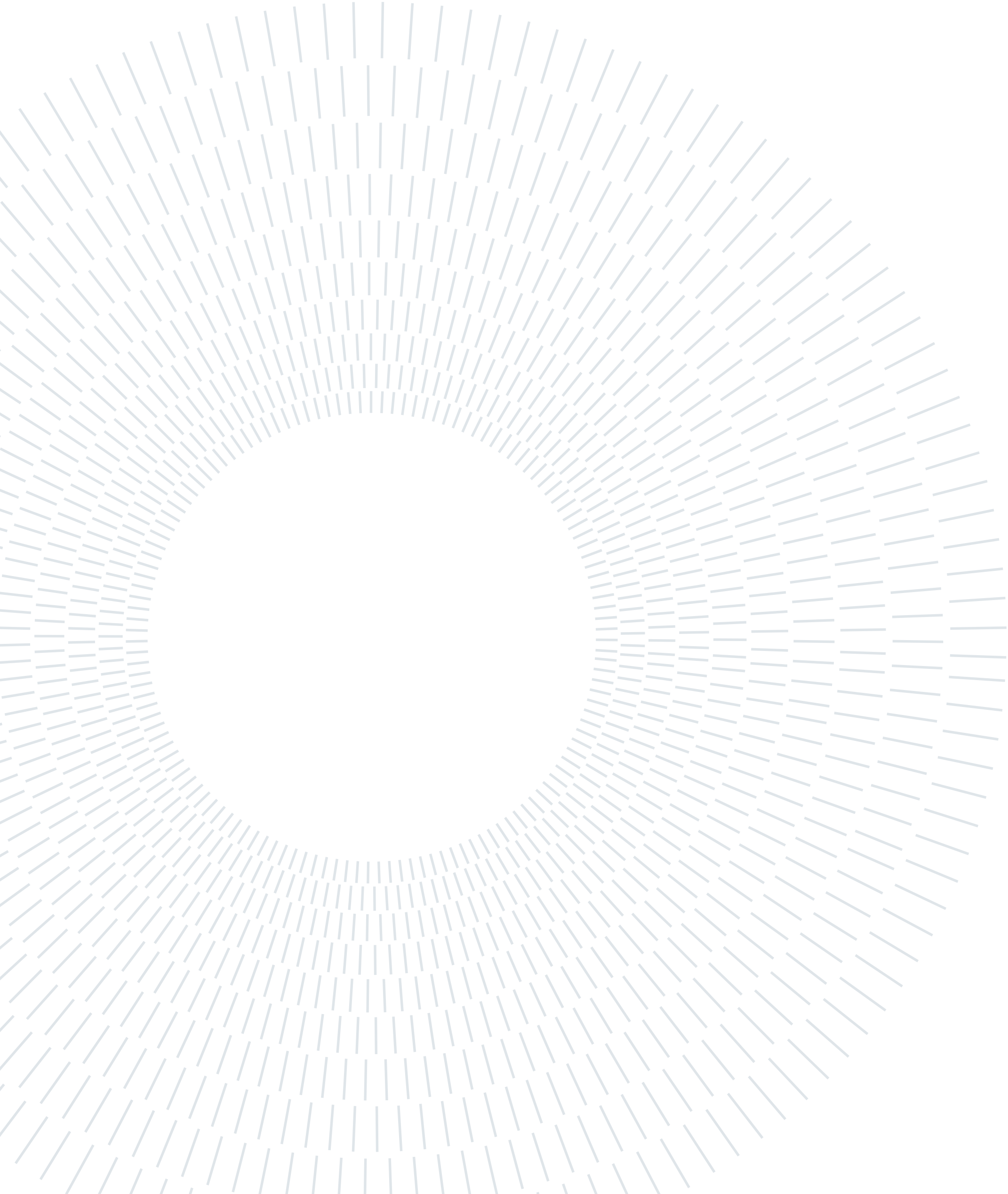

5 | Passive actuator design

The purpose of this chapter is to illustrate the configuration and design of the passive actuator. The goal is to create a system capable of deploying the origami solar sail without the aid of energy supplied by the satellite, therefore with the sole effect of heating by solar radiation. Shape memory alloys are proposed for this scope. In the first section, an overview of this class of materials is provided, focusing on both one-way and two-way memory effects. Afterwards, the stress-strain-temperature model is presented and applied to the design of the drag sail actuator.

5.1. Foundamentals of shape memory alloys

Shape memory alloys (SMA) are classified as "smart materials" because of their ability to perform specific actions in response to external stimuli. In particular, they are capable to recover their original shape if exposed to external heating rising the temperature of the alloy over a certain limit. This ability makes SMA suitable to be used as actuators since, if the shape recovery is completely or partially restrained, the alloy generates considerable stresses on the constraint.

The salient feature of SMA behavior is the gradual phase change variation with temperature between the parent crystallographic phase, the austenite, and the product crystallographic phase, called martensite. As regards the first, austenite is the high temperatures stable state formed by a highly symmetric cubic crystallographic structure with high elastic modulus. On the contrary, the structure of the martensitic phase is less symmetric, with a lower elastic modulus and lower stable temperatures. Because of the structural asymmetry, there exist 24 different variants of the martensite crystallographic orientation. In the case of a free-stress state, they all coexist in the twinned state, while under stress conditions the alloy deforms and only the variants that best adapt to the stress remain. Figure 5.1 shows a representation of the SMA phases structure, with a hint of how it is possible to switch from one to the other. The transformation from twinned to detwinned phase is promoted by an external stress, while the reverse transformation is not simply obtained by releasing the state of stress since it is necessary to go by the austenitic phase.

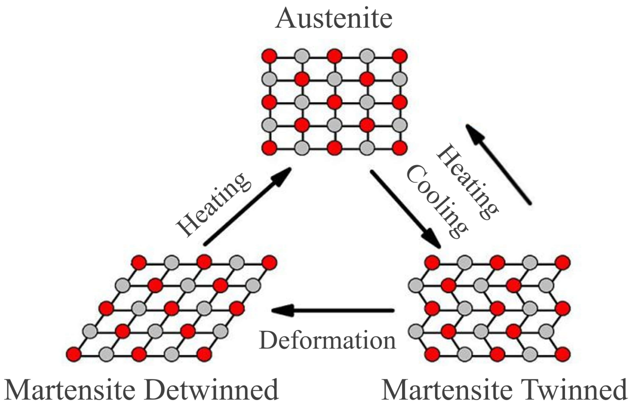
Austenite
Heating
Heating
Cooling
Deformation
Martensite Detwinned
Martensite Twinned

Figure 5.1: Crystalline structure of the three phases of shape memory alloys.

These relationships between the three phases of the SMA are the basis of the shape memory effect governing the design of smart materials. Therefore, temperature, stress and martensitic fraction (ξ) are the main variables characterizing the transformation. In particular, the shape memory can be divided into one-way effect and two-way effect.
In the first case, the alloy can recover a single deformation imposed at low temperatures through the transformation from the martensitic to the austenitic phase. Figure 5.2a represents the successive stages of the transformation. The alloy is initially subjected to a stress orienting the variants in the detwinned phase. Once the stress is released, the resulting detwinned phase retains a certain amount of prestrain, coming from the transformation of the alloy. The prestrain is recovered by rising the temperature over the austenite finish temperature A_f at which the transformation from martensite to austenite is completed. The cycle ends with the return to the starting condition by lowering the temperature and can be repeated multiple times.

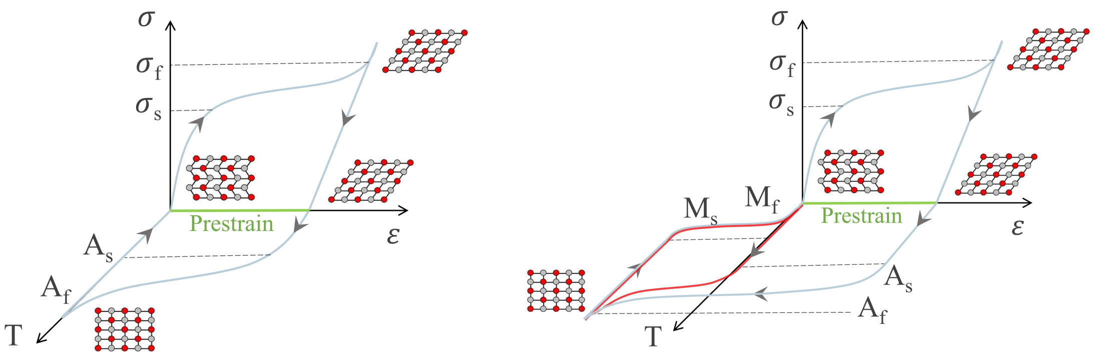
σ
σf
σs
Prestrain
ε
As
Af
T
σ
σf
σs
Ms
Mf
Prestrain
ε
As
Af
T

(a)

(b)

Figure 5.2: One-way (5.2a) and two-way (5.2b) shape memory effect.

The two-way memory effect is quite different from the previous one since, as a consequence of the training process, the material shows the ability to change its shape repeatedly by simply raising and lowering the temperature. The first phases of the cycle are the same as for the one-way effect. However, as the temperature increases above A_f, the macroscopic shape in the austenitic phase appears to be not the same as the starting one (figure 5.2b). In order to return to the initial configuration the temperature must lower under the martensite finish temperature M_f. Although the two-way memory effect can be exploited without imposing a prestrain after each cycle, the process is subjected to fatigue and the actuation force is less than the one provided by the one-way effect.

The relationship between the stress-temperature condition and the alloy phase is clearly represented in the phase diagram shown in figure 5.3. At low temperatures, the twinned martensitic phase is stable and can be turned into detwinned martensite through the application of stress (ξ=1). Vice versa, austenite is stable at temperatures higher than A_f (ξ=0). In the regions bounded by the transition temperatures, the percentage of martensite in the structure is governed by the progress of the transformation (0<ξ<1).

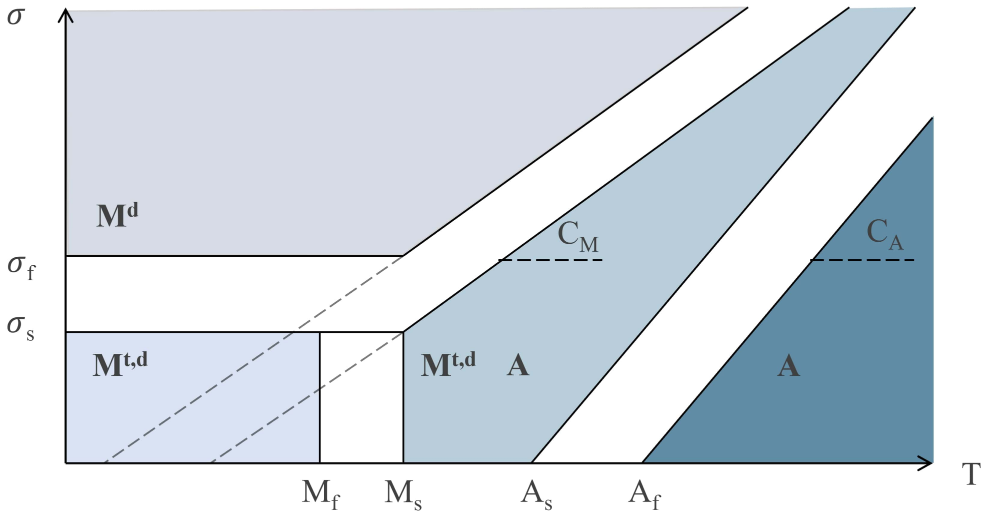

Figure 5.3: Shape memory alloy phase diagram.

Among the shape memory alloys, the most common is Nitinol (Nickel-Titanium Naval Ordnance Laboratory), an equiatomic alloy of nickel and titanium characterized by great strain recovery (about 5-8%) and a wide range of transformation temperatures (from -30°C to +170°C, compatible with LEO environment). The features of the alloy can be tuned by slight variations in the relative percentage of nickel and titanium in the crystalline structure. Furthermore, the possibility of being made in strips, wires and tubes, contributes to making these alloys versatile and suitable for a variety of applications.

5.2. Drag sail passive actuator

Chapter 1.3.2 briefly presents an overview of the systems adopted to deploy a drag sail. The main issues arising in the design are the minimization of the packed volume and the identification of the actuation mechanism. Shape memory alloys can meet both the requirements being compact, light components with respect to the common mechanical systems and providing relatively high actuation forces. These characteristics make the SMA suitable to be embedded in the structure of the sail itself, limiting the space occupied inside the satellite. Moreover, avoiding the use of mechanical deployment systems that act by pulling the sail outside the satellite reduces the risk of sail breakage and failure of the de-orbiting mission. The purpose of this section is to propose a suitable material and configuration for the embedded actuator whose feasibility will be verified in the following chapter regarding the overall simulation of the system.

5.2.1. Nitinol properties

Among the metals showing shape memory effect, Nitinol is the best-known and most used in engineering applications because of its mechanical and thermal properties. The composition consists of nickel and titanium, the ratio of which determines the physical characteristics of the alloy. The stability, for example, varies over wide temperature ranges based on the percentage of nickel, as shown in the figure 5.4a. The most noteworthy category is that of equiatomic alloys, concentrated closely around 50% Ni. The manufacture of nitinol equiatomic components requires great care as a small change in the ratio of nickel to titanium drastically changes the physical properties (figure 5.4b).

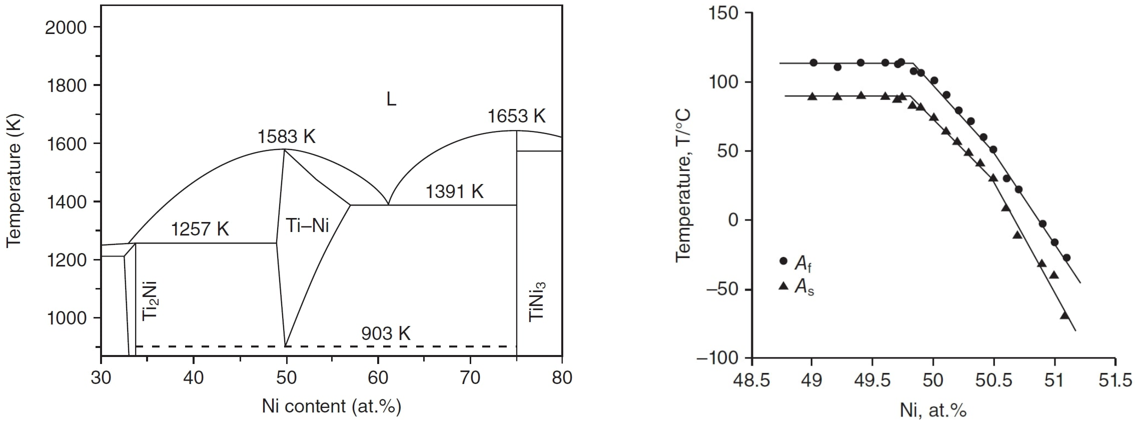

(a) (b)

Figure 5.4: Ti-Ni alloy characteritics.

An amount of nickel above 50% produces low transformation temperatures and makes the alloy suitable for applications in the superelastic field, whereas a SMA with a more significant percentage of titanium is better suited for exploiting the shape memory effect. Using nitinol of the first type as an actuator represents an excellent solution for deploying the drag sail. The working principle is based on the strain release of the superelastic alloy, which pulls the sail outside the satellite box like a spring. Although it is highly effective, the content of this thesis focuses on the detailed analysis of the shape memory effect actuator because of its innumerable advantage. In fact, the deployment can occur both actively and passively by passing a current in the wire (Joule effect) or exposing it to solar radiation. In both cases, it is certain that the deployment is more gradual than the simple release of elastic energy. Furthermore, it is possible to induce partial openings and controlled deployment of critical or functional parts of the membrane structure by tuning the Joule effect heating. Finally, an antagonistic configuration of several nitinol components allows the reversibility of the opening and closing process. This advantage is accentuated when combined with the multi-stable characteristics of origami patterns, which drives the possibility to have a discretized morphing between precise configurations. On the contrary, if a completely passive system is preferred, solar radiation heating replaces the Joule effect and the sail becomes energetically independent from the spacecraft. The latter solution is the one of interest for the scope of the thesis and will be numerically investigated in Chapter 6.

Another feature to examine is the invasivity of the actuation system on such a thin structure as origami. Beyond the high corrosion resistance and the wide range of activation temperatures, equiatomic nitinol is extremely interesting because of its fine grain and low anisotropy, which allows its production in wires and strips [19]. As a matter of fact, the thickness (or diameter in the case of wires) of these components can even go down to a few micrometers, making it compatible with the thickness of the sail membrane. Figure 5.5 presents two examples of application making use of small-sized SMA wires and exploiting the shape memory effect.

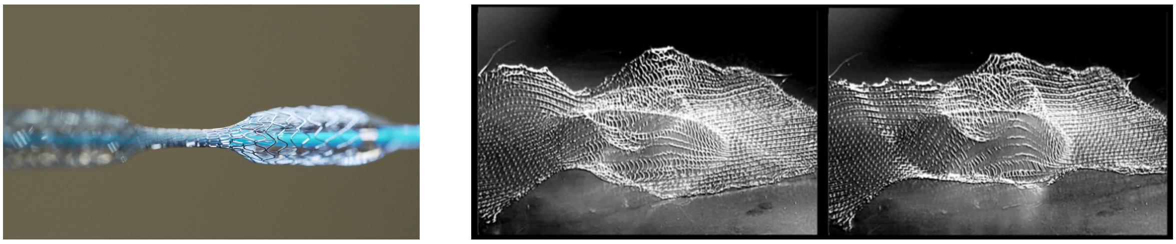

(a) Nitinol wires in nanotechnology.

(b) Nitinol functional textiles.

Figure 5.5: Examples of the application of small-sized SMA components [35, 60].

5.2.2. SMA actuator configuration

Thanks to these properties of shape memory alloys, it is possible to think of a solution that concerns the embedment of the actuator directly into the sail. Since the faces of the origami are modeled as perfectly rigid bodies hinged along the creases (Chapter 4), the actuator must act on the folding lines to open the angle between the faces.

There exist different configurations of the wire capable of exerting the required force differing according to the way the actuator work. The first concerns the use of an axially shrinking wire embedded in the membrane, widely used in composite materials. In this case, the material selected for the design of the sail does not allow this arrangement and the small curvature to be given to the wire to make it follow the fold of the origami would make the deformation flexural and no longer axial.

A very compact and effective way of coupling the actuator to the sail is to make it work in torsion. The longer portion of the Z-shaped wire follows the folding line of the pattern, while the two arms lie on the adjacent faces (figure 5.6). This configuration is beneficial for the simplicity of the joint structure and keeps the volume of the system compact. When the wire is heated, it tries to recover the torsional prestrain and the shorter arms push onto the faces and open the angle between them. The amount of recovered torsional strain depends on the length of the crease-aligned wire portion (L) and can induce rotations greater than a full circle [41], ensuring the full deployment of the origami. The torque generated is instead mainly dependent on the radius of the wire, which is a relevant design parameter. A large thickness of the wire generates a greater torque which would allow for easier deployment, whereas the smaller the wire the greater the packing efficiency of the origami.

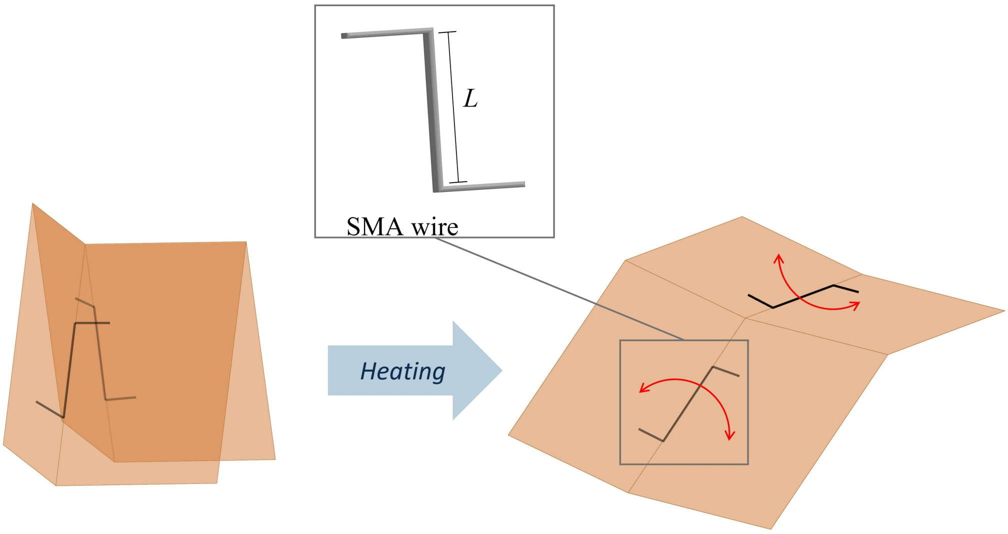

Figure 5.6: Configuration of the shape memory alloy wire actuator.

The design of the actuation system will thus focus on the determination of the smallest possible dimension of the wire capable of deploying the origami. However, the correlation between packing efficiency and torque is not only provided by the dimension of the wire but also by their number and their arrangement along the pattern. First, a higher number of SMA hinges require a smaller radius of each of the actuators with respect to a configuration involving fewer wires. Secondly, the torque is not the same on all the creases, so there exist some configurations requiring smaller wires for the same deployment path (figure 5.7). Chapter 6 will deepen the analysis on the wire configuration.

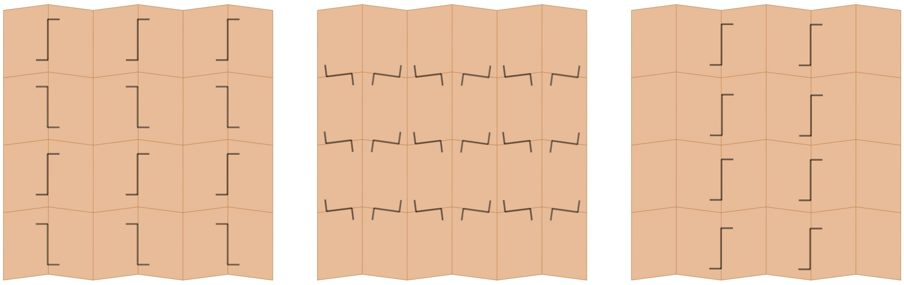

Figure 5.7: SMA wire arrangments along the origami pattern.

In the following section, the constitutive model describing the behavior of the wire will be presented, so as to be able to design its dimensions according to the desired actuation effect. The configuration will be then analyzed by integrating the model into the ADAMS-MATLAB deployment simulation.

5.2.3. Thermal model

The thermal analysis conducted on the SMA wire is analogous to the one provided in Chapter 3 and referred to the sail. Equation 5.1 shows the complete energy balance on the single-node wire modeled according to the lumped parameter approach:

$$\rho V c_V \frac{\partial T}{\partial \tau} = \dot{Q}_{Sun} + \dot{Q}_{ds} + \dot{Q}_{sail,rad} + \dot{Q}_{sail,cond}. \tag{5.1}$$

Since the purpose of these pages is to analyze the actuation phase of the sail, the radiation coming from the Sun $\dot{Q}_{Sun}$ and the one towards deep space $\dot{Q}_{ds}$ are the only sources of heat exchange with the external environment:

$$\dot{Q}_{Sun} = \alpha_w \dot{E}''_{Sun} A_{cross} \tag{5.2}$$

$$\dot{Q}_{ds} = -\varepsilon_w \sigma T^4 A_{ds}. \tag{5.3}$$

This is due to the assumption that, during the deployment, the drag sail is oriented perpendicularly to solar rays, and the SMA wire actuators are located on the surface facing the Sun. In this way, the radiation heating up the wire is the greatest possible. Assuming zero transmission of the sail, the wires are completely shielded from Earth's radiation and the two contributions $\dot{Q}_{alb}$ and $\dot{Q}_{Earth}$ are null. In equation 5.3, A_{cross} and A_{ds} are respectively the cross-section area of the wire radiated by the Sun and the surface radiating towards deep space. Both depend on the deployment angle and change during the actuation phase.

On the other hand, the interaction with the sail gives rise to two contributions, $\dot{Q}_{sail,rad}$ and $\dot{Q}_{sail,cond}$. The first is the amount of radiation received from the surface of the sail:

$$\dot{Q}_{sail,rad} = \dot{Q}_{sail} + \dot{Q}_{relf} \tag{5.4}$$

in which $\dot{Q}_{sail}$ is the heat exchanged with the sail and $\dot{Q}_{refl}$ is the amount of solar radiation reflected from the sail and hitting the wire:

$$\dot{Q}_{sail} = \varepsilon_w \sigma \left(T_s^4 - T_w^4\right) A_w \tag{5.5}$$

$$\dot{Q}_{refl} = \alpha_w \left(1 - \alpha_{sail}\right) \dot{E}''_{Sun} \cos\theta A_w . \tag{5.6}$$

A_w is the surface of the wire exposed to the radiation of the sail. For simplicity, since the wire is fixed on the surface of the sail, it is considered equal to the external surface of the wire multiplied by the self view factor of the sail.

Finally, the heat conduction with the surface of the sail is computed as follows:

$$\dot{Q}_{sail,cond} = h A_{cond} \left(T_s - T_w\right) . \tag{5.7}$$

The surface of the wire in contact with the sail changes with the deployment angle and it is ideally null for the completely deployed configuration since it degenerates in a line. The sail conduction contribution is thus gradually less predominant than that of radiation as the deployment angle decreases.

5.3. Shape memory effect model

Shape memory alloys are very promising in engineering applications, from space to robotics via the medical field. However, their use for the design of intelligent structures and components must pass through an in-depth knowledge of the behavior of these materials as temperature, deformation and stress vary. Many analytical models have been implemented over the years modeling both the microscopic and the macroscopic behavior of the shape memory alloys. Among the several approaches, in this section the focus will be on the model presented separately by Tanaka, Liang, and Brinson [9, 45, 47], a unified constitutive law addressing the constitutive behavior of these materials. Tanaka's model starts considering a one-dimensional SMA material of length L undergoing martensitic transformation. The energy balance equation and the Clausius-Duhem inequality are written as follows:

$$\rho\dot{U} - \sigma L + \frac{\partial q_{sur}}{\partial X} - \rho q = 0 \tag{5.8}$$

$$\rho\dot{S} - \rho\frac{q}{T} + \frac{\partial}{\partial X}\left(\frac{q_{sur}}{T}\right) \geq \ 0 \tag{5.9}$$

where ρ is the density of the current configuration, σ is the Cauchy stress, U is the internal energy density, q_{sur} is the heat flux from the sourroundings, q and T are the internal heat surce and the temperature, and S is the entropy density. According to Tanaka, the thermodynamics of SMA materials is described by the state variables T, ξ, and ε respectively the temperature, the martensitic fraction, and the Green strain (since the deformations involved are large). By introducing the Helmholtz free energy:

$$\Phi_H = U - TS \tag{5.10}$$

the inequality 5.9 can be rewritten, providing the mechanical constitutive equation of the material:

$$\sigma = \rho_0\frac{\partial \Phi_H}{\partial \varepsilon} = \sigma\left(\varepsilon, T, \xi\right). \tag{5.11}$$

From equation 5.11 Liang derived the differential form of the mechanical constitutive model:

$$d\sigma = D\left(\varepsilon, \xi, T\right) d\varepsilon + \Omega\left(\varepsilon, \xi, T\right) d\xi + \Theta\left(\varepsilon, \xi, T\right) dT \tag{5.12}$$

where D is the Young's modulus, Ω is the transformation tensor, and Θ is the thermoelastic tensor. If these three functions can be considered constant over time, the constitutive relation simplifies and becomes:

$$\sigma - \sigma_0 = D\left(\varepsilon - \varepsilon_0\right) + \Omega\left(\xi - \xi_0\right) + \Theta\left(T - T_0\right) \tag{5.13}$$

in which σ_0, ε_0, ξ_0, and T_0 are the initial conditions. This simple equation is able to model the behavior of the SMA during phase transition, but it is valid just for the stress-induced transformation occurring at temperatures above A_f (superelasticity). The reason for this limitation lies in the way ξ is modeled, simply representing the percentage of material in the martensitic state. In order to take into account the shape memory effect, Brinson separated the martensitic fraction into two contributions, based on the micromechanics of the SMA material:

$$\xi = \xi_S + \xi_T. \tag{5.14}$$

In this way, he was able to distinguish between the fraction of martensite obtained from the application of a stress ξ_S and the fraction of purely temperature-induced martensite. As a consequence, the constitutive relation reported in 5.13 can be modified by introducing the two distinct contributions:

$$\sigma - \sigma_0 = D\left(\varepsilon - \varepsilon_0\right) + \Omega_S\left(\xi_S - \xi_{S0}\right) + \Omega_T\left(\xi_T - \xi_{T0}\right) + \Theta\left(T - T_0\right) \tag{5.15}$$

The stress-induced and temperature-induced transformation tensors can be derived from the application of equation 5.15 to specific conditions. In case of maximum residual strain with the material initially 100% austenite, Ω_S becomes:

$$\Omega_S = -\varepsilon_L D \tag{5.16}$$

where ε_L is the maximum recoverable strain, while for maximum residual strain with the material initially 100% undeformed martensite, Ω_T becomes:

$$\Omega_T = 0. \tag{5.17}$$

The final expression of the constitutive model is thus the following (with the subscript "S" of the transformation tensors which can be dropped):

$$\sigma - \sigma_0 = D\left(\varepsilon - \varepsilon_0\right) + \Omega\left(\xi_S - \xi_{S0}\right) + \Theta\left(T - T_0\right). \tag{5.18}$$

However, equation 5.18 derives from the strong assumption of considering the material functions constant, while experimentally the Young's modulus is clearly dependent on the martensitic fraction. A reasonable assumption is the one proposed by Liang and Tanaka, who suggested the following expression of D as a function of the Young's modulus of the SMA as 100% austenite and 100% martensite:

$$D\left(\varepsilon, \xi, T\right) = D\left(\xi\right) = D_A + \xi\left(D_M - D_A\right). \tag{5.19}$$

Therefore, the expression of the transformation tensor (equation 5.16) changes too and turns into:

$$\Omega\left(\xi\right) = -\varepsilon_L D\left(\xi\right) = -\varepsilon_L D_A - \varepsilon_L \xi\left(D_M - D_A\right). \tag{5.20}$$

The constitutive model is not complete until the evolution of the martensite fraction according to temperature and stress is modeled. Liang and Rogers [45] developed an empirically based cosine model representing the trend of ξ along the superelastic phase transformation. The results well agree with the empirical results, but they must be modified to accommodate the correction made by Brinson on the martensitic fraction components (ξ_S and ξ_T). The outcome is thus the transformation equation 5.21, which traces the evolution of the martensitic fraction as the alloy is converted to austenite by temperature change:

$$\xi = \frac{\xi_0}{2}\left\{cos\left[a_A\left(T - A_s - \frac{\sigma}{C_A}\right)\right] + 1\right\} \tag{5.21}$$

$$\xi_S = \xi_{S0} - \frac{\xi_{S0}}{\xi_0}\left(\xi_0 - \xi\right) \tag{5.22}$$

$$\xi_T = \xi_{T0} - \frac{\xi_{T0}}{\xi_0}\left(\xi_0 - \xi\right) \tag{5.23}$$

Each phase transformation has its own associated formulation, but in this framework the focus is on the austenitic one (the shape memory modeling and treatment of the results are analogous to the analyzed case).

This complete model can be adapted to the torsional case too [1]. In this case, the involved quantities are the shear stress τ (equation 5.24) and the shear strain γ, while the Young's modulus gives way to the shear modulus G, as shown in equation 5.25.

$$\tau = \frac{\sigma_{eq}}{\sqrt{3}} \tag{5.24}$$

$$G = \frac{D}{2\left(1 + \mu\right)} \tag{5.25}$$

where μ is the Poisson ratio, which for SMAs is usually equal to 0.3. Equation 5.18 thus becomes:

$$\tau - \tau_0 = G\left(\gamma - \gamma_0\right) + \frac{\Omega}{\sqrt{3}}\left(\xi_S - \xi_{S0}\right) + \frac{\Theta}{\sqrt{3}}\left(T - T_0\right). \tag{5.26}$$

This equation will be widely used for the design of the actuation system since the shape memory actuator will be in the shape of a SMA wire working in torsion.

5.4. Actuator in ADAMS-MATLAB model

Once the analytical description of the shape memory effect is completed, the actuator can be embedded in the ADAMS-MATLAB simulation.

As the temperature rises above A_s and the shape memory actuator starts recovering the pre-stain, the stiffness of the crease line opposes the recovery and a shear stress τ is generated in the SMA wire. The stress results in an actuation torque equal to:

$$T = \tau \frac{J}{r}. \tag{5.27}$$

where r is the radius of the SMA wire while J is the polar moment of inertia ($J = \pi r^4/2$). The actuator is so modeled in ADAMS as a concentrated torque centered along the crease lines on which the actuator lies (figure 5.8).

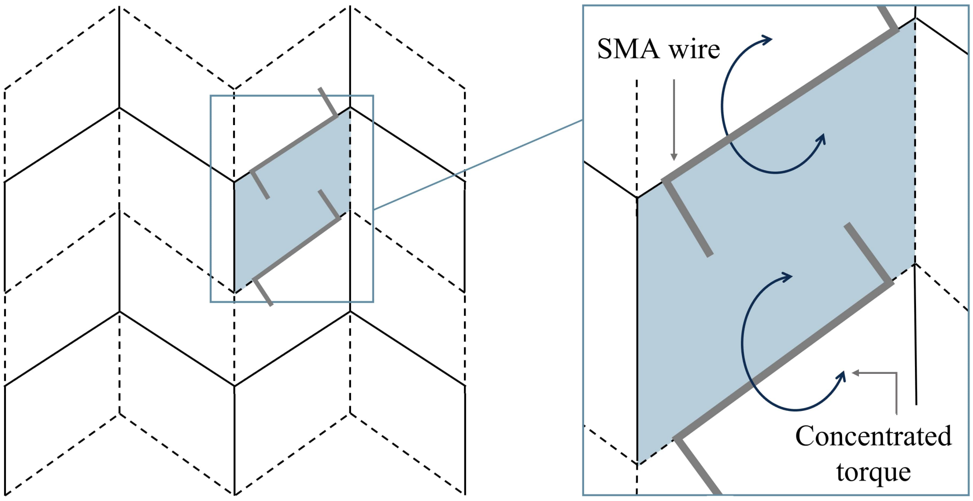

Figure 5.8: Miura-Ori multi-body dynamics simulation: actuator model.

However, the SMA resulting torque is dependent on both the temperature and the crease-equivalent torsional spring stiffness, so it must be ruled by the constitutive equation 5.18 which is tough to model in ADAMS. To overcome this problem, a state variable whose value is associated with the one of the concentrated torque is created with the aid of the MATLAB code interface. The value of the variable is not assigned directly in ADAMS but is taken in input from the constitutive model running in parallel to the multi-body software. (detailed information about ADAMS-MATLAB co-simulation are reported in the following chapter). The modeling of the actuator is therefore limited to the creation of a concentrated force and the variable associated with it.

Another important aspect to consider is the location of the SMA wire along the origami folding lines. As it can be seen in figure 5.9 the amplitude trend of the angles among the faces during the deployment differs with the orientation of the creases.

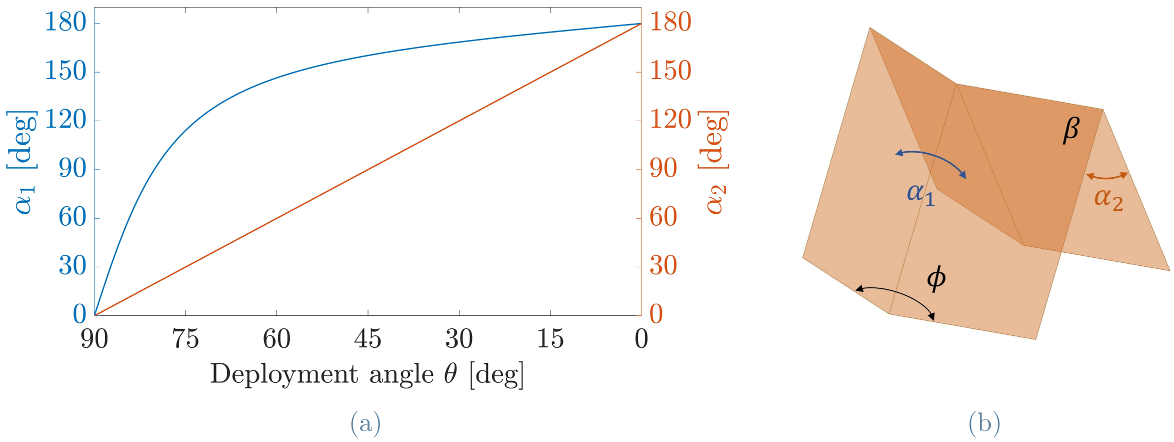

Figure 5.9: α_1 and α_2 trend as the origami unfolds (θ: deployment angle).

The angle indicated with α_1 shows a steep recovery in the first part of the deployment and then a gradual approach to the fully deployed configuration from there on. On the contrary, α_2 rises steadily from 0° to 180°, following an almost linear path. The values of the two angles are computed from the equations below [46, 48]:

$$\cos\phi = \sin^2\beta\cos\theta + \cos^2\beta \tag{5.28}$$

$$\sin\left(\frac{\alpha_1}{2}\right) = \frac{\cos\theta}{\cos\beta\sqrt{1+\cos^2\theta\tan^2\beta}} \tag{5.29}$$

$$\cos\alpha_2 = 1 - 2\cot^2\beta\tan\left(\frac{\phi}{2}\right). \tag{5.30}$$

This large disparity in the recovery trend translates into different strain trends and thus different actuation torques. Therefore, the number of variables associated with the SMA torque value is two, one for the wires mounted along the α_1 creases and the other for the ones along α_2.

Chapter 5 closes the discussion on modeling the sail-actuator system. The complete ADAMS model created with the aid of MATLAB is ready for the simulation of the dynamics of the deployment, which is deeply discussed in Chapter 6.

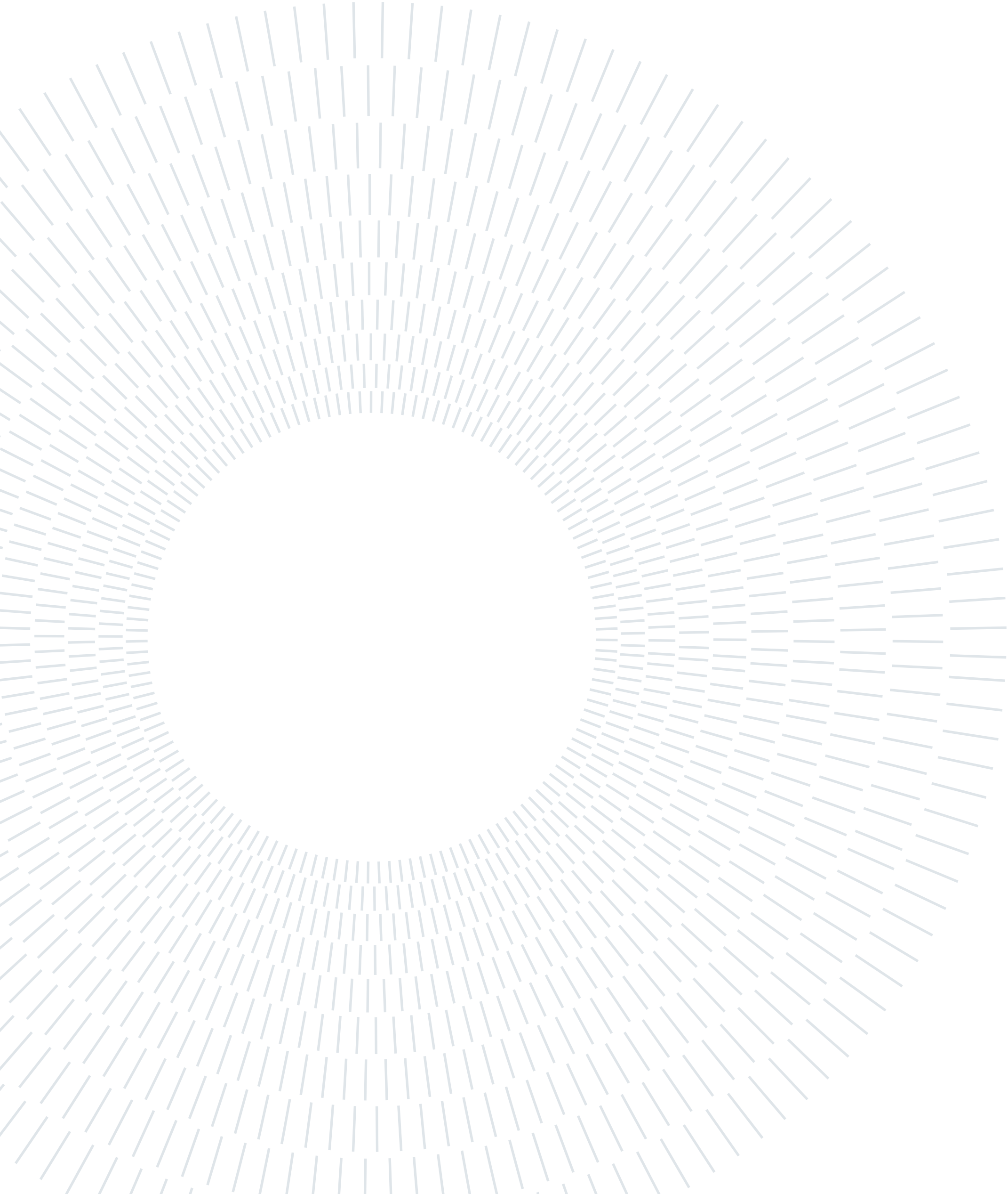

6 | Deployment simulation

The purpose of this chapter is to present the simulation architecture and the results of the multi-body dynamics of the satellite deployment. A brief introduction to the ADAMS-Simulink co-simulation software is followed by a description of the system design and the relative results in terms of deployment and actuator performances.

6.1. ADAMS-Simulink co-simulation

The drag sail-actuator model developed in Chapter 4 and Chapter 5 is now ready to be fed to the ADAMS simulation which is aimed to determine the dimension and configuration of the SMA wires needed to deploy the sail. As stated in Chapter 5, the main issue is related to the implementation of the torque in ADAMS since it depends on temperature and strain conditions. In fact, ADAMS provides the possibility to define a runtime function representing the behavior of the concentrated torque over time, but the internal stress from which the force derives is implicit in the constitutive model and the dependence on the temperature is a source of additional complication. The torque is thus assigned a variable whose value must be calculated in parallel to the simulation and supplied to ADAMS at each time step (Chapter 5.4). This is made possible through co-simulation between ADAMS and Simulink, a MATLAB-based programming software whose implementation is briefly described in the following lines.

Once the Miura-Ori model is completed and the torque variables are set, the *Adams Control Plant Export* tool generates a MATLAB-equivalent dynamic model of the sail to be imported in Simulink. The block created contains the dynamic characteristics of the model and consists of a set of input and output ports. The first set allows supplying the dynamic model with the module of the actuator-equivalent force at each time step. Hence the possibility of assigning Simulink the task of externally calculating the torque generated by the wire. The second set of ports instead provides output information about the dynamics of the multi-body model. In addition to analyzing the behavior of the drag sail, these are also useful whether the output data influences the input ones, as in this case. In fact, the action of the actuator depends on the temperature and the torsion of the wire, which in turn vary according to the angle at which the sail is deployed. The output parameter of the block is the length of a single cell w along X direction, represented in figure 6.1. This parameter provides information about the unfolding status and can be used to compute the deployment angle θ, which is the main input for the computation of temperature and torque:

$$\theta = \frac{\pi}{2} - \frac{1}{2}\arccos\left(1 - \frac{2\tan^2\frac{\phi}{2}}{\tan^2\beta}\right); \tag{6.1}$$

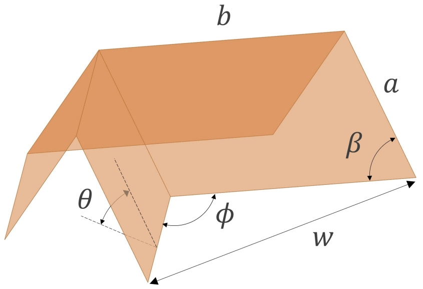

Figure 6.1: Miura-Ori cell geometry.

Figure 6.2 shows the complete Simulink scheme of the co-simulation, in which the orange block is the MATLAB-equivalent dynamic model of the drag sail. The red block is aimed at computing the deployment angle from equation 6.1, while the yellow and the blue ones are respectively dedicated to the evaluation of the temperature and the torque.

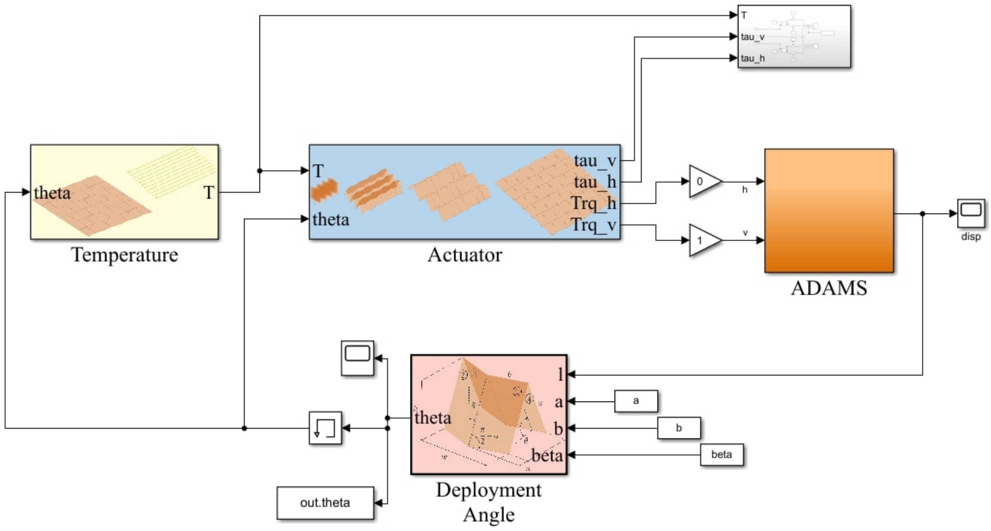
T
tau_v
tau_h
theta
T
Temperature
T
theta
tau_v
tau_h
Trq_h
Trq_v
Actuator
0
h
1
v
ADAMS
disp
l
a
b
beta
theta
Deployment Angle
a
b
beta
out.theta

Figure 6.2: Simulink simulation scheme.

The integration of the drag sail dynamics is dictated by Simulink, meaning that it leads ADAMS in the computational order. As a consequence, it is possible to set the integration parameters and the communication interval with ADAMS directly in Simulink.

The first parameter to be set is the integration stop time, which depends on the dynamics of the origami. In fact, a complete integration should terminate upon complete deployment, but the timespan changes based on both the geometry of the sail and the characteristics of the actuator. A stop time of about 60s indicatively guarantees successful deployment (see the following paragraphs).

Secondly, the integrator can be chosen from a variety of ODE solvers embedded in MATLAB. The one suggested for the co-simulation with ADAMS is the *ode113* function, a variable order integration method for nonstiff differential equations capable of high accuracy and suitable when using stringent error tolerances or solving computationally intensive ODE files. The solver step is set as 'variable', with an automatic maximum step size and a relative tolerance of 1e-3. Better accuracy can be reached by lowering both the tolerance and the stepsize, with a consequent increase in the computational cost.

6.2. Actuator configuration influence on deployment

The first step in designing the actuation system is to understand which wire configuration could be the most advantageous in the deployment. The most relevant requirements to be met are the complete deployment of the sail and a maximum packed volume of 1U. These two are in contrast with each other, as the higher the number of wires the simpler the deployment, whereas the lower the number the lower the volume occupied by the packed origami. The total volume occupied by the SMA actuators would be low since the diameter of the wire is some tens of micrometers while the length is a couple of centimeters. However, the way the origami is folded forces the wires to stay one aside from the other, increasing the packed dimension (figure 6.3).

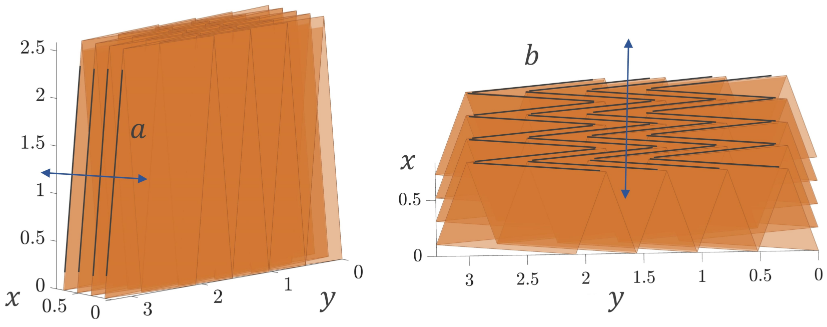

Figure 6.3: Influence of the position of the SMA wires on the packed dimension. The dark lines represent the SMA wire actuators lying along the a and b sides of the cells.

As it can be noted from figure 6.3, the disposition of the wires along a or b creases is way different in terms of overall dimension. On the one hand, when the SMA lies along a it overlaps just with the wires of the same row of cells in the X direction. On the contrary, when placing the actuator along the b sides, the thickness of the origami increases a lot due to the fact that the wires aligned with each other are not only those along the same row of cells in the X direction, but also those along the same row in Y direction. This issue limits a lot the potential thickness of the wire actuator along b as the width of the packed configuration risks not fitting inside the satellite. A possible solution aimed at reducing the dimension of the entire system is to place the wires in such a way as to minimize the overlap. This is achievable by reducing the length of the b wire to an amount equal to the shift between two consecutive vertices of the origami (figure 6.4), computed as:

$$\text{shift} = 2a\cos\beta. \tag{6.2}$$

In this way, the wires lying on the same row in the Y direction do not overlap anymore and the width of the geometry is drastically reduced.

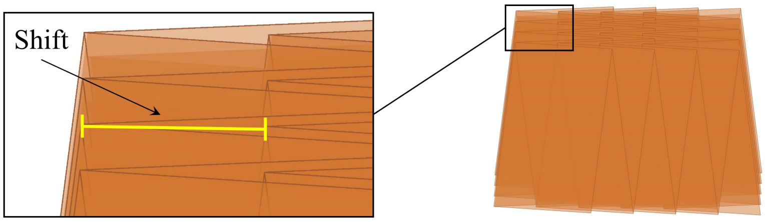

Figure 6.4: Shift distance between two consecutive vertices of the Miura-Ori.

However, this solution is unsuitable because it contrasts with the requirements on both the sail's dimension and the actuator's force. To optimize the relationship between packed volume and the deployed surface of the drag sail, in fact, the length of the two sides of the origami cells must be limited to a couple of centimeters, and the value of β must be close to 90°. According to equation 6.2, these requirements make the shift size very short, and so does the wire length. Since the length of the actuator is strictly related to the maximum recoverable angle, a shorter wire would not guarantee the complete deployment of the sail and the actuator would be ineffective.

Because of the issues deriving from the placement of the actuators on b, the following design is based on the configuration with the SMA wires along the a creases only. This design strategy is a simplification in the choice of the wires' pattern since it is based just on geometrical considerations and neglects any analysis of the optimization of the overall deploying force. Future developments will require a more in-depth analysis of this aspect.

6.3. Deployment design

Once the actuators' configuration along the sail's creases has been analyzed and selected, the design moves towards determining the wire size necessary to unfold the origami fully. The objective is to verify if, for certain fixed mechanical properties of Nitinol, there is the possibility of realizing an actuator compatible with drag sails both from the point of view of forces and dimensions. The following sections focus on the dimensions optimization of the SMA wire, considering a 2x2 cells portion of the overall origami sail. The dependency on the maximum recoverable strain is also considered in the unfolding phase analysis to limit the actuator's internal stress and minimize the final residual strain.

6.3.1. Deployment dependency on SMA length, radius and strain

In the previous paragraph, it was pointed out that the diameter of the Nitinol wire significantly influences the volume occupied by the packed sail. Conversely, the length of the wire does not affect the size of the subsystem inside the satellite, provided that it must not exceed the length of the crease on which it lies. However, both actuator dimensions contribute to the maximum torque exerted by the wire on the system and are thus essential in the determination of the deployment performance.

Likewise, the maximum prestrain the SMA can recover changes the size requirements on the wires: a prestrain in the order of 3% requires greater length in order to recover the same unfolding angle as a wire with a 6% prestrain. This mutual dependence is evident from equation 6.3, in which the relationship between strain and rotation angle is reported:

$$\Delta\alpha = \frac{l_w}{r_w}\gamma \tag{6.3}$$

Considering the above, it seems appropriate to state that a length close to the maximum allowed by the geometry of the origami plus a prestrain equal to the maximum allowed by the material guarantees the greatest recoverable angle and, therefore, good unfolding performance by limiting the dimensions of the wire. However, the problem with this approach lies in the fact that the entity of the torsional stress generated inside the wire needs to be considered. Equation 6.4 explains this point well: assuming that the actuation torque T necessary for deployment is fixed, if the radius of the wire decreases the internal torsional effort τ must increase to guarantee the same force.

$$T = \frac{\pi r_w^3}{2}\tau \tag{6.4}$$

The example presented in figure 6.5 and table 6.1 shows the trend of torque and stress in the complete deployment of the drag sail as the prestrain of the SMA wire varies. The results refer to a condition where the wire length is fixed to a value close to the length of the a side on which it lies, with the aim of minimizing the wire diameter. As the prestrain increases in modulus, the wire diameter required to unfold the sail decreases to a value below 100 microns. If, on the one hand, the final driving torque remains the same, on the other hand, it can be seen that the temperature at the end of the martensitic transformation of Nitinol increases considerably, and consequently, the internal stress of the wire too.

Fixed wire length: $l_w = 2.35$cm	
Recoverable strain ε_L [-]	Radius of the wire r_w [μm]
0.025	158
0.030	130
0.035	115
0.040	105
0.045	100
0.050	96

Table 6.1: Radius dimension as the prestrain varies (fixed wire length).

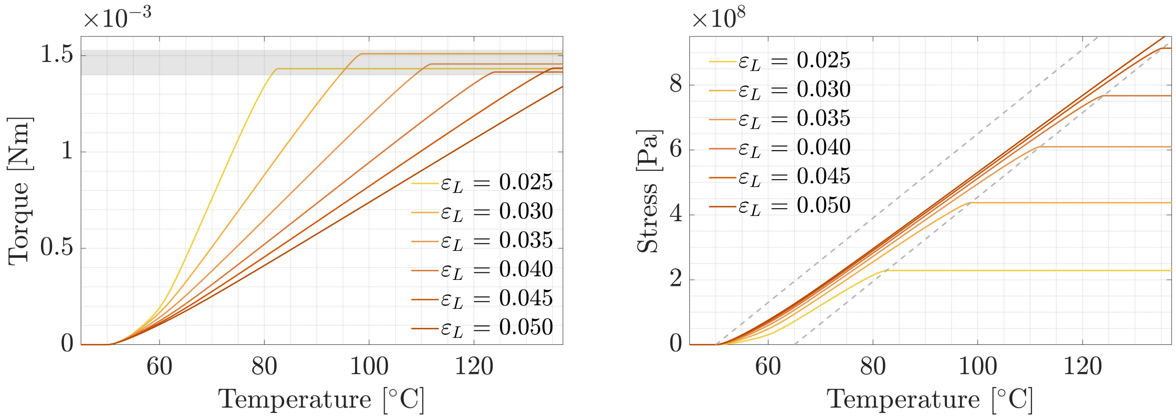

(a) (b)

Figure 6.5: Torque and stress trend for different values of initial prestrain. The results are obtained for a 2.35cm fixed length of the wire.

The reason for such a variation in the internal stress of the wire is given by the amount of residual prestrain at the end of the martensitic transformation. Figure 6.6 shows how for high prestrain values, the actuator's force is insufficient to fully recover it, with consequent residual strains close to the initial ones and the onset of high internal stresses. This situation for high strains turns out to be similar to that of the completely restrained recovery condition, in which the prestrain recovery is prevented.

Figure 6.7 shows the drag sail deployment angle trend in time, highlighting the variation in the time needed to fully open the sail as the radius and the prestrain vary.

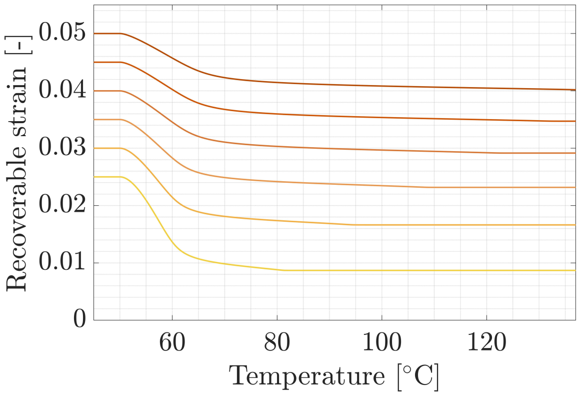

Figure 6.6: Strain recovery trend during sail deployment for different initial prestrains.

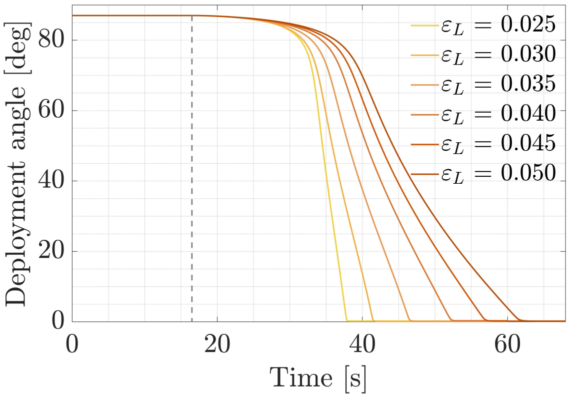

Figure 6.7: Deployment time as a function of different prestrain and wire radius.

Therefore, this design strategy does not guarantee the structural integrity of the Nitinol wire, so the mutual contribution of the variation of r_w, l_w, and γ_L must be taken into account. In particular, the goal is to understand which are the minimum values of l_w and γ_L that guarantee the complete deployment of the sail and, at the same time, the radius of the wire which guarantees the necessary force, without exceeding the plastic deformation limit of Nitinol.

The following section focuses on the constraint optimization design of the actuator, providing the solution whose results are presented at the end of the current chapter.

6.3.2. Optimization algorithm

The analysis made in the previous paragraph makes it clear that the choice of the actuator features cannot be based only on the size of the de-orbiting subsystem because of the bad performance in terms of maximum internal stress. The strategy adopted below is therefore based on maximizing the recovery of the initial prestrain, which in turn guarantees lower stress in the Nitinol wire at the end of the martensitic transformation.

As stated before, the l_w-γ_L couple defines the maximum angle α_R that the wire can recover during deployment. Low values of l_w and γ_L, even if associated with very large radii, provide low α_R, hence only partial recoveries of the packed origami shape. Therefore, by fixing a certain initial prestrain, there will exist a minimum value of l_w such as to guarantee a suitable recoverable angle and a corresponding r_w generating a torque capable of counteracting the resistance opposed by the sail until the maximum deployment. Figure 6.8 helps explain this concept showing the actuator-induced deployment of the sail for two different scenarios: in figure 6.8a the length of the wire is fixed to 1.70cm, while in figure 6.8a to 2.30cm. The initial prestrain is set to $\gamma_L = 0.025$.

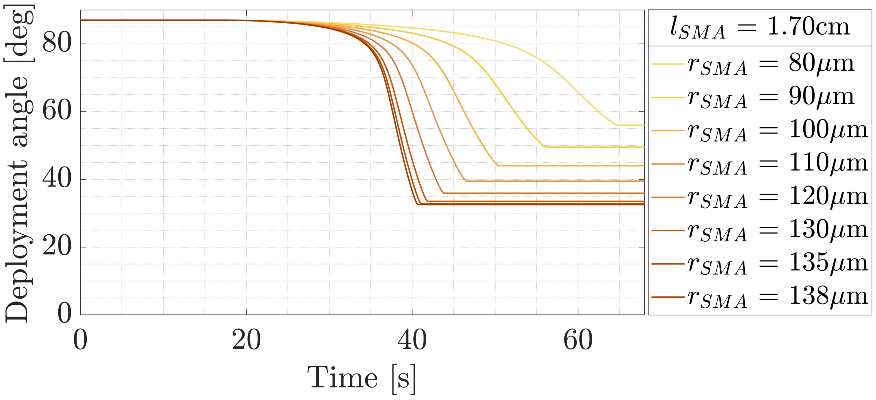

(a)

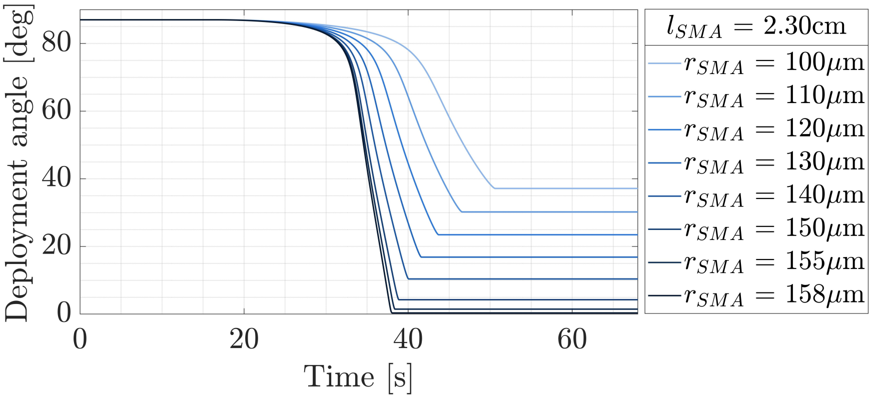

(b)

Figure 6.8: Drag sail deployment for different values of l_w and r_w. $\gamma_L = 0.025$.

By observing the first figure, it can be noted that large actuator's diameters produce greater torque hence the final angle at which the sail deploys decreases. As the radius increases, however, the rate of decrease in the deployment angle also reduces until it reaches the lowest possible limit. This limit corresponds to the maximum angle the actuator can recover using a wire with those specific characteristics in length and prestrain. For a Nitinol wire having an initial prestrain of 0.025 and a length of 1.70cm, the limit packing angle is about 35°, beyond which it is not possible to induce further opening (figure 6.8a). Since a 1.70cm wire does not guarantee full sail deployment for a 2.5% prestrain, there will exist a value of l_w such that, by increasing the radius size, the final angle will converge to 0°, i.e. to the fully deployed configuration (figure 6.8b).

The above represents a good solution for sizing the Nitinol wire as an actuator for the sail. An optimization algorithm is thus implemented and it sets out to find, given a specific prestrain value, the pair of l_{opt} and r_{opt} such as to deploy the sail while minimizing the strain at the end of the deployment. The cost function to be minimized is the deployment angle, which is constrained to be greater than zero. The driving parameters are l_w and r_w, while the recoverable strain is fixed for simplicity.

The main issue coming from the implementation of the optimization algorithm is the prone-to-failure attitude of the dynamic simulation when it approaches the complete deployment. The configuration with $\theta = 0°$ is in fact an inversion point for ADAMS, causing the code to fail and the simulation to stop. The consequence is the impossibility of completing the optimization whenever the dynamic simulation tries to converge to the minimum of the cost function ($\theta_{fin} = 0°$) with a length and radius of the wire greater than the minimum necessary to deploy the sail (l_{opt}, r_{opt}). To solve the problem, the algorithm should be able to converge to $\theta_{fin} = 0°$ from below, i.e. gradually increasing l_w and r_w, and stop at the first simulation encountering the inversion point. This is made possible by the built-in MATLAB function *try*, which allows running the simulation and continuing the optimization even if it fails due to exceeding the inversion point.

The optimization algorithm is thus implemented in MATLAB and the workflow can be seen more in detail in the pseudocode reported in Algorithm 6.1. It begins by setting the guess radius and length and their corresponding iteration step values. Two tolerances are then imposed. The first, tol_θ, refers to the tolerance on the solution of the optimization: the most external *while* cycle runs until the final angle is less than tol_θ, so the more the tolerance is close to zero the more the solution is accurate. The second is instead the one establishing the convergence of the deployment angle to the minimum value ensured by the couple r_w-l_w (greater than zero, see figure 6.8a). When the difference between two consecutive θ_{fin} is less than tol_r it means that the solution has reached convergence and the next iteration cycle can be initiated by increasing the value of l_w.

As the algorithm approaches the optimization target ($\theta_{fin} = 0°$) the iteration stops and the θ_{min} is obtained. The accuracy of the solution can be improved by tuning the tolerances and the iteration steps, with a consequent increase in the computational cost. Table 6.2 reports the results regarding optimal l_w and r_w for different initial prestrains, all of them ensuring the complete deployment of the origami.

Algorithm 6.1 Minimization of the deployment angle

```
Specify the initial guesses: $r_{guess}$, $l_{guess}$;
Specify $r_w$, $l_w$ iteration step: $step_r$, $step_l$;
Specify the tolerances: $tol_\theta$, $tol_r$;
$r_w = r_{guess}, \quad l_w = l_{guess};$
while $\theta_{fin} > tol_\theta$ do
    while $\theta_{fin}^{old} - \theta_{fin}^{new} > tol_r$ do
        try Run ADAMS-Simulink co-simulation $\rightarrow \theta_{fin}$;
        if not error then
            $r_w = r_w + step_r$;
        else
            EXIT from the loop;
        end if
    end while
    $l_w = l_w + step_l$;
end while
$\theta_{min} = \theta_{fin}$
$r_{opt} = r_w, \quad l_{opt} = l_w$
```

Optimization results:		
Recoverable strain ε_L	Length of the wire l_w	Radius of the wire
[-]	[cm]	[μm]
0.025	2.35	158
0.030	1.82	149
0.035	1.48	142
0.040	1.24	136
0.045	1.06	130
0.050	0.92	126

Table 6.2: Optimim radius and length dimension for different prestrain values.

It is evident how the length of the wire decreases as the prestrain increases, while the variation in the size of the radius is much less marked than in the previous case (table 6.1). This result was expected since, as the prestrain increases, the length of the wire required to fully deploy the sail is reduced. Consequently, the decrease in the length limits the reduction in the radius value, since a thicker wire is needed to recover the initial prestrain down to the deployed configuration.

It is worth noticing that the solutions obtained by the optimization algorithm for different prestrains all have almost the same value of the free recoverable angle, i.e. the angle the wire would recover through martensitic transformation if not partially restrained by the sail structure, computed with the above formula in equation 6.3 (figure 6.9). This angle is greater than the one the wire must recover (180°, a bit less if considering a partially opened initial configuration of the sail) since the SMA wire partially returns to the initial shape and partially generates internal torsional stress due to the unfolding resistance opposed by the creases stiffness.

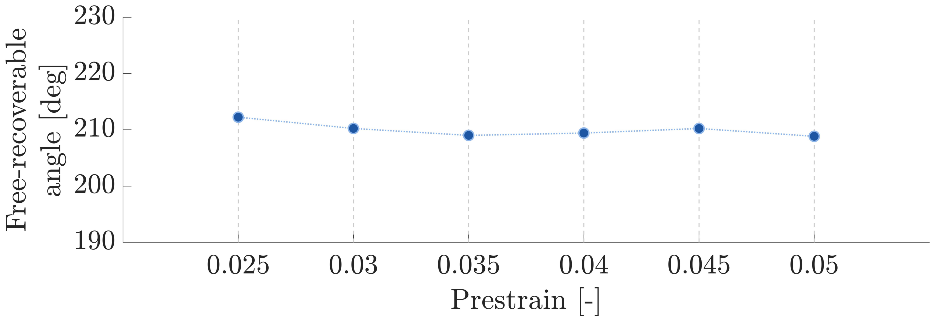

Figure 6.9: Free-recover angle for different optimization results.

Figures 6.10a and 6.10b instead show the torque and the stress related to the optimal solutions. As in figure 6.5a, the torque needed to deploy the sail is stationed just below 1.5m, a value common to all curves. Compared to the solution in figure 6.5b, the temperatures at the end of the transformation are much lower and, consequently, so are the maximum stress values reached at the end of the deployment. This is due to the fact that the radius of the wire is bigger than in the previous case and the initial prestrain is recovered to a greater extent, as shown in figure 6.11. In fact, contrary to what happens in the trends associated with the fixed-l_w strategy, even the higher initial prestrain is recovered down to a value of about 1.5%.

Finally, figure 6.12 shows the deployment path of the origami over time. The unfolding phase lasts about 25s, elapsing from the martensite start temperature to the end of the martensitic transformation. Unlike the previous case, the lines are close to each other, showing a variation in the deployment time not greater than ten seconds.

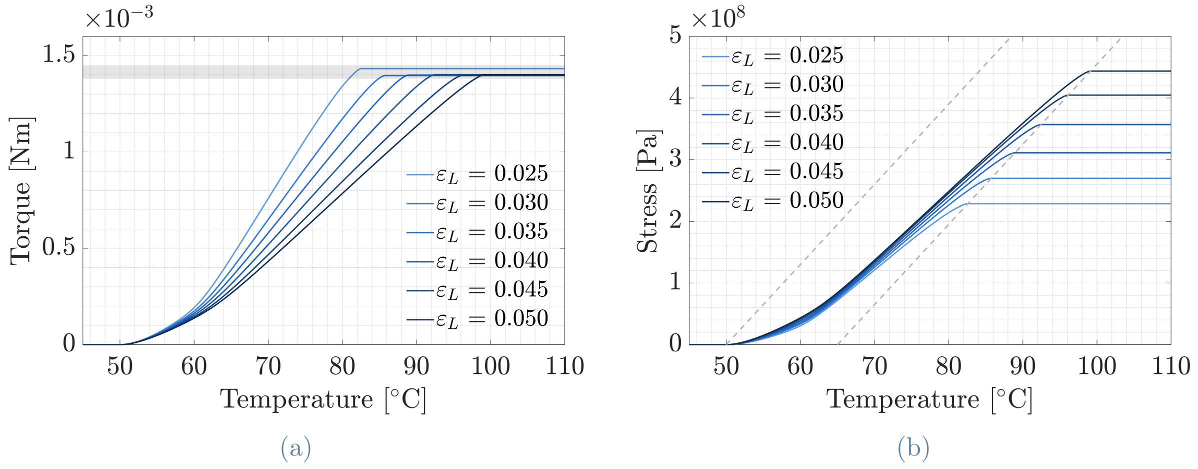

Figure 6.10: Torque and stress trend for different values of initial prestrain.

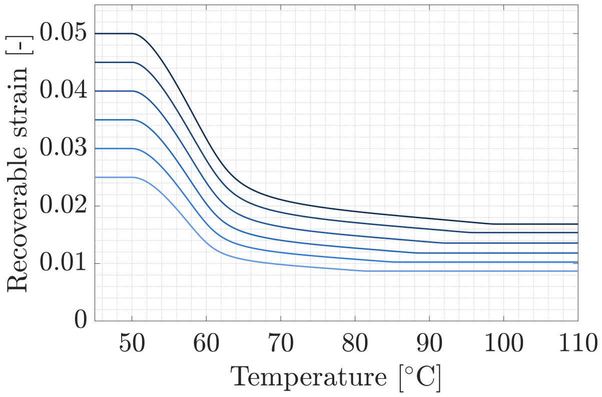

Figure 6.11: Strain recovery trend during sail deployment for different initial prestrains.

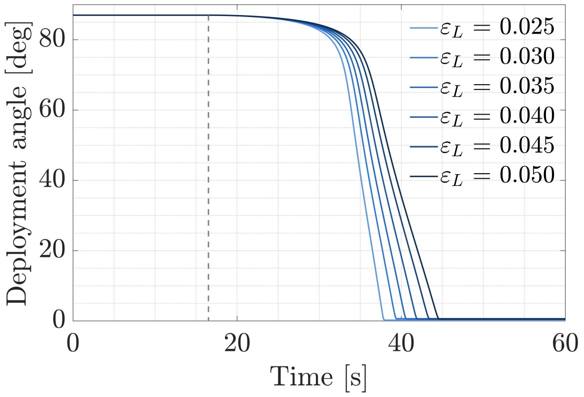

Figure 6.12: Deployment time of different optimal solutions.

The ADAMS-Simulink co-simulation combined with the optimization algorithm allows to design the sail's deployment system and verify the solution's feasibility.

6.4. Simulation of the optimum geometry: results

The current section reports the design results of the actuation of the drag sail deployment. The geometry of the sail is taken from the de-orbit analysis carried out in Chapter 2 with the aid of the origami optimization algorithm (table 2.5). The configuration of the actuators is instead the one defined in the previous paragraphs, with the SMA wires lying along the fold lines a. Finally, the wire material considered is a typical mid-temperature range Nitinol alloy, whose properties are collected in the table below [9, 15, 19, 51].

SMA wire actuator properties	
Density	6450kg/m^3
Young's modulus (Martensite)	30GPa
Young's modulus (Austenite)	72GPa
Poisson's ratio	0.33
Austenite start temperature	50°C
Austenite finish temperature	65°C
Maximum residual strain	0.025

Table 6.3: SMA properties. The values refer to a typical mid-temperature range Nitinol.

Given the design choices above, the Nitinol wire dimensions needed to deploy a 2x2 cells origami sail is $l_w = 2.35cm$ and $r_w = 158.6\mu m$, obtained from the optimization algorithm in section 6.3.2. The result is the one shown in figure 6.13, in which the trend of deployment angle and wire's temperature are reported together.

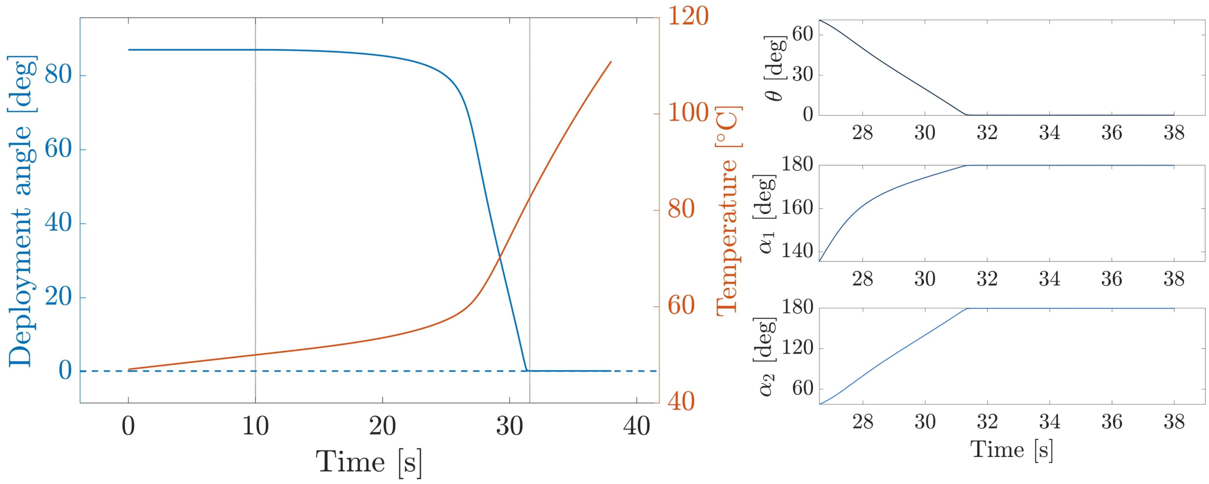

Figure 6.13: Deployment of the drag sail due to the action of the SMA wires. The decrease of the deployment angle θ as the temperature rises above A_s is evident from the graphs.

As the satellite's mission comes to an end, the sail is released from within the satellite and it begins to be exposed to solar radiation. The temperatures of the sail and the actuators gradually rise up to the point when the SMA wire reaches the transformation temperature A_s. Beyond this value, the actuator starts recovering the initial prestrain and θ gradually decreases. As the sail deploys, the cross-sectional area exposed to the radiation increases and so does the temperature. This phenomenon proceeds until θ reaches the value of 0°, corresponding to a complete deployment of the de-orbit system.
The total elapsed time from A_S temperature to the end of the martensitic transformation is about 21s. In this period, α_1 and α_2 increase from a starting angle of 0° to 180° (subfigures 6.13), corresponding to a SMA wire strain recovery from 2.5% to 0.8%.

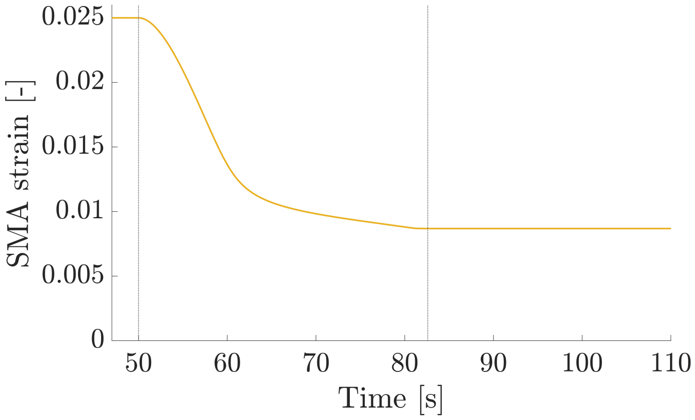

Figure 6.14: Strain recovery during deployment.

Figure 6.15 shows the stress and torque trends as a function of the temperature. As the martensitic transformation begins, the SMA contrasts the resistance opposed by the origami and a torque arises, which keeps increasing up to the end of the transformation.

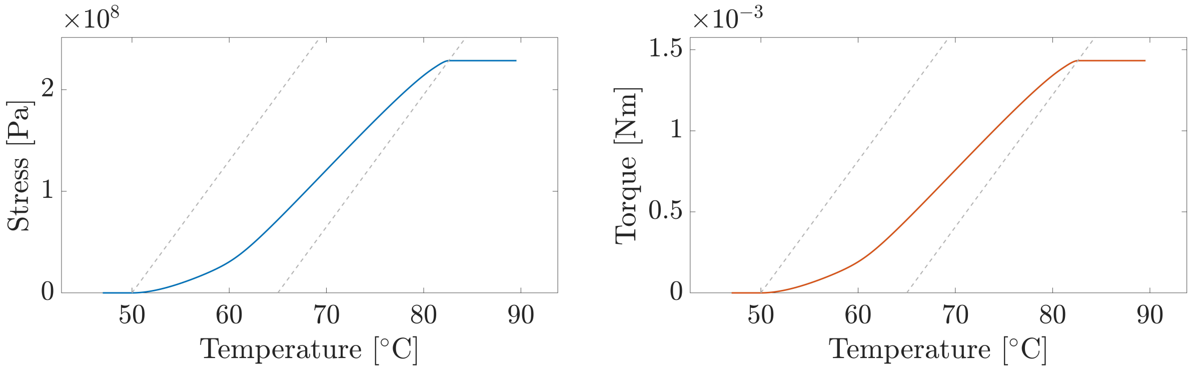

(a)

(b)

Figure 6.15: Stress and torque trends as a function of temperature during the deployment.

The simulation is limited in the number of cells that can be imported in ADAMS View Student Edition. Despite that, the possibility to access the complete version of the software allows for validating the results even for larger sail sizes. Figure 6.16 shows the trend of the deployment angle over time as the dimension of the sail varies. By fixing the dimension of the SMA wires, it can be noted that the final deployment angle does not scale as the number of cells, but it just grows slightly as the number of cells increases.

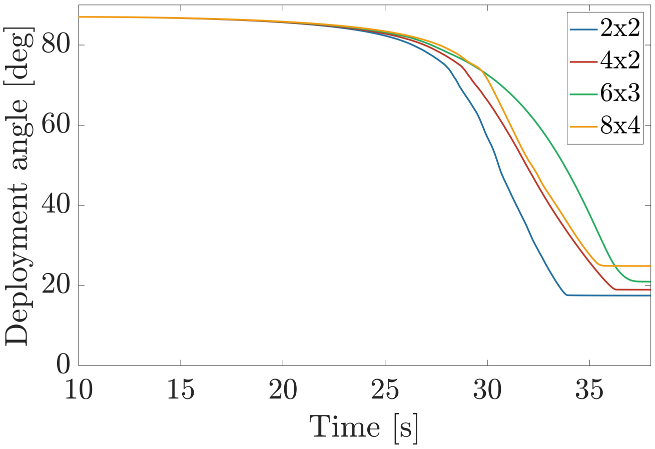

Figure 6.16: Deployment trend for different dimensions of the origami sail ($N_x \times N_y$). The results are obtained by simulating the structures with fixed SMA actuator characteristics: $r_w = 140\mu m$, $l_w = 2.1mm$, $\gamma_L = 0.025$.

This effect is predictable by thinking about the way the actuation system is designed. If, on the one hand, the larger the origami the higher the number of creases and thus the higher the rigidity of the system, on the other hand, as the number of wires increases the overall torque increases as well. The only two parameters scaling with the dimension are the inertia of the sail and the ratio between the number of SMA wires and the total number of creases in the pattern. As regards the first, its contribution is almost negligible with respect to the rigidity of the creases (overall mass of the 20x11 sail: less than 20g), providing a minimal increase of the required deploying torque. Regarding the second aspect, it is evident from figure 6.17 that the ratio between the number of wires and creases N_w/N_{crease} (considering the wire's arrangement described in the previous lines) reduces as the number of cells increases, reaching a plateau. Moreover, highly uneven geometries (large difference between the number of cells along X and Y) show high values of N_w/N_{crease}. A higher ratio guarantees a more effective action of the actuator on the structure, resulting in an easier deployment of the smaller patterns. However, the difference in the ratio among the various configurations is minimal, therefore also the one in the deployment results.

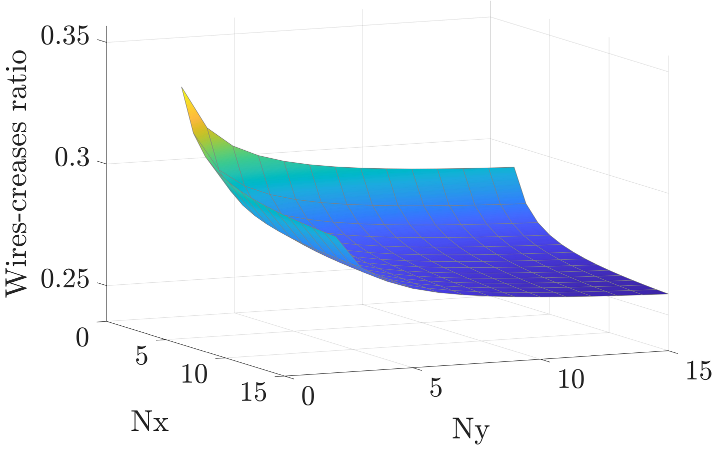

Figure 6.17: Ratio between the number of wires and creases.

The almost simultaneous increase in stiffness and torque makes the design easily scalable for structures of different sizes. Future developments could deepen this aspect by carrying out the optimization analysis also for the complete geometry, finding the optimum characteristics of the actuator and providing more accurate insight into its behavior. Although there is no information regarding the optimization of the full sail deployment system, it is still possible to deduce the dimensions and mass characteristics of the complete subsystem. The following results refer to a set of actuators having $r_w = 200\mu m$, $l_w = 2.5mm$. Since the number of cells in the origami sail is 20x11, each of them having 4 faces, the total number of wires settles at 440, with an overall mass of the deployment system of about 2g only (∼4.5mg each). As regards the width of the packed geometry, the embedment of the SMA wires makes it grow from the 4.8mm value of the sole origami sail to about 13mm. The increment in the dimension is not consistent and it is perfectly compatible with the space available in a 1U CubeSat.

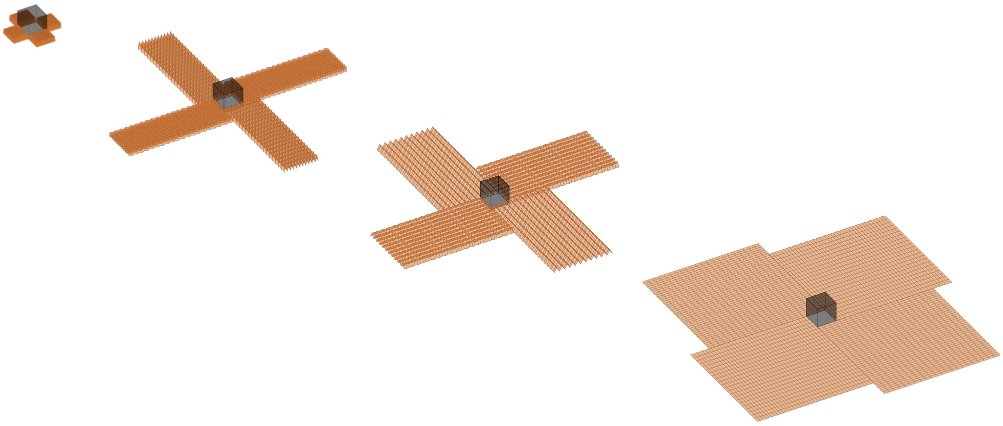

Figure 6.18: Deployment sequence of the origami drag sail.

6.5. Uncertainty propagation

During the production phase of the Nitinol wire and the subsequent manufacturing process to adapt it to use as an actuator, the dimensions are affected by uncertainties that can affect the deployment performance. In fact, different values of L and R change the recoverable strain and the internal stress of the wire and, consequently, the torque acting on the structure. It is thus important to understand how even small variations in the nominal size of the wire impact the overall performance of the system.

The analysis regards the propagation of the uncertainties on the size of the wires selected for the deployment of the drag sail. To do this, a population of wires having a standard deviation of 1% on the length and radius is considered. As the actuation torque produced by the wire is a function of these two quantities, the uncertainty will propagate to the driving torque, altering the deployment performance. By combining equations 5.26 and 5.27, it is possible to write the constitutive law as a function of the three parameters T_w, r_w, and l_w:

$$f\left(T_w,\ r_w,\ l_w\right) = 0. \tag{6.5}$$

As a consequence, the variance on the torque is computed as:

$$\sigma_{T_w}^2 = \left(\frac{\partial T_w}{\partial r_w}\right)^2 \sigma_{r_w}^2 + \left(\frac{\partial T_w}{\partial l_w}\right)^2 \sigma_{l_w}^2 \tag{6.6}$$

with $\dfrac{\partial T_w}{\partial r_w}$ and $\dfrac{\partial T_w}{\partial l_w}$ evaluated for a specific solution of equation 6.5. Since the function $f\left(T_w,\ r_w,\ l_w\right)$ is implicit in T_w, the partial derivatives are computed according to the implicit differentiation theorem as follows:

$$\frac{\partial T_w}{\partial r_w} = -\frac{\dfrac{\partial f}{\partial r_w}}{\dfrac{\partial f}{\partial T_w}} \quad ; \quad \frac{\partial T_w}{\partial l_w} = -\frac{\dfrac{\partial f}{\partial l_w}}{\dfrac{\partial f}{\partial T_w}}. \tag{6.7}$$

The computation of the derivatives $\dfrac{\partial f}{\partial T_w}, \dfrac{\partial f}{\partial r_w}, \dfrac{\partial f}{\partial l_w}$ is carried out directly in MATLAB using the symbolic toolbox embedded in the software.

The solutions are reported in figure 6.19, showing torque and deployment trends as a function of time. It can be seen how the standard deviation (represented by the grey areas) is strictly confined around the curves, with a value of about 3% of the mean one for the Torque. The consequence of this small variation in the actuation force is the alteration in the final deployment angle of the drag sail, as shown in figure 6.19b. These information are relevant in the design of the actuator since considering the nominal only could lead to suboptimal system operation.

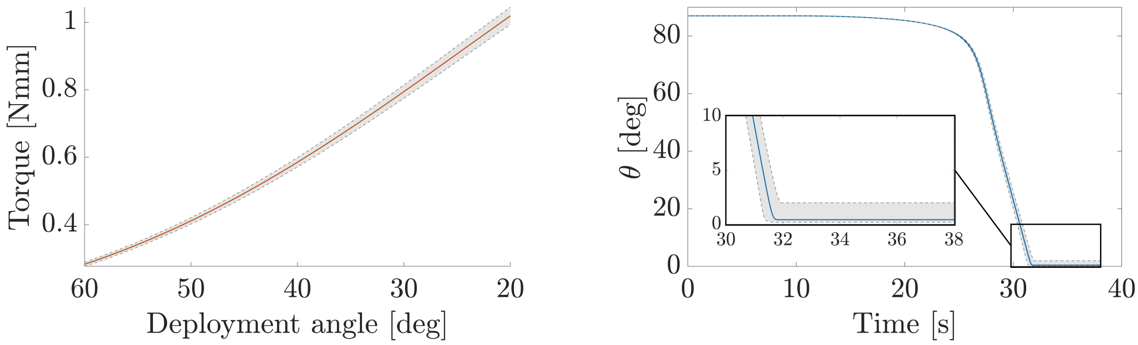

(a)

(b)

Figure 6.19: Uncertainty propagation on the torque generated by the wire during the deployment. The gray regions represent the 3% uncertainty in the magnitude of the torque and the consequent variation in the deployment performances. The graphs are obtained by simulating the deployment of the drag sail with $r_w = 158\mu$m and $l_w = 2.35$cm.

7 | Conclusions and future developments

The aim of the thesis was to analyze the dynamics of the passive deployment of an origami drag sail. For this purpose, it was chosen to use SMA wires as passive actuators integrated into the origami structure capable of bringing the sail into the operational configuration by exploiting the one-way shape memory effect. The arrangement of these wires has been designed to reduce the size of the overall system and, at the same time, guarantee a uniform deployment of the sail.

The study's results show the system's effectiveness from many points of view. First, the choice of origami pattern ensures excellent packing efficiency. In fact, the overall volume of the sail alone does not exceed 6% of the space available within a single 1U unit while guaranteeing a large drag surface.
As designed, the actuator appears perfectly capable of deploying the sail at the end of the spacecraft's life cycle. The Nitinol wires recover the initial pre-deformation by exerting a torque along the fold lines, which results in a recovery of the drag sail's operational configuration. By acting directly on the origami creases, no deformations are localized along the folding lines due to the resistance opposed to the opening and the sail is uniform in its final shape. Furthermore, unlike passive systems based on the recovery of elastic energy, the deployment is not abrupt and immediate but gradual from the beginning to the end of the martensitic transformation. This fact reduces the risk of localized stress and, consequently, of sail breakage. Regarding the overall system's size, the diameter and length of the small Nitinol actuators do not significantly impact the volume occupied. Although, in fact, the increase in the volume of the sail alone is inevitable, the encumbrance and mass are much lower than in traditional deployment systems.

The work carried out is part of a larger project on deployable origami structures already inherited from the previous thesis student. The results obtained open new paths toward the further future development of this research field.

The first way forward is to analyze the dynamics of unfolding by considering the origami faces as flexible. Gossamer structures are generally very thin and the low flexural stiffness predisposes them to bend during deployment. The use of finite element software would allow considering this aspect, to be coupled with a more in-depth model of the behavior of the folds. In these pages, in fact, the stiffness of the origami folds is considered constant, whereas in the case of Kapton and polymers in general, the temperature affects the force opposed by the structure to unfolding. The analysis carried out on the previous pages is thus oversized compared to what is expected, potentially making the properties of this system even better.

Another line of interest is the structural analysis after the operational configuration has been reached. In this case, the shape must be maintained without the sail crumpling or folding back on itself. Two paths could be analyzed. Firstly, the stiffness of the unfolded sail could be evaluated to assess the need to adopt a stiffening system, which must be compatible with the deployment one. Second, the analysis of the behavior of bistable structures is of great interest for the morphing between different configurations of the membrane structure. Moving the sail from one stable shape to another, the actuator only needs to exert force during the actuation phase since the structure stabilizes once the target shape is reached. This last point opens up a last path that goes beyond the passive deployment requirement but can take advantage of the architecture of the actuator designed here. By controlling the action of the Nitinol wires by the Joule effect and coupling them with bistable origami structures, it is in fact possible to open and close the membrane in different configurations based on mission requirements.

Bibliography

[1] S.-M. An, J. Ryu, M. Cho, and K.-J. Cho. Engineering design framework for a shape memory alloy coil spring actuator using a static two-state model. *Smart Materials and Structures*, 21(5):055009, apr 2012. doi: 10.1088/0964-1726/21/5/055009. URL `https://dx.doi.org/10.1088/0964-1726/21/5/055009`.

[2] Ansys. Software for digital mission engineering and systems analysis. URL `https://www.ansys.com/it-it/products/missions/ansys-stk`.

[3] Ansys STK. STK Premium (Space) Advanced analytical tools and higher fidelity modeling in the space domain. URL `https://www.ansys.com/content/dam/amp/2022/june/webpage-requests/stk-product-page/brochures/stk-premium-space-brochure.pdf`.

[4] A. K. Arudra. Atmospheric density estimation using satellite precision orbit ephemerides. Master's thesis, 2011. URL `http://hdl.handle.net/1808/7650`.

[5] Astroscale. Astroscale's ELSA-d Mission Successfully Completes Complex Rendezvous Operation. URL `https://astroscale.com/astroscales-elsa-d-mission-successfully-completes-complex-rendezvous-operation`.

[6] W. K. Belvin, M. Straubel, W. K. Wilkie, M. E. Zander, J. M. Fernandez, and M. F. Hillebrandt. Advanced deployable structural systems for small satellites. Technical report, NASA Langley Research Center, DLR Institute of Composite Structures and Adaptive Systems, Institute of Adaptronics and Function Integration, 2016.

[7] M. E. H. Bhuiyan. Dynamic modeling and analysis of strain energy deployment of an origami flasher. Master's thesis, University of Toledo, 2017.

[8] A. Boschetto, L. Bottini, G. Costanza, and M. E. Tata. Shape memory activated self-deployable solar sails: Small-scale prototypes manufacturing and planarity analysis by 3d laser scanner. *Actuators*, 8(2), 2019. ISSN 2076-0825. doi: 10.3390/act8020038. URL `https://www.mdpi.com/2076-0825/8/2/38`.

[9] L. Brinson. One-dimensional constitutive behavior of shape memory alloys: Thermo-

mechanical derivation with non-constant material functions and redefined martensite internal variable. *Journal of Intelligent Material Systems and Structures*, 4(2):229–242, 1993. doi: 10.1177/1045389X9300400213. URL `https://doi.org/10.1177/1045389X9300400213`.

[10] S. Channumsin, M. Ceriotti, G. Radice, and I. Watson. Experimental validation of damping properties and solar pressure effects on flexible, high area-to-mass ratio debris model. *Acta Astronautica*, 138:129–144, 2017. ISSN 0094-5765. doi: https://doi.org/10.1016/j.actaastro.2017.05.015. URL `https://www.sciencedirect.com/science/article/pii/S0094576516309444`. The Fifth International Conference on Tethers in Space.

[11] T. Chen, O. R. Bilal, R. Lang, C. Daraio, and K. Shea. Autonomous deployment of a solar panel using elastic origami and distributed shape-memory-polymer actuators. *Phys. Rev. Appl.*, 11:064069, Jun 2019. doi: 10.1103/PhysRevApplied.11.064069. URL `https://link.aps.org/doi/10.1103/PhysRevApplied.11.064069`.

[12] F. C. Commission. FCC Adopts New '5-Year Rule' for Deorbiting Satellites, 2022. URL `https://www.fcc.gov/document/fcc-adopts-new-5-year-rule-deorbiting-satellites`.

[13] H. D. Curtis. *Orbital Mechanics For Engineering Students*. Butterworth-Heinemann, Boston, third edition edition, 2014. ISBN 978-0-08-097747-8. doi: https://doi.org/10.1016/B978-0-08-097747-8.00002-5.

[14] *D3 Technical Sheet*. D-Orbit SpA. URL `file:///C:/Users/tommi/Downloads/D3.pdf`.

[15] M. M. P. Data. Nitinol - niti shape memory alloy; high-temperature phase. URL `https://www.matweb.com/search/datasheet.aspx?matguid=de9dd08433714f698d513766dccea437`.

[16] Y. Dharmadasa, C. Mallikarachchi, and F. Lopez Jimenez. Characterizing the mechanics of fold-lines in thin kapton membranes. 01 2018. doi: 10.2514/6.2018-0450.

[17] L. A. Di Landro, G. Sala, A. Airoldi, and P. Bettini. *Tecnologie e materiali aerospaziali*, chapter 31. Arseni Souryal, 3 edition, 2018.

[18] L. A. Di Landro, G. Sala, A. Airoldi, and P. Bettini. *Tecnologie e materiali aerospaziali*, chapter 58. Arseni Souryal, 3 edition, 2018.

[19] L. A. Di Landro, G. Sala, A. Airoldi, and P. Bettini. *Tecnologie e materiali aerospaziali*, chapter 52. Arseni Souryal, 3 edition, 2018.

[20] Dunmore. Aluminized kapton® film. URL `https://www.dunmore.com/products/aluminized-polyimide-film.html`.

[21] DuPont™. Kapton® Polyimide films. URL `https://www.dupont.com/electronic-materials/kapton-polyimide-film.html`.

[22] ESA. InflateSail. URL `https://www.eoportal.org/satellite-missions/inflatesail#eop-quick-facts-section`.

[23] ESA. ELSA-d (End-of-Life Service by Astroscale Demonstration). URL `https://www.eoportal.org/satellite-missions/elsa-d`.

[24] ESA. CanX-7 (Canadian Advanced Nanospace eXperiment-7), . URL `https://www.eoportal.org/satellite-missions/canx-7#spacecraft`.

[25] ESA. LightSail Missions of The Planetary Society, . URL `https://www.eoportal.org/satellite-missions/lightsail`.

[26] ESA. IAE (Inflatable Antenna Experiment), 2012. URL `https://www.eoportal.org/satellite-missions/iae#eop-quick-facts-section`.

[27] ESA. ESA purchases world-first debris removal mission from start-up, 2020. URL `https://www.esa.int/Space_Safety/ESA_purchases_world-first_debris_removal_mission_from_start-up`.

[28] ESA Space Debris Office. ESA's annual space environment report. Technical report, ESA ESOC, 2022.

[29] M. Fossati. Origami engineering: Evaluation of patterns for deployable space structures. Master's thesis, Politecnico di Milano, 2022.

[30] J. Fulton and H. Schaub. Deployment dynamics analysis of an origami-folded spacecraft structure with elastic hinges. *Journal of Spacecraft and Rockets*, 59:1–20, 09 2021. doi: 10.2514/1.A34938.

[31] N. Geographics. Origami is revolutionizing technology, from medicine to space, . URL `https://www.nationalgeographic.com/magazine/article/origami-driving-futuristic-technologies-feature`.

[32] N. Geographics. Episode 5: Unfolding the future of origami, . URL `https://www.nationalgeographic.com/podcasts/article/unfolding-the-future-of-origami`.

[33] C. Giovannini. Solar sail strategies for satellite's direct and modulating deorbiting.

Master's thesis, Politecnico di Milano, Milan, 2021. URL `http://hdl.handle.net/10589/183320`.

[34] W. D. Hayes and P. Ronald F. Hypersonic flow theory. Technical report, Academic Press, New York, 1959.

[35] L. Heller, K. Janouchová, P. Sittner, and D. Vokoun. Functional textiles driven by transforming niti wires. *MATEC Web of Conferences*, 33:03010, 12 2015. doi: 10.1051/matecconf/20153303010.

[36] Hexagon. Adams, 2023. URL `https://hexagon.com/it/products/product-groups/computer-aided-engineering-software/adams`.

[37] *Adams View Command User's Guide*. Hexagon AB, 2021.

[38] S. Hobbs, J. Kingston, P. Roberts, C. Juanes, R. Sewell, B. Snapir, F. Robinson, J. V. Llop, J. Hobbs, and M. Patel. De-Orbit Sail Design For Techdemosat-1. Technical report, Cranfield University, 2013.

[39] P. S. C. Jr. and C. R. Naegeli. Low-perigee aerodynamic heating during orbital flight of an atmosphere explorer. Technical report, NASA, Goddard Space Flight Center Greenbelt, Md. 20771, 1976.

[40] Y. I. Khlopkov, V. A. Zharov, Z. Y. M. Myint, and A. Y. Khlopkov. Investigation of the heat transfer coefficients on the body surface in high speed flow. Technical Report 4, Department of Aeromechanics and Flight Engineering, Moscow Institute of Physics and Technology, Zhukovsky, Russia, 2015.

[41] J.-S. Koh, S. Kim, and K.-J. Cho. Self-folding origami using torsion shape memory alloy wire actuators. page V05BT08A043, 08 2014. doi: 10.1115/DETC2014-34822.

[42] *TECHNICAL DATA SHEET Mylar® (Polyester Film)*. Laminated Plastics, 7 Executive Park Dr., Billerica, MA 01862.

[43] B. Landen A. A dynamic modeling approach and optimization framework for the design of self-folding origami structures. Master's thesis, Pennsylvania State University, 2016.

[44] F. Landis Markley and J. L. Crassidis. *Fundamentals of Spacecraft Attitude Determination and Control*. Space Technology Library, Springer, 2021. ISBN 978-1-4939-0802-8 Published: 31 May 2014. doi: https://doi.org/10.1007/978-1-4939-0802-8.

[45] C. Liang and C. Rogers. One-dimensional thermomechanical constitutive relations for shape memory materials. *Journal of Intelligent Material Systems and Structures*,

1(2):207–234, 1990. doi: 10.1177/1045389X9000100205. URL `https://doi.org/10.1177/1045389X9000100205`.

[46] S. Liu, G. Lu, Y. Chen, and Y. Leong. Deformation of the miura-ori patterned sheet. *International Journal of Mechanical Sciences*, 99, 05 2015. doi: 10.1016/j.ijmecsci.2015.05.009.

[47] P. S. Lobo, J. Almeida, and L. Guerreiro. Shape memory alloys behaviour: A review. *Procedia Engineering*, 114:776–783, 2015. ISSN 1877-7058. doi: https://doi.org/10.1016/j.proeng.2015.08.025. URL `https://www.sciencedirect.com/science/article/pii/S1877705815016641`. ICSI 2015 The 1st International Conference on Structural Integrity Funchal, Madeira, Portugal 1st to 4th September, 2015.

[48] C. lv, D. Krishnaraju, G. Konjevod, H. Yu, and H. Jiang. Origami based mechanical metamaterials. *Scientific reports*, 4:5979, 08 2014. doi: 10.1038/srep05979.

[49] T. M. C. Sears. Sail material, inspection imager, and deployment analysis for an end-of-life disposal drag sail. Technical report, Space Flish Laboratory, University of Toronto Institute for Aerospace Studies, Toronto, Ontario, Canada M3H 5T6, 2014.

[50] M. J. Matney. Algorithms for the computation of debris risk. Technical report, NASA Orbital Debris Program Office, NASA Johnson Space Center, 2101 NASA Parkway, Houston Texas, USA, 77058, 2017.

[51] J. Matthey. Nitinol technical properties. URL `https://matthey.com/products-and-markets/other-markets/medical-components/resource-library/nitinol-technical-properties`.

[52] M. Mirhosseini and A. Saboonchi. View factor calculation using the monte carlo method for a 3d strip element to circular cylinder. *International Communications in Heat and Mass Transfer*, 38(6):821–826, 2011. ISSN 0735-1933. doi: https://doi.org/10.1016/j.icheatmasstransfer.2011.03.022. URL `https://www.sciencedirect.com/science/article/pii/S0735193311000674`.

[53] Momentus. Vigoride^{TM} First Flight. URL `https://momentus.space/vigoride-first-flight/`.

[54] NASA. ORDEM 3.2 : OD Engineering Model. URL `https://orbitaldebris.jsc.nasa.gov/modeling/ordem.html`.

[55] NASA. Solar power, origami-style. URL `https://www.nasa.gov/jpl/news/origami-style-solar-power-20140814`.

[56] NASA/GSFC/NSSDC. COSPAR International Reference Atmosphere from NSSDC. URL `https://cmr.earthdata.nasa.gov/search/concepts/C1214605543-SCIOPS`.

[57] C. Pardini and L. Anselmo. Evaluating the impact of space activities in low earth orbit. *Acta Astronautica*, 184:11–22, 2021. ISSN 0094-5765. doi: https://doi.org/10.1016/j.actaastro.2021.03.030. URL `https://www.sciencedirect.com/science/article/pii/S0094576521001430`.

[58] U. SFL. Space Flight Laboratory announces successful deorbiting of nanosatellite with drag sail technology. sails reduced time as space debris by 178 years, 2022. URL `https://www.utias-sfl.net/?p=3942`.

[59] D. D. A. Spencer. Testing The LightSail Program: Advancing Solar Sailing Technology Using a CubeSat Platform. *JoSS (Journal of Small Satellites)*, 2016.

[60] K. Taylor-Smith. How has nanotechnology helped the development of nitinol? *AZoNano*, 8 2022. URL `https://www.azonano.com/article.aspx?ArticleID=5366`.

[61] *Upilex-S*. UBE Europe GmbH Performance Materials Department, Immermannstrasse 65B, 40210 Düsseldorf, Germany. Version: 031105.

[62] M. R. Vujičić, N. P. Lavery, and S. G. R. Brown. Numerical sensitivity and view factor calculation using the monte carlo method. *Proceedings of the Institution of Mechanical Engineers, Part C: Journal of Mechanical Engineering Science*, 220(5):697–702, 2006. doi: 10.1243/09544062JMES139. URL `https://doi.org/10.1243/09544062JMES139`.

[63] D. K. Weidner, C. L. Hasseltine, R. E. Smith, and S. A. Mills. Models of Earth's Atmosphere (120 to 1000 Km). Technical report, NASA, 1969.

[64] Q. Zhang, Y. Liu, M. Li, Y. Han, J. Cai, and J. Feng. Simulation of dynamics during deployment of foldable origami structures. *International Journal of Structural Stability and Dynamics*, 20, 04 2020. doi: 10.1142/S0219455420500583.

[65] Q. Zhang, Y. Liu, M. Li, Y. Han, J. Cai, and J. Feng. Simulation of dynamics during deployment of foldable origami structures. *International Journal of Structural Stability and Dynamics*, 20(05):2050058, 2020. doi: 10.1142/S0219455420500583. URL `https://doi.org/10.1142/S0219455420500583`.

A | SMA actuator configuration choice

In Chapter 5, the constitutive model of shape memory alloys is presented and the configuration of the Nitinol wire integrated into the origami structure is defined. Two factors mainly dictate the choice to make the wire work by torsion: the effectiveness of the actuator in terms of exerted force and deployment and its compatibility with the membrane. The twisting wire exerts a large actuating force on the structure. The analysis done in Chapter 6 shows how by varying the length, radius, and elongation of the wire, it is possible to find a combination of parameters to guarantee a sufficient torque to unfold the sail. On the contrary, if the wire were placed across the fold (figure A.1), it would tend to work in flection and traction. In the first case, the flexural stiffness is very low due to the geometry of the wire itself, and the force exerted on the structure would not be sufficient to overcome the equivalent torsional stiffness of the crease. Similarly, in order to ensure the complete deployment by working in traction, it must be able to recover a large amount of strain, thus requiring high initial prestrain or very long wires.
The criticalities of this kind of configuration are assessed by experimentally evaluating the deployment of a single Miura-Ori cell, as shown in figure A.1.

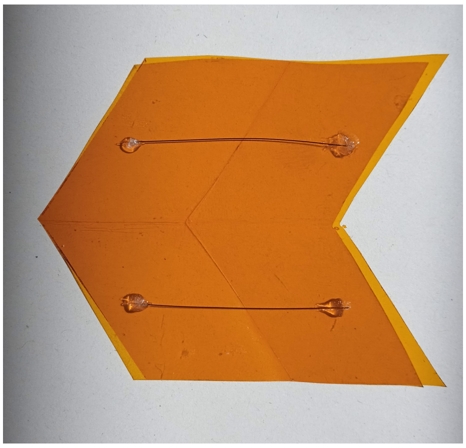

Figure A.1: Miura-Ori single cell in Kapton equipped with two Nitinol wires actuators.

The experimental setup consists of a foil of Kapton cut in the shape of a single Miura-Ori cell. The ends of two Nitinol wires (diameter of 0.2mm and A_s equal to 95°) are fixed on two adjacent faces of the cell with the aid of two-component epoxy glue. The assembly phase is carried out when the cell is completely unfolded so that the wire tries to return to this configuration when heated while packed. Since part of the actuator action is due to the axial recovery of the wire strain, the wire is made long enough to guarantee a large recovery without exceeding the dimension of the cell. Moreover, the wire must be fixed accurately in order to guarantee good adherence to the Kapton model and, consequently, better performance when working in traction. As a matter of fact, if there is space between the membrane and the wire in the deployed configuration, the actuator would not act on the faces of the origami while transformed to austenite, but it would fill this gap without exerting any action on the structure (figure A.2).

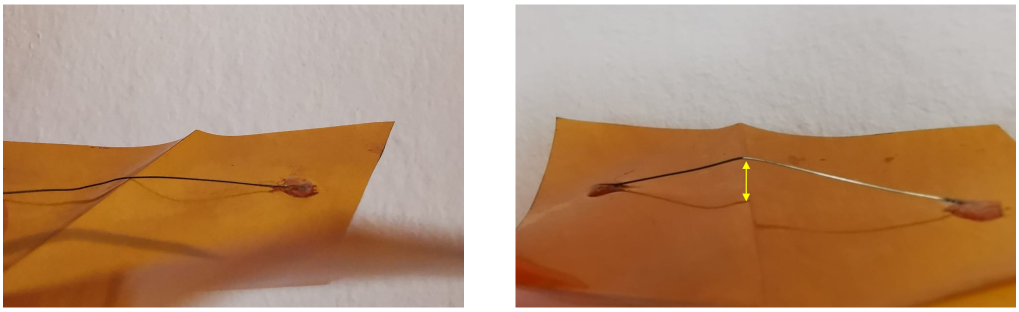
(a) (b)

Figure A.2: The figures shows the proper way of assembling the wire and the cell (A.2a) and the excessive gap between them (A.2a), reducing the actuation effectiveness.

Once the setup is completed, the cell is folded and heated up in a hoven at a temperature of about 120°, high enough to induce the martensitic transformation of the wire without undermining the integrity of the glue. As it can be seen in figure A.3, the force exerted by the wire can deploy the cell up to an almost flat configuration. Nevertheless, some issues related to the structure arise. First of all, since the ends of the wire are fixed on the Miura-Ori faces, which are highly flexible because of low thickness, the latter deforms under the action of the axially recovered strain (figure A.3). The force is thus not focused completely on the deployment of the crease but it is in part spent to bend the origami. As a consequence, the deployment does not occur as completely as intended in the modeling, and a strong deformation effect arises which can not be neglected in a multi-body dynamic simulation. On the contrary, the torsional wire acts directly along the crease and works ideally without exerting a direct bending force on the faces.

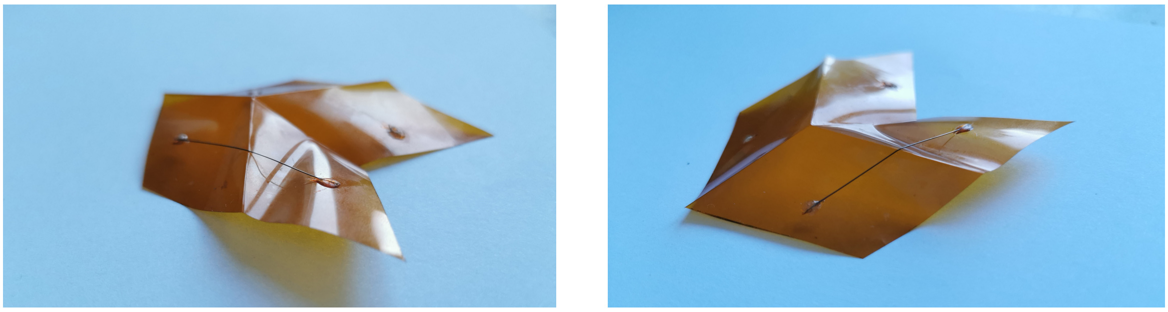

(a) (b)

Figure A.3: Origami faces bending as a consequence of the action of the Nitinol wire. It is evident how the actuator contributes to deploying the cell and bending its faces.

Another relevant aspect to account for is the shape memory effect of Kapton. Since the polymeric origami cell tends to recover its initial shape while heated partially, the experimental activity as described does not allow the evaluation of the effect of the SMA wire alone on the deployment. Therefore, the actuator's action must be decoupled from the polymeric recovery effect. The first way to do this is wire activation with the Joule effect. In this case, the wire is the only heating up and Kapton's recovery is prevented. However, this solution goes beyond the discussion proposed in the thesis concerning the passive heating of the wire and it is preferable to take another way.
The origami cell material is thus changed from Kapton to aluminum. The metal owns different crease-equivalent torsional spring stiffness characteristics, but it allows a raw experimental analysis of the effects of the actuation induced by the wires.

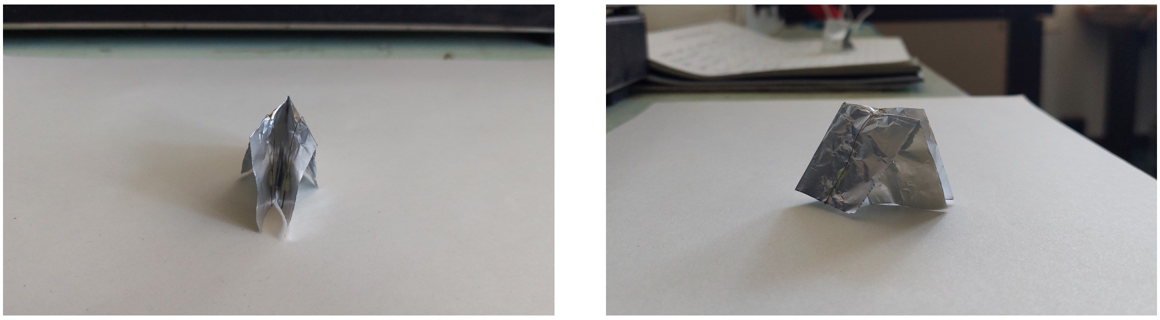

(a) (b)

Figure A.4: Packed aluminum cell.

The setup is exactly the same as the one for Kapton. This time, the aluminum is completely passive in the heat-induced actuation process and the deployment can be attributed entirely to the SMA actuator. The result is the one shown in figure A.5.

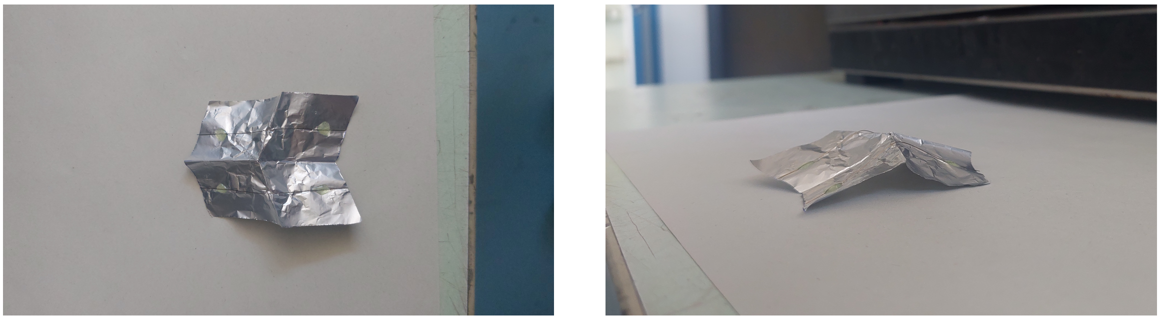
(a) (b)

Figure A.5: Deployed aluminum cell.

It is evident how the wires can partially deploy the cell but the issues are similar to those seen with Kapton. As a matter of fact, even if the configuration is almost flat, the actuator tends to bend the faces of the cell, whereas the creases maintain a certain folding angle. Moreover, the aluminum highlights the localized deformations on the cell caused by the Nitinol wire. The axial strain recovery of the wire and the requirement of making it adhere to the cell before folding causes the crease line to wrinkle under the pressure exerted by the wire during the deployment. This effect can cause the membrane structure to be damaged or improperly wrinkled, altering the effectiveness of the deployment mechanism. Better results in terms of wrinkles reduction could be obtained by making the wire accurately follow the angle generated by the faces on which it is fixed. It is indeed evident from figure A.4 that Nitinol is shaped with a relatively wide curvature angle and it does not form a sharp angle following the membrane crease. This experimental setup is forced by the yield point of the SMA wire. If the wire is folded as stated above, the region in the neighborhood of the folding point is subjected to highly concentrated stresses of compression and traction (figure A.6b). Therefore, the wire in the martensitic phase first transforms from martensite twinned to martensite detwinned, then it overcomes the elastic deformation region and enters the plastic one (figure A.6a). When the bending force is released, after a partial elastic recovery the wire assumes a deformed shape made of two components. The first is the amount of deformation the shape memory alloy can recover in the martensitic transformation, usually below 6% (represented in green in figure A.6a). The remaining part is the non-recoverable permanent plastic deformation preventing Nitinol from returning to its initial shape. This phenomenon damages the actuator's effectiveness and must be carefully avoided since an incomplete recovery of Nitinol's shape would cause in turn an incomplete deployment of the origami.

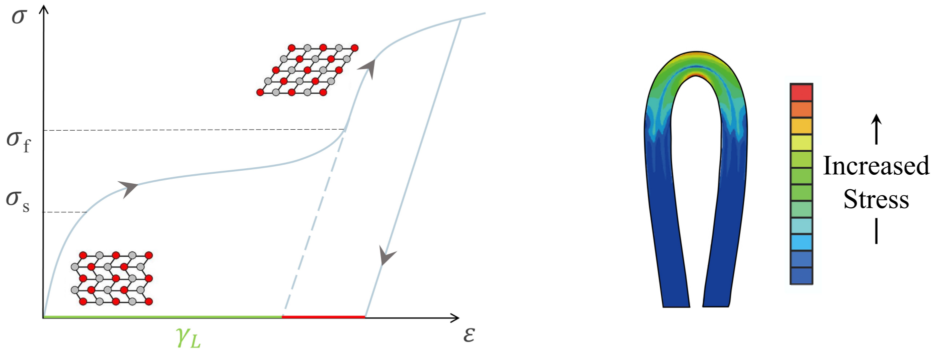

(a)

(b)

Figure A.6: Permament plastic deformation due to low curvature angle.

The figure below shows the Nitinol wire used in the experimental analysis subjected to high bending deformation, before and after the martensitic transformation. When it is heated, partial bending remains as a consequence of plasticization.

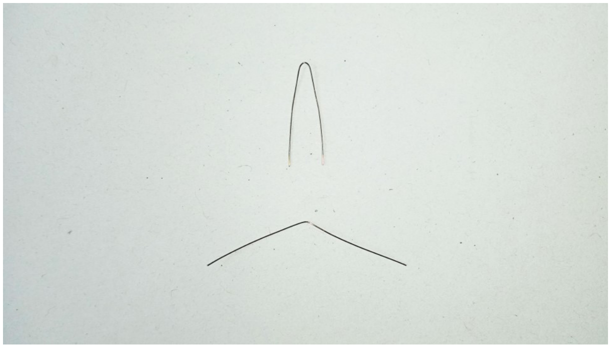

Figure A.7: Nitinol wire plastic deformation. Part of the deformation is recovered in the martensitic transformation, and another part is maintained.

This issue does not affect the torsional SMA wire since the actuator lies on the crease of the pattern without involving any axial or bending deformation. The wire must be bent only to give continuity between the portion that works in torsion and the one that adheres to the faces of the origami, but the curvature radius can be selected properly and it is not constrained by the folding angle.

The impossibility of training the wire to work in torsion prevents carrying out an equivalent experimental analysis evaluating the effectiveness of this solution. Nevertheless, the valid results coming from the analytical study and the experimental issues related with the axial-bending configuration make it interesting to develop future experimental models able to demonstrate the feasibility of the torsional solution.

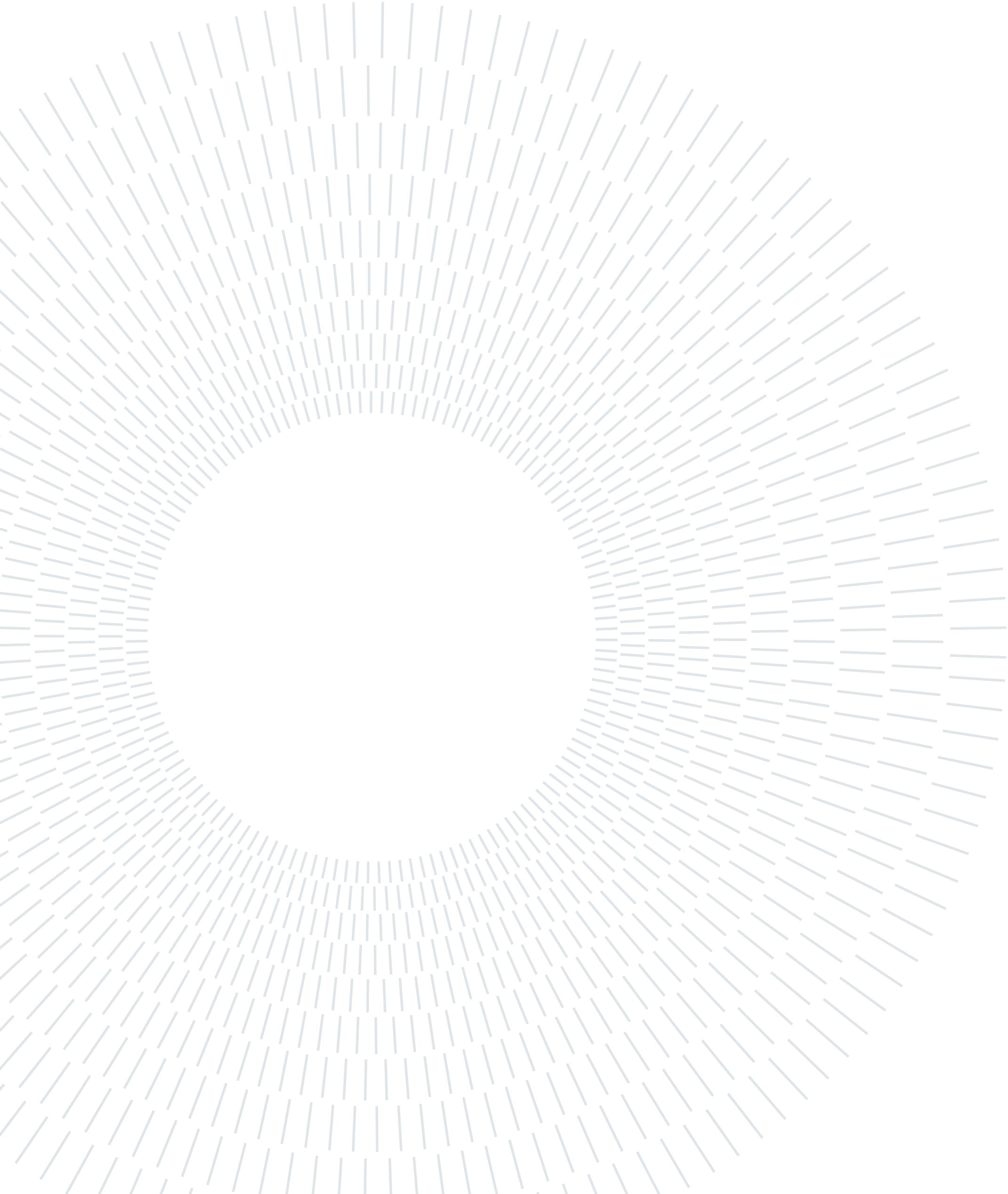

List of Figures

1 Inflatable Antenna Experiment. 1
2 James Webb Space Telescope: sunshield deployment phase. 2
3 Drag sail de-orbit device. 2

1.1 Space objects evolutions in all orbits. Report by ESA [28]. 5
1.2 Space debris impact damages on spacecrafts. 6
1.3 Debris removal mission concepts. 8
1.4 Active de-orbiting systems. 9
1.5 Lightsail spacecraft 10
1.6 Space debris removal with drag sail. 11
1.7 Long March 2D deorbit with drag sail. On-board camera image. 11
1.8 Z-folding technique. 14
1.9 Miura-Ori folding pattern. 15
1.10 Flasher folding pattern. 16
1.11 Starshade: flasher origami. 16
1.12 Mission concept: perimeter truss deployment system. 17
1.13 Storable Tubular Expandable Member (STEM) technology. 18
1.14 Inflatable deployment and rigidization systems. 19
1.15 Perimeter truss SMP deployment system. Image credits: [11]. 20
1.16 SMA embedment in gossamer structure. Image credits: [8]. 20

2.1 Earth Centered Inertial Frame. 22
2.2 Harmonic potentials. From left to right: zonal, tesseral and sectoral. 25
2.3 Sail orientation along the orbit. 26
2.4 $\mathbf{a}_{drag}$ and $\mathbf{a}_{SRP}$ versus orbital height. 27
2.5 Sail orientation along the orbit. 28
2.6 De-orbit representation from 700km altitude. 29
2.7 De-orbit lifetime based on a $4m^2$ drag sail (image credit: UTIAS/SFL [24]). The data are obtained from the Ansys software STK Premium Space (Chapter 2.5). 30

2.8 STK lifetime tool 31
2.9 De-orbit lifetime sensitivity to sail size. 33
2.10 Origami optimization software, user interface [29]. 34
2.11 Predominance of the deployment along X axis (Kresling tessellation). . . . 34
2.12 Miura-Ori packed and deployed configurations. 35

3.1 Sail temperature trend over one orbit. 40
3.2 Sail temperature during reentry. 41
3.3 Radiation heat transfer for deployed and partially folded Miura-Ori origami. 42
3.4 Monte Carlo method for the computation of the Miura-Ori self view factor. 43
3.5 Self view factors of different Miura-Ori origami faces. 44
3.6 Self view factor as a function of the deployment angle θ. 45

4.1 Miura-Ori drag sail optimal geometry. 49
4.2 Single cell geometry. 50
4.3 Multi-body dynamics simulation: drag sail initial configuration (θ=89°). . . 51
4.4 Miura-Ori multi-body dynamics simulation: crease model. 52
4.5 Effects of the crease-face stiffness relationship during deployment. 53
4.6 ADAMS graphical interface. 54
4.7 Drag sail dynamics analysis: block scheme. 54

5.1 Crystalline structure of the three phases of shape memory alloys. 58
5.2 One-way and two-way shape memory effect. 58
5.3 Shape memory alloy phase diagram. 59
5.4 Ti-Ni alloy characteritics. 60
5.5 Examples of the application of small-sized SMA components. 61
5.6 Configuration of the shape memory alloy wire actuator. 62
5.7 SMA wire arrangments along the origami pattern. 63
5.8 Miura-Ori multi-body dynamics simulation: actuator model. 68
5.9 α_1 and α_2 trend as the origami unfolds. 69

6.1 Miura-Ori cell geometry. 72
6.2 Simulink simulation scheme. 72
6.3 Influence of the position of the SMA wires on the packed dimension. 73
6.4 Shift distance between two consecutive vertices of the Miura-Ori. 74
6.5 Torque and stress trend for different values of initial prestrain. 76
6.6 Strain recovery trend during sail deployment for different initial prestrains. 77
6.7 Deployment time as a function of different prestrain and wire radius. . . . 77
6.8 Drag sail deployment for different values of l_w and r_w. $\gamma_L = 0.025$. 78

6.9 Free-recover angle for different optimization results. 81
6.10 Torque and stress trend for different values of initial prestrain. 82
6.11 Strain recovery trend during sail deployment for different initial prestrains. 82
6.12 Deployment time of different optimal solutions. 82
6.13 Deployment of the drag sail due to the action of the SMA wires. 83
6.14 Strain recovery during deployment. 84
6.15 Stress and torque trends as a function of temperature during the deployment. 84
6.16 Deployment trend for different dimensions of the origami sail ($N_x \times N_y$). The results are obtained by simulating the structures with fixed SMA actuator characteristics: $r_w = 140\mu m$, $l_w = 2.1mm$, $\gamma_L = 0.025$. 85
6.17 Ratio between the number of wires and creases. 86
6.18 Deployment sequence of the origami drag sail. 86
6.19 Uncertainty propagation on the torque generated by the wire during the deployment. 88

A.1 Miura-Ori single cell in Kapton equipped with two Nitinol wires actuators. 97
A.2 Actuator-cell gap. 98
A.3 Origami faces bending. 99
A.4 Packed aluminum cell. 99
A.5 Deployed aluminum cell. 100
A.6 Permament plastic deformation. 101
A.7 Nitinol wire plastic deformation. 101

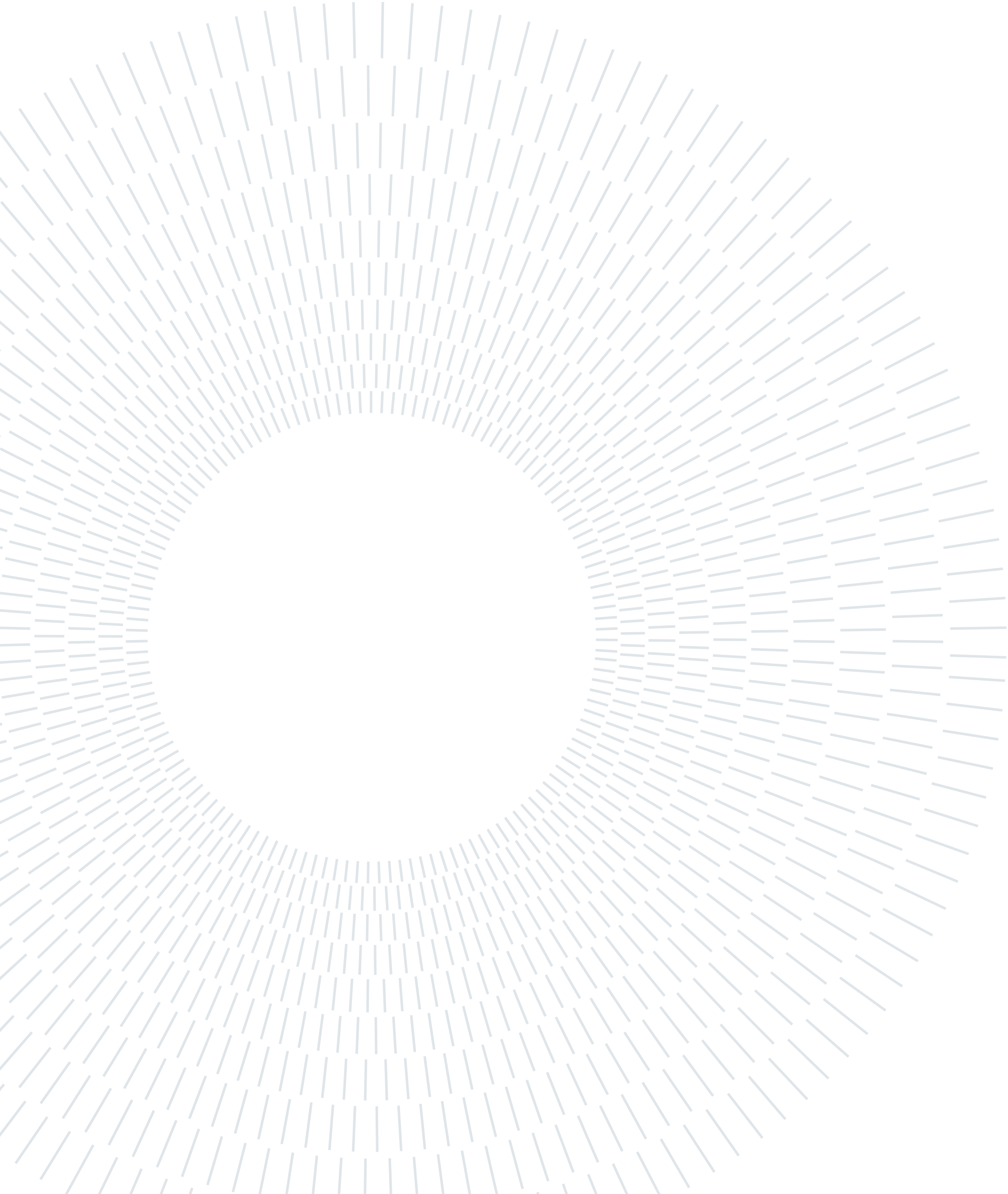

List of Tables

1.1 Time elapsed between two successive collisions. 7
1.2 Atomic oxygen erosion estimates. 13
1.3 Origami tesselations for space engineering application. 17

2.1 Earth zonal harmonics. 25
2.2 Size of the sail needed to deorbit the satellite within 5 years. 31
2.3 MATLAB®-STK Premium Space results comparison for different altitudes. 32
2.4 MATLAB®-STK Premium Space results comparison for different inclinations. 32
2.5 Optimized origami drag sail. 36

3.1 Heat rate per unit surface as a function of the altitude. 39

6.1 Radius dimension as the prestrain varies (fixed wire length). 76
6.2 Optimim radius and length dimension for different prestrain values. 80
6.3 SMA properties. The values refer to a typical mid-temperature range Nitinol. 83

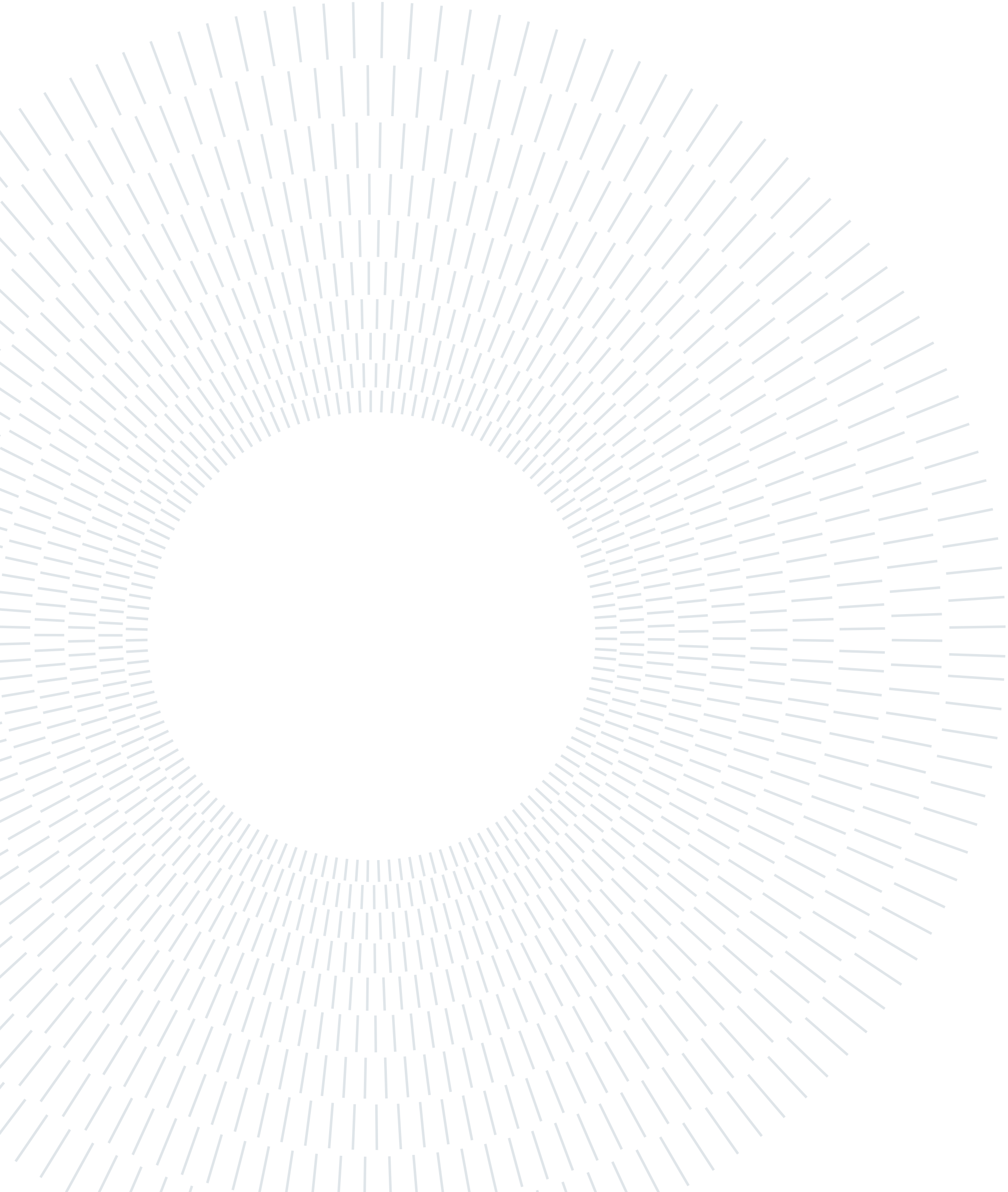

List of Symbols

Variable	Description	SI unit
A	Surface	m^2
a	Earth albedo coefficient	-
A_{cross}	Cross sectional area	m^2
A_f	Austenite finish temperature	K
$\boldsymbol{a}_{J_2}$	Acceleration due to Earth oblateness	$\mathrm{m\ s}^{-2}$
$\boldsymbol{a}_p$	perturbing accelerations	$\mathrm{m\ s}^{-2}$
A_s	Austenite start temperature	K
$\boldsymbol{a}_{SRP}$	Acceleration due to SRP	$\mathrm{m\ s}^{-}2$
AU	Astronomical unit	m
c	Speed of light	$\mathrm{m\ s}^{-1}$
c_V	Specific heat capacity	$\mathrm{m}^2\ \mathrm{s}^{-2}\ \mathrm{K}^{-1}$
C_A	Austenite transformation line inclination	$\mathrm{Pa\ K}^{-1}$
C_D	Drag coefficient	-
C_M	Martensite transformation line inclination	$\mathrm{Pa\ K}^{-1}$
D	Elastic modulus	Pa
D_A	Austenite elastic modulus	Pa
D_M	Martensite elastic modulus	Pa
E	Energy of photons	J
$\dot{E}''_{Sun}$	Sun's heat rate per unit surface	$\mathrm{J\ m}^{-2}\ \mathrm{s}^{-1}$
$\dot{E}''_{Earth}$	Earth's heat rate per unit surface	$\mathrm{J\ m}^{-2}\ \mathrm{s}^{-1}$
$\boldsymbol{f}_{i,j}$	Face of the origami	-
$\boldsymbol{f}_D$	Damping force vector	$\mathrm{kg\ m\ s}^{-2}$
F_{self}	Miura-Ori self view factor	-
G	Gravitational constant	$\mathrm{kg}^{-1}\ \mathrm{m}^3\ \mathrm{s}^{-2}$
h	Planck constant	$\mathrm{m}^2\ \mathrm{kg\ s}^{-1}$

J	Polar moment of inertia	m^4
J_2	Second Earth zonal harmonic	-
k	Hinge stiffness	N rad^{-1}
$\dot{l}$	Length of a single origami cell	m
$\dot{L}$	Work rate exchanged	J s^{-1}
$\boldsymbol{M}$	Mass matrix	m
M	Crease torque	Nm
M_f	Martensite finish temperature	K
M_s	Martensite start temperature	K
m_1	Mass of the first gravitationally interacting body	kg
m_2	Mass of the second gravitationally interacting body	kg
$m_{s/c}$	Mass of the spacecraft	kg
N_x	Miura-Ori number of cells along x	-
N_y	Miura-Ori number of cells along y	-
p	Momentum transferred from photon to satellite at impact	kg m s^{-1}
r	Orbital radius	m
$P_{SRP@1AU}$	SRP pressure at 1AU distance from Sun	Pa
$\boldsymbol{Q}$	Vector of generalized forces	N
$\dot{Q}$	Heat rate exchanged	J s^{-1}
$\boldsymbol{q}$	Vector of generalized nodal coordinates	m
$\dot{Q}_{alb}$	Earth albedo heat rate radiation	J s^{-1}
$\dot{Q}_{ds}$	Heat rate radiation toward deep space	kg J s^{-1}
$\dot{Q}_{drag}$	Aerodynamic heat rate	J s^{-1}
$\dot{Q}_{Earth}$	Earth heat rate radiation	J s^{-1}
$\dot{Q}_{refl}$	Reflected heat rate radiation	J s^{-1}
$\dot{Q}_{sail,rad}$	Radiation heat rate between sail and wire	J s^{-1}
$\dot{Q}_{sail,con}$	Conduction heat rate between sail and wire	J s^{-1}
$\dot{Q}_{Sun}$	Sun's heat rate radiation	J s^{-1}
$\boldsymbol{r}$	Orbital position	m
$\ddot{\boldsymbol{r}}$	Orbital acceleration	m s^{-2}
$\boldsymbol{r}_{s/c-Sun}$	Distance vector from spacecraft to Sun	m
S	Entropy density	J K^{-1}
T	Torque	Nm

T	Temperature	K
T_0	Initial temperature	K
T_s	Sail temperature	K
T_w	Wire temperature	K
T_{sail}	Temperature of the sail	K
T_{ds}	Temperature of the deep space	K
U	Internal energy	J
u	Specific internal energy	J m^{-2}
$\boldsymbol{u}_r$	Orbital position versor	-
V	Volume	kg m^2 s^{-3}
$\boldsymbol{v}_{rel}$	Spacecraft-air relative velocity	m s^{-1}
W	Length of the crease	l
w	Width of a single origami cell	m
x_{shift}	Miura-Ori cells shift	m
y_{shift}	Miura-Ori cells shift	m
α	Absorption coefficient	-
α_1	Miura-Ori angle	rad
α_2	Miura-Ori angle	rad
α_w	Absorption coefficient of the wire	-
γ	Shear strain	-
γ_0	initial shear strain	-
$\Delta\alpha$	Recoverable angle	K
ε	Emission coefficient	-
ε	Strain	-
ε_0	Initial strain	-
ε_L	Maximum recoverable strain	-
ε_w	Emission coefficient of the wire	-
η	Reflectivity coefficient	-
λ	Lagrange multiplier	-
μ	Earth gravitational parameter	m^3 s^{-2}
ν	Frequency of electromagnetic wave	s^{-1}
ξ	Martensitic fraction	-
ξ_0	Initial martensitic fraction	-

ξ_S	Stress-induced martensitic fraction	-
ξ_{S0}	Initial stress-induced martensitic fraction	-
ξ_T	Temperature-induced martensitic fraction	-
ξ_{T0}	Initial Temperature-induced martensitic fraction	-
Θ_0	Thermoelastic tensor	kg s^{-2} K^{-1}
θ	Deployment angle	rad
θ_0	Initial deployment angle	rad
θ_{fin}	Final deployment angle	rad
θ_{min}	Optimized deployment angle	rad
ρ	Density	kg m^{-3}
ρ_{atm}	Atmospheric density	kg m^{-3}
ρ_{sail}	Reflection coefficient of the sail	-
σ	Stefan Boltzmann constant	kg s^{-3} K^{-4}
σ	Cauchy stress	Pa
σ_0	Initial Cauchy stress	Pa
τ	Shear stress	Pa
τ_0	Initial shear stress	Pa
$\boldsymbol{\Phi}$	Complete set of Kinematics constraints	N
ϕ	Initial fold angle	m
$\boldsymbol{\Phi_q}$	Complete set of Kinematics constraints	N
Ω	Transformation tensor	Pa
Ω_S	Stress-induced transformation tensor	Pa
Ω_T	Temperature-induced transformation tensor	Pa

Acknowledgements

These months of work dedicated to the development of the thesis have been the perfect conclusion of an extraordinary journey that began at the age of 19.

The most sincere thanks go to Professor Antonio Grande and Laura, for the dedication and patience they have shown in wonderful months of very stimulating work. Thank you for making the thesis so interesting and for everything I've still managed to learn after 5 years of lessons. I also wish Laura the best of luck in completing her Ph.D. and wish her the best in everything that awaits her later. I thank Martino for supporting me in the first weeks of my thesis, and I wish Eleonora and Nadir to enjoy these months of work. I am sure that their enthusiasm will greatly contribute to the topic's development.

A special thank goes to my classmates, without whom these five years would not have been so much fun. Thank you for the mixed moments of joy and madness during the master thesis projects. Thanks to my mechanic friends with whom I spent three unforgettable years of lessons and laughs, especially with Jack.

I cannot but thank my everyday friends for the many adventures spent together. Among them, I want to give special thanks to Chop, Mac, Rada, and Stucchi (in strict alphabetical order). If today I can write these thesis pages, the credit is also yours.

For Alice and Chiara I would need a separate appendix. The joy and life that you bring within the walls of home have made many days of intense study much lighter and your company goes beyond the simple coexistence between *sorelli*.

The heartfelt dedication goes to Francesca, her infinite patience, and all the support she has given me in these years of study.

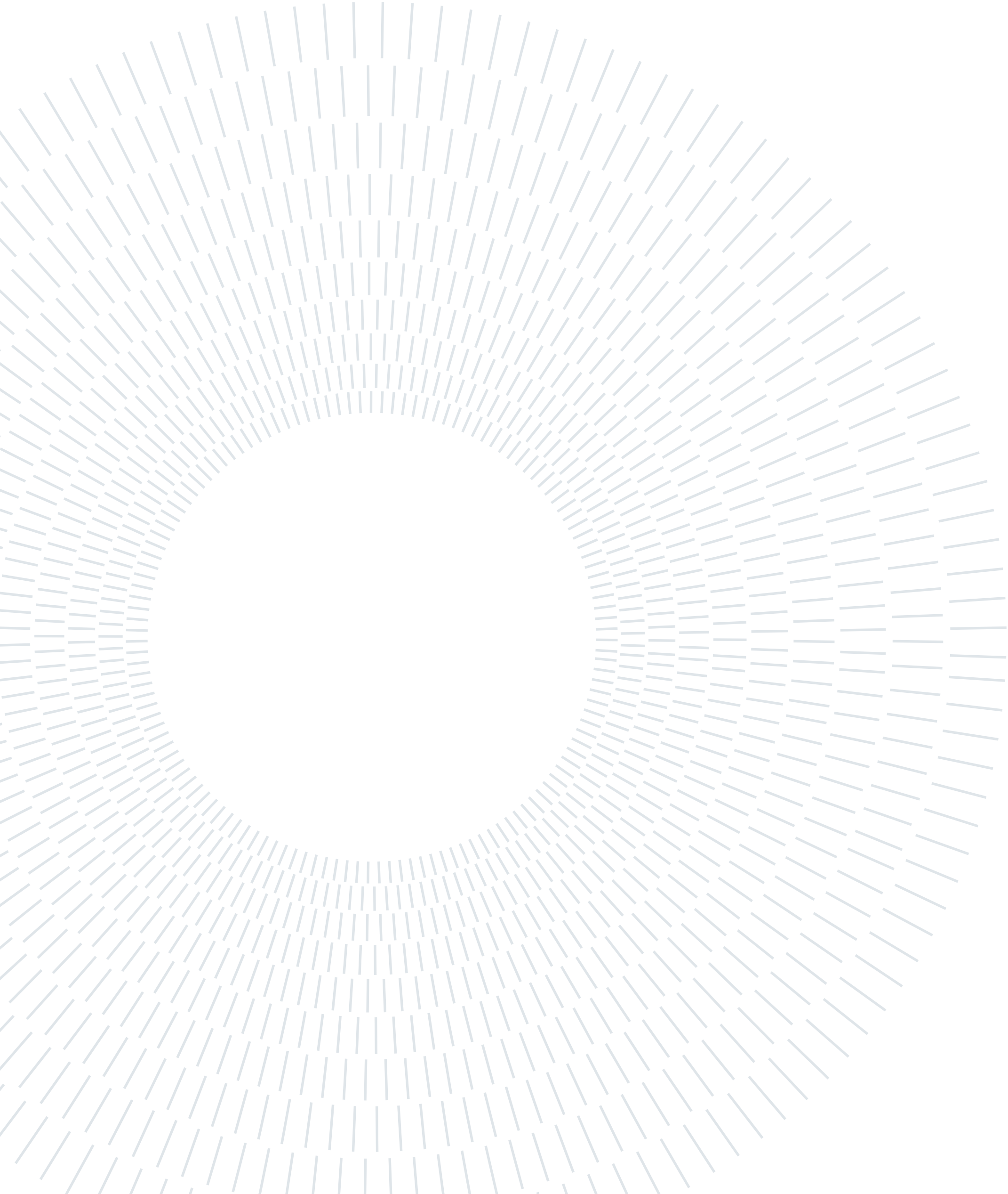Lastly, the greatest thank go to Mum and Dad, which extends well beyond the university period alone. They are my inspiration and model, my joy and love. All the exams I passed are the result of years of severe and loving education that has taught me to face each day with energy and determination. You have often been the engine that drove me to do well, hoping to repay you for all the efforts made to make me the person I am now. Everything I am today I owe to you.